Fakultät für Medizin

Institut für Zellbiologie des Nervensystems

(Univ.-Prof. Dr. Thomas Misgeld)

Imaging of mitochondrial redox signals in neuronal physiology and pathology

Dr. med. Michael Breckwoldt

Vollständiger Abdruck der von der Fakultät für Medizin der Technischen Universität München zur Erlangung des akademischen Grades eines

Doctor of Philosophy (Ph.D.)

genehmigten Dissertation.

Vorsitzender: Univ.-Prof. Dr. Claus Zimmer

Betreuer: Univ.-Prof. Dr. Thomas Misgeld

Prüfer der Dissertation:

1. Univ.-Prof. Dr. Martin Kerschensteiner, Ludwig-Maximilians-Universität München

2. Univ.-Prof. Dr. Thomas Korn

3. apl. Prof. Dr. Edgar Meinl, Ludwig-Maximilians-Universität München

Die Dissertation wurde am 23.9.2013 bei der Fakultät für Medizin der Technischen Universität München eingereicht und durch die Fakultät für Medizin am 18.2.2014 angenommen

Content

Abbreviations and symbols

AAV	adeno-associated virus
ALS	amyotrophic lateral sclerosis
BBB	Basso, Beattie and Bresnahan locomotor test
CNS	central nervous system
CFP	cyan fluorescent protein
DRG	dorsal root ganglion
DTT	dithiothreitol
EAE	experimental autoimmune encephalomyelitis
FAD	focal axonal degeneration
eGFP	enhanced green fluorescent protein
EGTA	ethylene glycol tetraacetic acid
FRET	fluorescence resonance energy transfer
GECI	genetically encoded calcium sensor
GERI	genetically encoded redox sensor
GFP	green fluorescent protein
HNE	trans-tetrahydroxy-dinonenal
ICN	intercostal nerve
IMM	inner mitochondrial membrane
ip	intraperitoneal
KX	ketamine xylazine
maCSF	mouse artificial cerebrospinal fluid
mito-Grx	*Thy1*-mito-Grx1-roGFP2
MnSOD	manganese superoxide dismutase
mPTP	mitochondrial permeability transition pore
MS	multiple sclerosis
NAC	N-acetyl-cystein
NMJ	neuromuscular junction
PBS	phosphate buffered saline
PFA	paraformaldehyde
OXPHOS	oxidative phosphorylation
PCR	polymerase chain reaction
PNS	peripheral nervous system
RFP	red fluorescent protein
ROI	region of interest
ROS	reactive oxygen species
SCI	spinal cord injury
TMRM	Tetramethylrhodamin-methylester
TTX	tetrodotoxin
UCP	uncoupling proteins
XFP	fluorescent protein
YFP	yellow fluorescent protein
Ψ	mitochondrial inner membrane potential

Abstract

Neurological diseases are often accompanied by neuronal loss. As neurons can only regenerate to a very limited extent, deciphering the mechanisms that cause neurodegeneration is an important step towards targeted therapies. Reactive oxygen species (ROS) have been implicated in neurodegeneration as possible molecular mediators of cellular damage. ROS are generated during the inflammatory burst of neutrophils and macrophages/microglia, as well as during mitochondrial oxidative phosphorylation. ROS can be detrimental to cells and tissues by oxidizing biomolecules like DNA, lipids or proteins, but can also act as cellular signaling molecules under physiological conditions. The study of ROS is notoriously difficult as ROS form intricate networks of short-lived and inter-convertible species. In addition, it was until recently not possible to directly visualize ROS and their effects *in vivo*.

In my thesis, I aimed to establish such *in vivo* methods in order to measure redox changes that are caused by ROS in intact neurons. For this purpose, together with my collaborators, I generated novel transgenic mouse lines (*Thy1*-mito-Grx1-roGFP2 and *Thy1*-mito-roGFP2-Orp1), which express redox sensors in their neuronal mitochondria. Additionally, I developed further strategies to co-visualize mitochondrial pH, calcium and potential dynamics. By using wide-field, confocal and 2-photon *in vivo* microscopy, I could quantify redox changes in single mitochondria under physiological conditions, as well as in mouse disease models of acute neurodegeneration (axon transection, nerve crush, spinal cord injury), chronic neurodegeneration (amyotrophic lateral sclerosis) and in neuroinflammatory conditions (experimental autoimmune encephalitis, a model of multiple sclerosis). I obtained the following results:

(1) Under physiological conditions and in the absence of neuronal activity, the mitochondrial glutathione pool is almost completely reduced, indicating that mitochondrial redox levels are tightly regulated and independent of organelle location or movement. When axons are electrically stimulated, the mitochondrial redox potential is elevated in axons and synapses. (2) Mitochondria in PNS and CNS axons show spontaneous redox signals, which are accompanied by reversible shape changes and that we dubbed “mitochondrial contractions”. During these contractions, mitochondria

transiently shorten by ~ 50% of their relaxed length and their glutathione pool reversibly oxidizes. A reversible drop of the mitochondrial inner membrane potential and a short alkaline spike of the matrix pH followed by a long-lasting matrix acidification accompany the contraction. Matrix calcium levels do not change detectably during the contraction. The frequency of mitochondrial contractions increases during extrinsic and intrinsic oxidative stress, as well as during electrical activity. (3) Mechanistically, complex I activity is necessary for the initiation of contractions, as well as for the oxidative shift of the redox potential. (4) Pharmacological manipulations inducing and blocking uncoupling proteins (UCPs) showed that these are activated during the contraction, and that these proteins sustain the long lasting drop in the mitochondrial inner membrane potential and the acidification. (5) In a mouse model of chronic neurodegeneration (amyotrophic lateral sclerosis, ALS), mitochondria show severe oxidative changes that correlate with the disease course. In affected mice, mitochondrial contractions are increased in frequency and last longer compared to littermate controls. (6) Under pathological conditions of acute neurodegeneration, *e.g.* during laser axotomy, as well as during crush injury to peripheral nerve axons, a spreading wave of mitochondrial oxidation is initiated at the injury site. In damaged axons, the mitochondrial contraction frequency is increased ~4-fold, before mitochondria round up and fragment permanently and acute axonal degeneration sets in. A number of mitochondria also show an increase in contraction length of which some become irreversible. (7) *In vivo* imaging during laser axotomy in the spinal cord of living mice established a similar sequence of events and revealed further mechanisms: First, the presence of extracellular calcium and its injury-induced influx into axons is necessary and sufficient to cause mitochondrial oxidation and rounding. Knockout of cyclophilin D, which is part of the mitochondrial transition pore, reduces the mitochondria pathology seen after axotomy. Preventing the oxidation of the mitochondrial glutathione pool by genetic or pharmacological means does not prevent mitochondrial shape changes.

Zusammenfassung

Neurologische Erkrankungen gehen häufig mit neuronalem Zelltod einher. Da Nervenzellen nur eine geringe Regenerationsfähigkeit besitzen, ist es wichtig die genauen Ursachen und Mechanismen für den Zelltod herauszufinden. Dies wäre auch ein erster möglicher Schritt hin zu spezifischeren Therapien. Reaktive Sauerstoffspezies (ROS) sind hoch reaktive Moleküle, die neurodegenerative Prozesse hervorrufen können. ROS entstehen während des „oxidativen Bursts" von neutrophilen Granulozyten und Makrophagen/Mikroglia sowie in der Atmungskette von Mitochondrien. Durch die Oxidation von DNA, Proteinen und Lipiden können ROS direkt Zellen und Gewebe schädigen. ROS fungieren aber auch als zelluläre Signalmoleküle. Die Untersuchung von ROS wird dadurch erschwert, dass ihre Halbwertzeit sehr kurz ist und sie schnell umgewandelt und abgebaut werden. Daher konnten ROS bisher nicht *in vivo* untersucht werden.

Das Ziel der hier vorgelegten Arbeit ist es, Methoden zur *In-vivo*-Messung von Redoxveränderungen und Radikalstress, die in physiologischen und pathologischen Situationen auftreten, zu entwickeln. Dafür habe ich in Kooperation neue transgene Mauslinien erzeugt (*Thy1*-mito-Grx1-roGFP2 und *Thy1*-mito-roGFP2-Orp1), die Redoxsensoren in neuronalen Mitochondrien exprimieren. Zudem kamen weitere Biosensoren zum Einsatz, um gleichzeitig ablaufende mitochondriale pH-, Potential- und Kalzium-Veränderungen zu quantifizieren. Durch den Einsatz von *In-vivo*-Mikroskopieverfahren konnte ich Redoxdynamiken in einzelnen Mitochondrien unter physiologischen und pathologischen Bedingungen messen. Es kamen Modelle von Rückenmarkstrauma, peripherer Nervenverletzung, Amyotropher Lateralsklerose sowie Multipler Sklerose zum Einsatz.

In meiner Arbeit habe ich folgende Ergebnisse erzielt:

(1) Unter Ruhebedingungen ist das mitochondriale Redoxpotential stark reduziert. Dieses ist genau reguliert und unabhängig vom Transportzustand von Mitochondrien. Bei elektrischer Aktivität des Axons steigt das Redoxpotential von axonalen und synaptischen Mitochondrien an. (2) Mitochondrien im ZNS und PNS zeigen spontane

Redoxsignale, die mit einer reversiblen Formveränderung einhergehen, die wir als „mitochondriale Kontraktionen“ benannt haben. Während der Kontraktionen verkürzen sich Mitochondrien reversibel um ~50% ihrer normalen Länge und oxidieren. Zudem fällt das Potential der inneren Mitochondrienmembran reversibel ab und es kommt zu einem schnellen pH Anstieg, der von einem lang anhaltenden pH Abfall gefolgt ist. Die Frequenz der Kontraktionen steigt bei oxidativem Stress und elektrischer Stimulation an und fällt bei Gabe von Antioxidantien ab. (3) Die Aktivität von Komplex I ist sowohl für die Initiation der Kontraktion sowie für den „oxidativen Burst" notwendig. (4) Durch pharmakologische Manipulationen konnte ich zeigen, dass „Uncoupling Proteine" während der Kontraktion aktiviert werden und für die lang-anhaltende mitochondriale Ansäuerung verantwortlich sind. (5) In einem chronischen neurodegenerativen Mausmodell der Amyotrophen Lateralsklerose (ALS) zeigen Mitochondrien im Erkrankungsverlauf zunehmend oxidative Veränderungen. Zudem finden sich gehäuft mitochondriale Kontraktionen von verlängerter Dauer. (6) Nach einer Axotomie als Modell einer akuten Neurodegeneration oxidieren Mitochondrien ausgehend von der Transektionsstelle. Die Anzahl der Kontraktionen nimmt hier um das ~4-fache zu, bevor Mitochondrien abrunden oder fragmentieren. (7) Durch *In-vivo*-Messungen konnte ich ähnliche Abläufe in einem Modell von Rückenmarkstrauma zeigen. Mechanistisch ist ein Kalzium-Einstrom in das Axon, ausgehend von der Transektionsstelle, hinreichend und notwendig, um die mitochondriale Pathologie auszulösen. Der Knockout von Cyclophilin D, einer Komponente der mitochondrialen „Transition Pore", verringert die mitochondriale Pathologie nach Axotomie. Die alleinige Blockierung der Oxidation durch Antioxidantien oder die genetische Überexpression von MnSOD verhindert die mitochondriale Abrundung nicht.

Introduction

Motivation

Neurological diseases are a tremendous burden for society and represent the 3rd leading cause of death worldwide. Due to the advances in the basic sciences in the “genomic” and “post-genomic” era, some progress has been made to understand the cellular and molecular causes of such diseases (Cowan et al., 2000; Jakovcevski and Akbarian, 2012; Misgeld et al., 2013). Mitochondria are crucial intracellular organelles that provide the vast majority of cellular ATP. Neurons with their particular high energy demand depend on proper mitochondrial function. Within the last decade mitochondrial dysfunction has shifted into the focus of neurological research being now implicated in the pathogenesis of almost all neurological diseases ranging from neurodegenerative to neuroimmunological and neurovascular disorders (Corrado et al., 2012; Dutta et al., 2006; Lin and Beal, 2006; Nicholls and Budd, 2000; Nunnari and Suomalainen, 2012). For instance: ~18% of familial forms of parkinsonism have been shown to be caused by mutations in the EB3 ligase Parkin, which controls mitochondrial quality and degradation (Abou-Sleiman et al., 2006; Chen and Dorn, 2013; Poorkaj et al., 2004). Mitochondrial calcium buffering is essential for neurons and dopaminergic neurons are particularly vulnerable to calcium perturbations in Parkinson models (Goldberg et al., 2012; Guzman et al., 2010; Surmeier et al., 2010). Mutations in the mitochondrial inner membrane fusion protein OPA lead to a hereditary form of optic atrophy. Similarly, mutations in the outer membrane protein MFN cause Charcot-Marie-Tooth neuropathy type 2a (Westermann, 2010). Furthermore, mitochondria have been implicated in the pathogenesis of Alzheimer's disease (Chen and Chan, 2009), amyotrophic lateral sclerosis (Lin and Beal, 2006) or multiple sclerosis (Lassmann et al., 2012; Corrado et al., 2012) - and are believed to be central regulators of normal ageing and life span (Batlevi and La Spada, 2011; Bratic and Larsson, 2013; Swerdlow, 2011; Vendelbo and Nair, 2011).

My host laboratory studies the role of mitochondria in neuronal development, neuroinflammation and neurodegeneration. Mitochondrial morphological alterations have been shown to precede focal axon degeneration in EAE and MS and thus might

represent a target for therapeutic intervention (Nikić et al., 2011). Mitochondrial transport, another key aspect of these organelles, that has pathomechanistic significance (Millecamps and Julien, 2013), was studied in a zebrafish tauopathy model (Plucinska et al., 2012) as well as in models of ALS (Marinkovic et al., 2012).

One caveat of previous studies was that so far only the morphology and transport of mitochondria could be used as a surrogate marker for their function based on the expression of fluorescent proteins in neuronal mitochondria (Chandrasekaran et al., 2006; Misgeld et al., 2007a). Given the importance of mitochondria in neuronal physiology and pathology and their involvement in cellular metabolism and signaling I wanted to establish novel tools that allow the assessment of mitochondrial morphology **and** function *in vivo*. To accomplish this task I have made use of a set of novel functional fluorescent probes that allow sensing the redox status as a measure of mitochondrial ROS production, as well as other key aspects of mitochondrial bioenergetics (membrane potential, pH, calcium content).

Mitochondria

Mitochondria are the “powerhouse” of the cell as they provide the vast majority of cellular ATP. Neurons actively downregulate glycolysis and thus depend on the lactate shuttle from astrocytes, which they use for mitochondrial oxidative phosphorylation (OXPHOS, Choi et al., 2012; Herrero-Mendez et al., 2009). Additional mitochondrial functions include β-oxidation of fatty acids, calcium-buffering and the control of apoptosis and necrosis (Hoppins and Nunnari, 2012; Lane, 2005; Scheffler, 2011; Vaseva et al., 2012). In neurons with their extraordinary long processes, mitochondria are actively transported into the anterograde and retrograde direction (Chang et al., 2011; MacAskill and Kittler, 2010). “Dysfunctional" or "aged” mitochondria are actively degraded in a process called “mitophagy” (Youle and Narendra, 2011). Not surprisingly, mitochondria are implicated in various pathological states including neurologic, cardiovascular, neoplastic and inflammatory diseases (Lin and Beal, 2006; Wallace, 2012; Ballinger, 2005; Corrado et al., 2012; Martínez, 2006; Nunnari and Suomalainen, 2012).

Next to their metabolic function, mitochondria have recently emerged as organellar signaling hubs, both in redox- as well as in calcium-mediated pathways (Al-Mehdi et al., 2012; Drago et al., 2012; Hamanaka and Chandel, 2010; Shutov et al., 2013). Mitochondrial redox signals can originate from the electron transport chain, which is located in the inner mitochondrial membrane. Superoxide (O_2^-) is produced mostly at complex I and III (Hirst, 2012; Murphy, 2009). Anti-oxidative enzymes, such as manganese superoxide dismutase or catalase are expressed in mitochondria in high levels and quickly degrade ROS (Ibrahim et al., 2000; Kiningham et al., 1999). ROS that escape these degradative pathways, and, for example, cause lipid peroxidation, constitute a signal that can be sensed inside and outside of the cell (*e.g.* by immune cells or other cell types (Al-Mehdi et al., 2012; Echtay et al., 2005; Niethammer et al., 2009; Weismann et al., 2011). Indeed, the exploration of redox signaling is a fast-growing field: Already with our current knowledge it is safe to predict that redox mediators (including ROS derived from mitochondria) play similarly important roles in cellular signaling as kinase- or calcium-mediated signals. In the next paragraph I will discuss in more detail the chemistry of ROS.

Reactive oxygen species

A potential mechanism of redox-mediated neuronal pathology is uncontrolled production of ROS leading to cellular demise. ROS are short-lived small molecules that originate from molecular oxygen. Through a one-step reduction of molecular oxygen, O_2^- is generated, which is further converted to hydrogen peroxide (H_2O_2), the hydroxyl radical ($OH^{\cdot -}$) and peroxynitrite ($ONOO^-$). Specific enzymes such as superoxide-dismutase have evolved to catalyze the degradation of O_2^- (Fig. 1). Radicals have an unpaired electron in their outer orbital. This renders them highly reactive as they try to obtain an electron from another molecule to fill their electron shell. This generates another radical, thus starting a chain reaction until the radical gets either degraded by specific enzymes or it pairs with another radical. Oxidative stress can be defined as a mismatch of ROS production and ROS degradation. Analyzing ROS and their effects is challenging because ROS are short-lived molecules that get degraded on the order of milliseconds.

ROS are secreted in high amounts by macrophages/microglia and neutrophils, but also originate from the electron transport chain of mitochondria during oxidative phosphorylation when electrons are directly transferred to molecular oxygen. This occurs especially at complex I and III and it is assumed that *in vitro* about 0.1 - 2% of the electrons form ROS during normal OXPHOS (Murphy, 2009). Currently it is unknown how much of the electron flux is converted into ROS *in vivo,* especially under pathological conditions when the electron transport chain is malfunctioning and the supply with redox equivalents such as NADH and FADH is not secured. It was the goal of this thesis to develop tools to quantify redox changes caused by ROS within mitochondria, as these organelles do not only release ROS, but are also prime targets of ROS mediated damage (Bartosz, 2009; Zorov et al., 2000). ROS have been suggested to cumulatively cause damage that leads to neuronal loss and thus represent a possible kick-off point that could be targeted for therapeutic interventions (Fatokun et al., 2008; Guzman et al., 2010).

The oxidative burst

The biological importance of ROS were first recognized around 1960 when the "oxidative burst" of phagocytes was discovered (Babior, 1984; Iyer et al., 1961). The activation of neutrophils or macrophages/microglia causes a massive up-regulation of their O_2 consumption – that is why the term "oxidative" or "respiratory burst" was coined. Later it was found out that the activation consists of the production of O_2^- and H_2O_2 mediated by the membrane-associated enzyme NADPH oxidase. The burst of O_2^- causes the subsequent generation of reactive halogens, such as hypochlorous acid ($HOCl^-$) catalyzed by myeloperoxidase, and other radicals, such as $OH^{\cdot -}$ that can oxidize lipids and proteins within bacterial membranes. This renders the membrane porous and thus has antimicrobial effects. This oxidative attack is not spatially directed nor target-specific and thus has potentially detrimental effects on host tissues.

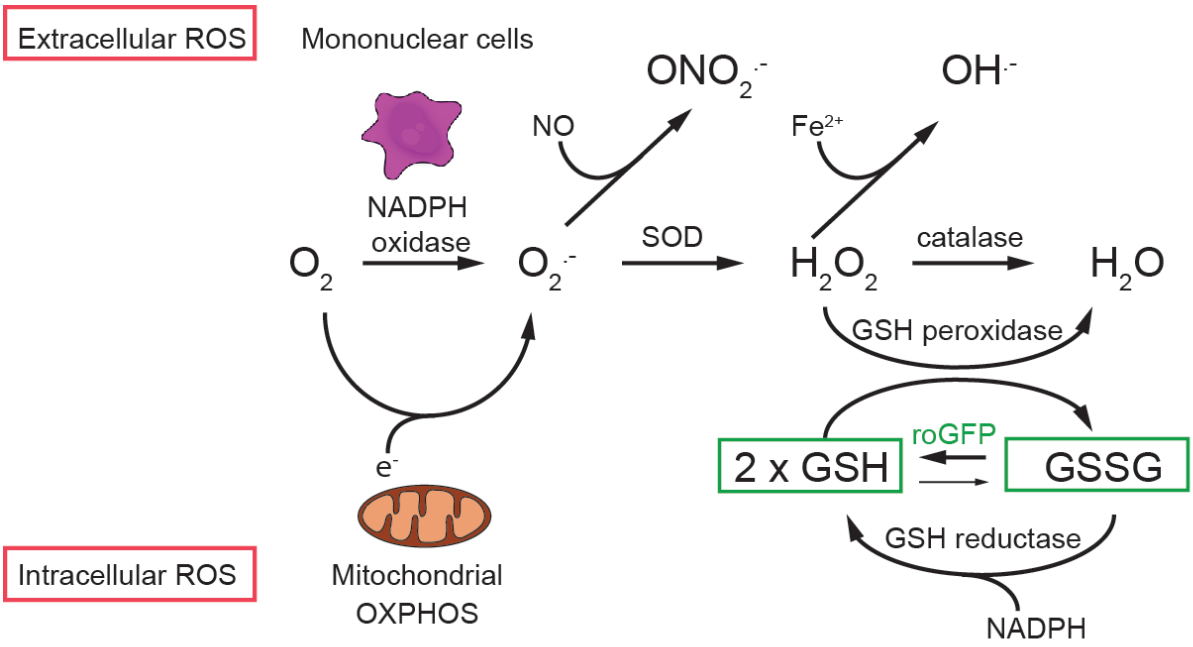

Figure 1: Model of ROS production and degradation
ROS can be generated during the oxidative burst of mononuclear cells like macrophages or neutrophils ("extracellular ROS") or during oxidative phosphorylation of mitochondria (OXPHOS, "intracellular ROS"). The highly reactive superoxide anion ($O_2^{\cdot-}$) is generated by the one-step reduction of O_2. $O_2^{\cdot-}$ can be degraded to H_2O_2 by SOD. H_2O_2 is detoxified to H_2O by catalase or glutathione (GSH) peroxidase. But also other harmful ROS, like peroxynitrite (ONO_2^-) or the hydroxyl radical ($OH^{\cdot-}$), can originate from $O_2^{\cdot-}$ and H_2O_2, respectively. GSH is part of the oxidative defense system and serves as an electron donor in order to detoxify H_2O_2 by the oxidative formation of a disulfide bond between two GSH molecules. Redox sensitive GFP (roGFP) senses the redox potential of glutathione. (E_{GSH}). Under physiological conditions the pool of GSH is almost completely reduced. Figure is modified from Dröge, Physiol. Rev., 2002.

Redox signaling

Apart from these "destructive" effects, it has been recognized over the past decade that ROS constitute an important signal transmitting information that can be sensed within the cell (Dröge, 2002; Murphy et al., 2011). Three major types of redox switches have been described which include glutathione (GSH and GSSG), thioredoxin (Trx1-(SH_2) and Trx1-(SS) and cystein (CySH and CySS, Hansen et al., 2006). These redox pairs serve as electron donors and acceptors and can be used to specifically reduce or oxidize target proteins. Literally hundreds of proteins have been identified that are

regulated by reversible oxidation or reduction of cystein residues (Herrmann and Dick, 2012). Disulfide bridge formation can lead to tertiary structure rearrangement and alter the activity of a protein. Thus ROS-mediated oxidation acts as an important posttranslational modification similar to phosphorylation or sumoylation. For example, nuclear transcription factors such as zinc-finger proteins are impeded in their activity upon oxidation and a reduced nuclear GSH pool is required to keep them fully active (Kröncke, 2001; Wilcox et al., 2001). Under pathological conditions it has been well documented that ROS formation can trigger the production of pro-inflammatory cytokines (Naik and Dixit, 2011; Zhou et al., 2010). Recently it was shown that reactive nitrogen species can specifically modify a single residue of complex I (Cys39) which gets exposed during myocardial ischemia. This modification (s-nitrosation) down-regulates the activity of complex I during reperfusion, thus prevening additional ROS production (Chouchani et al., 2013).

To balance redox signals and counteract possible aversive effects of ROS a number of antioxidative mechanisms have evolved. These include enzymes like superoxide-dismutase, catalase and myeloperoxidase. Additionally, small molecule scavengers like glutathione are present in the cytoplasm, as well as in several cellular organelles (nucleus, mitochondria) to preserve a physiological redox equilibrium. GSH consists of only 3 amino acids (glutamine, cysteine, glycine). Two GSH molecules can form a disulfide bridge upon oxidation and serve as an electron donor to detoxify radicals. The reaction is catalyzed by glutaredoxin. The reversible oxidation of thiol groups and the catalysis of this reaction by glutaredoxin have been utilized to construct redox-sensitive fluorescent sensors such as roGFP and its improved version, Grx1-roGFP2.

Synthetic dyes for redox imaging

Important redox-sensitive dyes include MitoSox (Invitrogen, reactive to $O_2^{-\cdot}$) and dichlorofluorescein (H_2DCF, reactive to several ROS). MitoSox is taken up by mitochondria and increases strongly in fluorescence upon oxidation by superoxide and by other ROS to a lesser degree (Robinson et al., 2008). H_2DCF is esterified after cellular uptake and accumulates in the cytoplasm. It is non-fluorescent in its reduced

form. Oxidation - presumably by any one of a number of different kinds of ROS - results in the highly fluorescent end product DCF. Even though H_2DCF is not targeted to mitochondria directly, it is often used as read-out of mitochondrial function, as mitochondria are considered to be the primary intracellular source of ROS. Unfortunately, a number of limitations exist with synthetic dyes. Targeting of these dyes to specific compartments of the cell without disrupting cellular function is difficult. Many studies are performed *in vitro* with isolated mitochondria or in cell culture, where dye delivery is less problematic. *In vivo* measurements however are often hampered by low loading efficacy due to poor penetration or unspecific staining by these lipophilic dyes (Romanelli et al., 2013). It also remains a challenge to ascertain the specificity of the dye towards one reactant (Karlsson et al., 2010). Additionally, most dyes are non-ratiometric and/or are irreversibly modified (MitoSox) making dynamic time-lapse measurements impossible. To overcome these problems, functional proteins have been engineered, which promise to greatly advance our knowledge of mitochondrial function and their role in redox signaling (Akerboom et al., 2013; Meyer and Dick, 2010).

Genetically encoded redox sensors

ro-GFP

Redox-sensitive GFP (ro-GFP) was first developed by the groups of Nobel laureate R. Tsien and S. Remington by mutating the green fluorescent protein (Dooley et al., 2004; Hanson et al., 2004). Two cystein residues were engineered into the beta sheet backbone of GFP close to the chromophore, which renders GFP redox-sensitive. Several publications proved its utility to measure the redox potential in different compartments (mitochondria, endoplasmic reticulum, cytosol) and systems (plants, cell lines, neurons; Guzman et al., 2010; Schwarzländer et al., 2009; van Lith et al., 2011; Xie et al., 2013) but two problems remained: first, the reaction kinetics for oxidizing and reducing roGFP are relatively slow (on the order of minutes), as the reaction is not catalyzed by an enzyme. Even more importantly, the oxidation and reduction cannot be attributed to a specific oxidative species (in other words: linked to a specific redox pair) making it difficult to interpret the signal.

Grx1-roGFP2

To overcome this problem the laboratory of T. Dick (collaborating partner at DKFZ, Heidelberg) developed Grx1-roGFP2 (Gutscher et al., 2008) by fusing roGFP2 with the human enzyme glutaredoxin 1 (Grx1, Fig.2 a-c). This accelerates the reversible oxidation and reduction by an order of magnitude. Also, Grx1-roGFP2 reports specifically the glutathione redox potential (E_{GSH}). The dynamic range was reported *in vitro* as ~2.6 (Gutscher et al., 2008) and *in vivo* as ~5 (Albrecht et al., 2011). This is still less than the novel generations of *e.g.* calcium indicators (see bellow) and engineering newer versions with higher dynamic ranges would be desirable, especially for *in vivo* applications where signals might be more difficult to detect. Importantly, it was shown that Grx1-roGFP2 is insensitive to pH changes in the physiological range between 5.5 to 8.5 (Gutscher et al., 2008).

Making use of this concept of enzyme-coupling roGFP2, other enzymes can be used to render roGFP2 specific to other oxidants. For example, a direct H_2O_2 sensor was engineered by fusing the H_2O_2-sensing protein Orp1 from yeast to roGFP2 creating the roGFP2-Orp1 sensor (Gutscher et al., 2009).

cpYFP and HyPer to detect O_2^- and H_2O_2

Other redox sensitive proteins include the circular-permutated YFP (cpYFP) and the derivative HyPer (Belousov et al., 2006; Hou et al., 2013; Wang et al., 2008). CpYFP was proposed to react specifically to O_2^-, even though there has been some debate over the nature of the signal, as it was demonstrated that cpYFP also strongly reacts to pH changes (Schwarzländer et al., 2011; Wei-LaPierre et al., 2013). HyPer is also a circular permutated YFP fused to the H_2O_2-sensitive protein Oxy-R from *E.coli*. Ocy-R has two oxidation-sensitive cystein residues which lead upon oxidation to a conformational change of the sensor (Belousov et al., 2006; Love et al., 2013; Niethammer et al., 2009). HyPer has been reported to be pH-sensitive, too. In how far the detected HyPer signals could be “contaminated” by possible pH alterations is a matter of debate.

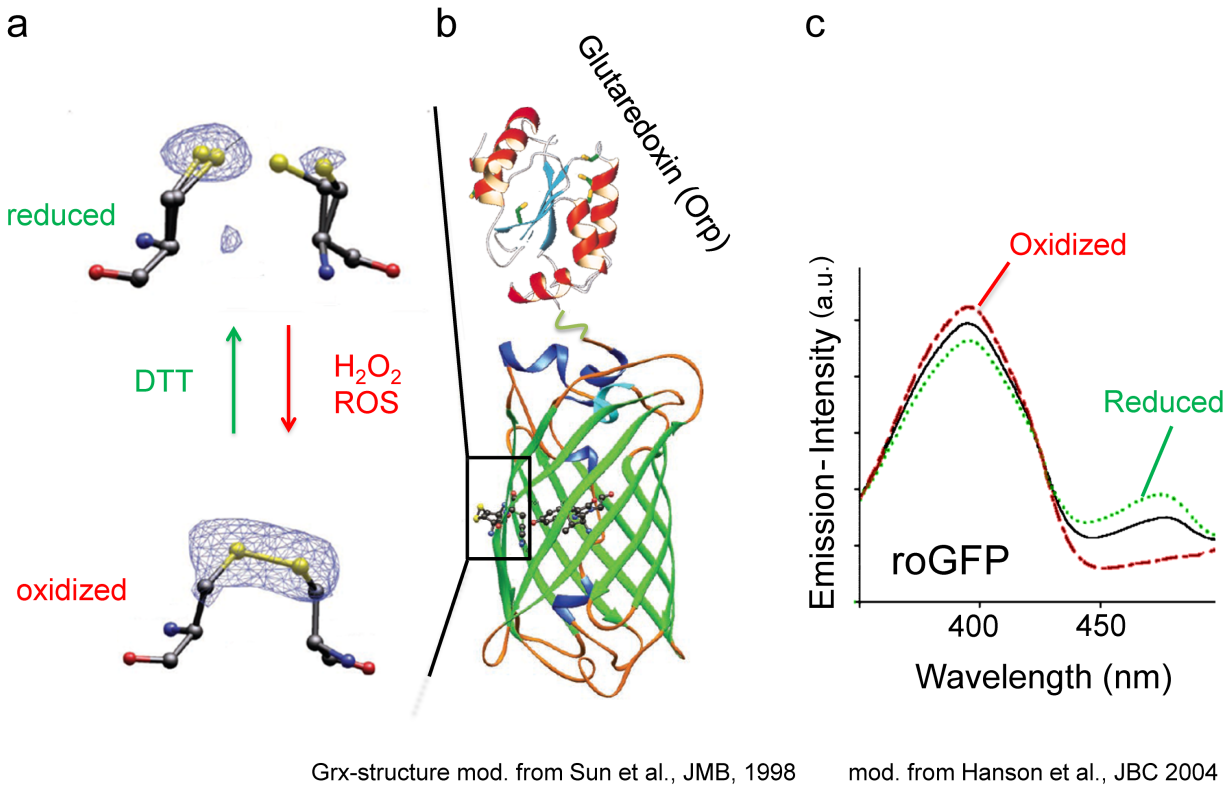

Figure 2: Model and mechanism of Grx1-roGFP2 imaging
(**a,b**) Redox sensitive GFP (roGFP) possess two cystein residues, which can be reversibly oxidized and reduced (**a**). Experimentally DTT acts as an electron donor and is used for the reduction of cystein residues. H_2O_2 or ROS can lead to the oxidation of cysteins and the formation of a disulfide bridge. In the roGFP protein, two cystein residues have been engineered into the β-sheet backbone of GFP in close proximity to the three amino acids Ser_{65}-Tyr_{66}-Gly_{67} that constitute the fluorochrome of GFP (Hanson et *al*., 2004; Dooley et *al*., 2004). roGFP has been modified by the addition of human glutaredoxin 1 (Grx or Orp1) to speed up the reaction kinetics and to make the reaction specific to sense the glutathione redox potential E_{GSH}; Gutscher *et al*., 2008) or the production of H_2O_2 (Gutscher *et al.*, 2009; **b**). (**c**) Oxidation/reduction changes the fluorescence properties of roGFP. Its fluorescence emission-intensity increases upon oxidation at ~405 nm and decreases at ~488 nm excitation and *vice versa* upon reduction. This enables excition ratiometric measurements by scanning with 408 and 488 nm sequentially.

pH sensors

A number of other molecular sensors that can be applied to characterizing mitochondrial function have been recently developed. This includes the pH sensors, pHred (Tantama et al., 2011) and SypHer (Poburko et al., 2011). SypHer is a variant of HyPer, in which

one of the cystein residues has been mutated to render the protein purely pH-sensitive and abolish the reactivity towards H_2O_2 (Poburko et al., 2011; Santo-Domingo et al., 2013). Mitochondrial pH is mostly affected by proton export from the mitochondrial matrix at complexes I, III and IV and by the re-entry into the matrix at complex V (ATP synthase). The mitochondrial pH is very dynamic and a marker of respiratory activity. The resting matrix pH is ~7,8. It can rise to values above 9 upon activation of the electron transport chain. Contrary, the mitochondrial proton gradient quickly dissipates upon mitochondrial damage leading to mitochondrial acidification.

Calcium sensors

Another exciting field of molecular sensors are genetically-encoded calcium-sensors (GECI; Grienberger and Konnerth, 2012). Calcium fluxes in neurons are widely used as a surrogate marker of neuronal activity. But obviously, GECIs can also be used to detect calcium-mediated second messenger signals or pathological calcium elevations. Over the past years different classes of GECIs have been developed to cover broad ranges of sensitivity and to increase their dynamic range. GECIs are either based on fluorescence resonance energy transfer (FRET) or single fluorophore sensors with a calcium-binding domain. One example of a FRET sensor is CerTN and its improved version TnXXL. TnXXL contains a CFP/YFP (cyan/yellow fluorescent protein) pair, connected by a calcium-binding troponin-c linker (Heim et al., 2007; Jares-Erijman and Jovin, 2003; Mank et al., 2008). Troponin-c is a calcium-binding protein in muscle that is not expressed in neurons. Upon calcium binding to troponin-c, the sensor undergoes a conformational change that brings the fluorescent moieties in close proximity. This allows direct energy transfer between CFP and YFP resulting in an increase of FRET efficiency. Another approach is used in the GCaMP family of calcium-sensors. This class of sensors is based on a circularly mutated form of eGFP, which is fused to the calcium-binding protein calmodulin. GCaMP exhibits a conformational change upon calcium-binding to calmodulin, resulting in a strong increase in eGFP fluorescence. The newer generations of GCaMPs have been shown to be suitable to detect single action

potentials (Tian et al., 2009; Zariwala et al., 2012). GECIs however have not been used extensively to detect other forms of calcium signals.

Protein engineering of GCaMPs has led to an amazing improvement of the dynamic range which is well above 10 (F/F_0) and to an expansion of the available color-palette, spanning now a large part of the visible spectrum (Akerboom et al., 2013; Zhao et al., 2011). This has been a joint scientific effort for the past decade (Pologruto et al., 2004) that resulted in an ~10 fold increase of the dynamic range. Also, the notorious pH sensitivity of GCaMPs has been tackled in the latest generations of rGECOs (Akerboom et al., 2013). Still, the pH sensitivity of *e.g.* GCaMP-3 makes measurements in mitochondria with their fluctuating pH difficult as GCaMPs become brighter at more alkaline pH, thus falsely mimicking calcium signals.

Despite the problems described, molecular biological, biochemical and biophysical approaches have yielded a striking toolbox of sensors in order to read out a manifold of molecular signals. These sensors have the potential to transform our understanding of physiological and pathological processes.

Spinal cord injury

Spinal cord injury (SCI) is a debilitating disease resulting often from high-speed acceleration trauma. SCI affects mostly young adults (McDonald and Sadowsky, 2002). The pathophysiology of this condition is complex, involving primary and secondary processes. The initial tissue damage - typically a compression injury - leads to acute axon transection, glial cell death, bleeding and tissue ischemia. This results in a secondary inflammatory reaction that in itself has beneficial and detrimental effects. SCI is particularly devastating as CNS neurons have only a very limited capacity to recover or regenerate after injury (Bareyre, 2008; Ertürk et al., 2011). Up to now, no causal treatment exists (Filli and Schwab, 2012). In my thesis I used models of spinal cord and peripheral nerve injury mimicking the initial phase of the disease in order to understand how the primary injury leads to mitochondrial damage and neuronal loss. I chose an injury paradigm, in which the axotomy is induced with a femto-second pulsed

titanium:sapphire laser (Steinmeyer et al., 2010). The laser induces a very controlled transection of axons, which leads to acute axonal and Wallerian degeneration. Certainly, this model does not recapitulate the entire complexity of SCI, but it can serve as a model for acute neuronal injury. It also provides unprecedented precision and allows comparing transected and untouched axons side-by-side.

Amyotrophic lateral sclerosis

Amyotrophic lateral sclerosis (ALS) is a chronic neurodegenerative disorder that involves the upper and lower motor neuron located in the primary motor cortex and the ventral horn of the spinal cord. This results in the degeneration of the corticospinal tract (Pasinelli and Brown, 2006). As all motor neurons can ultimately be affected including the neurons innervating the diaphragm, patients usually die of respiratory failure within five years after symptom onset. No cure is available to this day, and prognosis is poor as breathing and swallowing muscles are affected early in the disease course. 10% of ALS cases are familial with an autosomal-dominant inheritance pattern. I used the SOD^{G93A} mouse model, which carries a human mutation in the Cu^{2+}/Zi^{+} superoxide dismutase gene - mutation of glycine changed to alanine at position 93. Mutations in the SOD1 gene cause ~20% of familial ALS cases. To assess mitochondrial redox dynamics and their role in the disease process, SOD^{G93A} mice were crossed to mitochondrially-labeled mouse strains.

Multiple sclerosis

Multiple sclerosis (MS) is one of the most common reasons for disability in young adults (Hemmer et al., 2006; Nylander and Hafler, 2012). The disease was initally described by the French neurologist Jean-Martin Charcot in 1868. Hallmarks of its pathogenesis include demyelinating inflammatory plaques, as well as axonal degeneration in the central nervous system (Frohman et al., 2006; Kuhlmann et al., 2002). Whereas demyelination with the influx of inflammatory cells has been recognized as an important feature of the disease for decades, axonal degeneration and neuronal loss have only recently shifted (again) into the focus of research (Friese et al., 2007; Trapp and Nave,

2008). A novel mechanism of axonal degeneration named "focal axonal degeneration" (FAD) was recently described in our laboratory (Nikić et al., 2011). It consists of three sequential stages of axonal pathology. First normal appearing axons (“stage 0”) undergo focal swellings ("stage 1"). Subsequently, some of the swollen axons break and degenerate ("stage 2"). At least the initial swelling can be reversible, thus establishing a potential target for therapy. So far the underlying mechanisms triggering FAD remain unknown, but it has been shown that exogenous application of H_2O_2 or NO donors can start a process mimicking FAD. Also ROS scavengers can ameliorate FAD in an animal model of MS indicating that FAD might be a redox sensitive process.

The animal model of MS, which I also used in my studies, is known as “experimental autoimmune encephalomyelitis" (EAE). EAE is induced by immunizing mice with myelin components (MOG peptide, residues 35 to 55, emulsified in Freund`s adjuvant, supplemented with Mycobacterium tuberculosis extract). This emulsion is injected into the flanks of the anesthetized animal in conjunction with an intraperitonal (ip) injection of pertussis toxin. After a preclinical phase of 10 days mice develop a monophasic disease with paralysis characterized by neuroinflammatory infiltrates, demyelination and axonal degeneration in the spinal cord. EAE closely mimics the pathological hallmarks of MS, even though - depending on the immunization protocol and the genetic background of the animals used - some aspects (*e.g.* inflammation) can be more pronounced in a given EAE model than others (*e.g.* demyelination; Ransohoff, 2012; Wekerle et al., 2012).

Materials and Methods

Constructs and plasmids

CMV-Grx-roGFP2, *CMV*-mito-Grx-roGFP2 (Gutscher et al., 2008) and *CMV*-roGFP2-Orp1 plasmids (Gutscher et al., 2009) were obtained from T. Dick (DKFZ, Heidelberg). HyPer (Belousov et al., 2006) was bought from Evrogen (Moscow). RGECO1 and GCaMP3 were obtained from Addgene (Cambridge, USA). SypHer (Poburko et al., 2011) was a kind gift of N. Demaurex (University of Geneva). For mitochondrial targeting of fluorescent proteins (XFPs) the targeting sequence from ATP synthase protein 9 (*Neurospora crassa*) was used for roGFP2 constructs. All other constructs were cloned under the targeting sequence of human cytochrome oxidase VIIIB (Misgeld et al., 2007a). Standard molecular biology techniques were used to perform sub-clonings. Vector NTI software (Invitrogen, Carlsbad) was used to plan cloning strategies.

Transgenic mouse lines

Thy1-TnXXL mice were obtained from O. Griesbeck (Max Planck Instiute for Neurobiology, Martinsried; Direnberger et al., 2012; Heim et al., 2007). MnSOD overexpressing mice were obtained from D. St. Clair (Ibrahim et al., 2000; Kiningham et al., 1999). Cyclophilin D knockout mice were bought from the Jackson Laboratory (Bar Habor; Schinzel et al., 2005). MnSOD and Cyclophilin D mice were crossed to *Thy1*-mito-Grx1-roGFP2 mice.

Cell culture

Hek-293 cells were cultured using standard conditions. Cells were grown in Dulbecco's Modified Eagle Medium (DMEM, Invitrogen) substituted with 10% fetal bovine serum and 1% normocin or penicillin/streptomycin. For testing fluorescent sensors, cells were grown on poly-l-lysine coated glass cover slides using cloning cylinders to reduce media volumes needed for transfection. For transfections 500 ng plasmid DNA of a given

construct were mixed with 0.5 µl lipofectamine (Invitrogen) and diluted in 500 µl PBS for an incubation period of 10 min at room temperature. 500 µl of the mixture was added on top of the cells and left on for 2 to 5 hours. Afterwards the glass cylinders were gently removed without disrupting the adherent cells and 1 ml DMEM was added. The cells were grown for 1-3 days to express the construct before imaging experiments were performed. Expression efficiency improved over time and was found to be optimal on days 2 and 3 post transfection when more than ~30% of cells expressed the fluorescent protein.

In vitro characterization of molecular sensors

For cell culture imaging experiments the glas cover slips with transfected HEK-293 cells were gently transferred to a heated flow chamber (33-35 °C) and continuously perfused with carbogen-bubbled normal Ringer. Drugs (H_2O_2, DTT) were administered through the perfusion system. Widefield (BX-51, Olympus) and confocal microscopy (FV-1000, Olympus) were performed using 488 nm or 408/488 nm excitation.

Cloning of transgenic constructs and generation of transgenic mouse lines

Thy1-mito-Grx1-roGFP2 and *Thy1*-mito-roGFP2-Orp1 mouse lines were generated by pronuclear injections (in cooperation with R. Naumann, MPI for Molecular Cell Biology and Genetics, Dresden). The Thy1 promotor was used to drive the expression of the sensor in the nervous system (Feng et al., 2000). The mitochondrial targeting sequence from ATP synthase protein 9 (*Neurospora crassa*) was cloned upstream of Grx1-roGFP2 to specifically target the XFP to mitochondria (kind gift by our cooperating partner T. Dick, DKFZ, Heidelberg). Eleven founders lines for each construct were screened for XFP expression in the intercostal nerve and in the central nervous system (cortex, hippocampus, cerebellum, retina, spinal cord). Three lines of the *Thy1*-mito-Grx1-roGFP2 animals (“mito-Grx mice”) and one line for *Thy1*-mito-roGFP2-Orp1 were selected for further experiments and bred in our animal facility. These lines showed the highest expression of the XFP and broad labeling density (>75% of neurons).

Anatomical and behavioral characterization

Thy1-mito-Grx1-roGFP2 transgenic animals were tested for possible behavioral and neurological abnormalities using morphological (mitochondrial shape factor, mitochondrial density in axons, mitochondrial transport, muscle diameter, mitochondrial density in neuromuscular junctions, size of the NMJ) and behavorial tests. Anatomical assessment was performed in the triangularis sterni explant. The Basso, Beattie and Bresnahan locomotor test for mice (Basso et al., 1995) and the gridwalk test (Pearse et al., 2007) were used as behavioral tests. Transgene-negative littermates or mito-CFP animals served as controls. Two independent blinded observers (M. Breckwoldt and G. Heitmann, technician, M. Kerschensteiner lab, LMU Munich) scored the animals in the behavioral tests blinded for the animals` genotype.

Morphological characterization

For tissue analysis, mice were transcardially perfused with 4% (wt/vol) paraformaldehyde (PFA) diluted in 1xphospahte buffered saline (PBS) and post-fixed for 24 h in 4% PFA in PBS. Following dissection, the tissue of interest (brain, spinal cord and eye) was prepared for cryosectioning by incubation in 30% sucrose (Sigma). 20 to 50 µm sections were stained either with Neurotrace 640/660 (Molecular Probes, diluted 1:500) to label cell bodies and nuclei or with Alexa594-conjugated α-bungarotoxin (Invitrogen, diluted 1:50 in PBS) to visualize acetylcholine receptors at the neuromuscular junction (NMJ). Muscle fibers were counterstained with phalloidin conjugated to Alexa Fluor 635 (Invitrogen). Tissue sections were mounted in Vectashield (Vector Laboratories) and image stacks were recorded using an FV1000 confocal microscope (Olympus) equipped with x20/0.8 N.A. and x60/1.42 N.A. oil-immersion objectives. Analysis of muscle diameter and - area, NMJ size, mitochondrial shape factor and mitochondrial density was performed in triangularis sterni explants. Transgene-negative littermates or aged-matched mito-CFP animals served as controls. Whole mount preparations of the excised spinal cord were performed by embedding the post-fixed spinal cord on a cover slip in a drop of 2 % agarose in PBS. This whole mount

preparation was imaged upside down on a FV1000 confocal microscope (Olympus). For correlation with *in vivo* imaging the induced laser lesion was identified by its bright autofluorescence at 488 nm and the vascular pattern of the spinal cord serving as landmark structures.

Functional characterization

Explants of the triangularis sterni muscle were prepared as previously described (Kerschensteiner et al., 2008). Mice were euthanized with isoflurane and the rib cage (with the attached triangularis sterni muscle and its innervating intercostal nerves) was isolated by paravertebral cuts, pinned in a Sylgard-coated dish using insect pins and maintained on a heated stage (32-35°C) in normal Ringer solution, bubbled with carbogen gas (95%O_2, 5%CO_2). Recordings were performed in proximal or distal intercostal axons or at the NMJ. Axonal transport was measured as previously described (Kerschensteiner et al., 2008). To record the mitochondrial glutathione redox potential in motor axons and NMJs, a BX51 wide-field microscope (Olympus) was used, equipped with x20/0.5 N.A. and x100/1.0 N.A. dipping-cone water immersion objectives, a filter wheel with shutter, a dichroic filter (D/F 500 DCXR ET 525/36), a Polychrome V polychromator system (Till Photonics) and a cooled CCD camera (Sensicam, pco imaging) controlled by TillVision software. Images were acquired at rates of 0.5 or 1 Hz with exposure times of 150 ms for 408 nm excitation (1500 ms for mito-roGFP2-Orp1) and 30 ms for 488 nm excitation (400 ms for mito-roGFP2-Orp1). To measure the dose-response of the sensor proteins, triangularis sterni explants were incubated with exogenous H_2O_2 (Sigma; concentration of 6.25, 12.5, 25, 50, 100, 200, 400, 800, 1000 µM H_2O_2 diluted in normal Ringer solution) or dithiothreitol (DTT; Sigma or VWR; concentration of 500 µM diluted in normal Ringer solution) for 5 minutes. Images of NMJs (3-10 NMJs per concentration, per animal) were acquired by taking single frame images with 408 and 488 nm excitation. To measure the physiological state of the mitochondrial glutathione redox potential in axons, time-lapse movies in intercostal nerves were recorded for 5 to 10 minutes at 0.5 or 1 Hz.

Electrical stimulation of the peripheral nerve

Electrical stimulation of the intercostal nerve was performed in triangularis sterni explants using a custom-built suction electrode. The intercostal nerve was carefully dissected over a short distance of ~2 mm at the proximal end of the ribcage. The isolated end of the nerve was sucked smoothly into the electrode without stretching the nerve and stimulated at 1 and 10 Hz, respectively using a Master 8 pulse generator (stimulation settings: 70 V pulse, 0.5 ms duration; A.M.P.I, Jerusalem). In order to paralyze the muscle during the stimulation and prevent movement artifacts, 0.2 µM tubocurarin was added to normal Ringer solution and incubated for 30 min. To control for the specificity of the stimulation effect, 1 µM tetrodotoxin (TTX; Abcam, Cambridge, UK) was added into the bath in some experiments to block action potential conduction. Redox measurements were performed in proximal intercostal nerve axons and at the NMJ with the same imaging settings described above. To determine the length of the stimulation effect time-lapse movies were taken for 1 hour at a frame rate of 1 Hz with an intermittent stimulation period of 10 Hz for 10 minutes.

Measurements of the mitochondrial inner membrane potential

To analyze the mitochondrial membrane potential, the potential sensitive dye tetramethylrhodamine methyl ester perchlorate (TMRM, Invitrogen; Chazotte, 2011; Nicholls and Ward, 2000) was loaded into intercostal nerve axons. TMRM is membrane permeable and accumulates in the mitochondrial matrix in a potential-dependent manner due to its positive charge. The mitochondrial matrix has a negative charge due to its proton and electrical gradient generated by the electron transport chain and accumulates cations. As TMRM is only ineffectively taken up after bath application, the dye was directly applied on one of the intercostal nerves after surgical exposure. The exposed nerve was covered with an absorbable gelatin sponge (Spongostan, Johnson and Johnson) soaked in TMRM, which was left in place after closing the surgical opening. To expose an intercostal nerve, animals were anesthetized with ketamine/xylazine (KX) and the fur of the thorax was removed. After a longitudinal

incision, the 3rd and 4th intercostal nerve of *Thy1*-mitoGrx1-roGFP2 and mito-CFP mice was exposed in the axillary line. The pectoralis muscle was split and the intercostal space was carefully dissected without damaging the nerve or the pleura. A gel foam pad soaked with 2.5 µl of TMRM (stock concentration: 25 mM in DMSO) was implanted onto the intercostal nerve. The pectoralis muscle was sutured above the foam pad to secure it in place using 6-0 monofilament sutures. The skin was closed with metal clips and cleaned with 80% ethanol. Mice were allowed to recover in a pre-heated chamber and monitored daily for signs of discomfort. Triangularis sterni explants were prepared 1-7 days after gel foam implantation. The mitochondrial membrane potential of single mitochondria was assessed in proximal intercostal nerve axons in addition to the glutathione redox potential or in mito-CFP animals. Triple wavelength imaging with a triple-dichroic filter set was performed (DAPI/ FITC/ TRITC filter set, F66-000; AHF Analysetechnik) using excitation wavelengths at 408, 488 and 550 nm or dual wavelength imaging with excitation wavelengths at 440 and 570 nm (CFP/ YFP/ DsRed filter set; AHF Analysetechnik). Exposure times varied between different TMRM experiments due to different loading efficiencies of the dye but was tried to be kept to a minimum (between 50-150 ms) as TMRM is a photosensitizer that can lead to phototoxicity. Movies were recorded for 5-10 minutes at 0.5 Hz.

AAV production and spinal cord injection of viral constructs

The cloning of the AAV expression constructs and the production of the AAVs was kindly performed by Anja Schmalz (technician, Kerschensteiner lab) with additional help from Dr. L Godinho (TUM) and Dr. Florence Bareyre (LMU). Mitochondrial targeted constructs were cloned into the CMV early enhancer/chicken beta actin vector (CAG, Addgene, Cambridge, USA). Adeno-associated virus 1/2 production was performed using standard methods. AAV-293 cells (10^6 per 14 cm plate; Invitrogen) were grown in 10 ml DMEM. AAV DNA was transfected on day two using $Ca^{2+}Cl_2^-$. Cells were grown for additional 3 days until the virus was harvested. After harvesting and purification, the virus was titrated by quantitative RT-PCR following an established protocol (Veldwijk et al., 2002). The following primers for the pAAV Cag vector amplification were used:

forward primer: 5‘-TTA CGG GGT CAT TAG TTC ATA GCC CA-3‘; reverse primer: 5‘-CAA TGG AAA GTC CCT ATT GGC GTT AC-3‘. The titers of the virus preparations used here were between 1.01 - 2.68 x 10^{11} viral particles/ml.

For labeling intercostal axons, AAV virus particles were stereotactically injected into the spinal cord. The injections were performed mainly by Peter Bradley, Ph.D (Kerschensteiner lab, LMU). Animals were anesthetized with KX and a one-level laminectomy was performed of cervical vertebra 7. AAV (0.5 µl, diluted 1:2 or 1:4 in sterile PBS) was stereotactically injected uni- or bilaterally over 10 minutes into the cervical spinal cord beween cervical vertebra 7 and thoracic vertebra 1. The coordinates were 0.3 mm lateral of the dorsal vein and 0.6 mm below the dorsal surface of the spinal cord targeting the α-motor neurons of the ventral horn. The neck muscles were loosely adapted with sutures and the skin was closed with metal clips. Animals were allowed to recover in a pre-heated chamber and monitored daily for any apparent signs of discomfort or neurological deficit. Triangularis sterni explants were prepared 14 to 28 days post AAV injection and the expression and possible toxicity of the virus was assessed in spinal cord tissue sections and in the triangularis sterni explant. The expression level of the AAVs was found to be stable for at least ~6 weeks.

Pharmacological manipulations

To mechanistically dissect mitochondrial contractions, I used a set of pharmacological manipulations targeting different mitochondrial pores and channels. 100 µM genipin (UCP inhibitor, Sigma), 35 µM HNE (UCP inducer, Merck Millipore), 20 µM cyclosporin A (inhibitor of the mitochondrial transition pore, Sigma), 1 µM MitoQ (inhibitor of lipid peroxidation, kind gift of M. Murphy, University of Cambridge) and 100 µM ru360 (inhibitor of the mitochondrial uniporter, Santa Cruz Biotechnology) were used. Stock solutions were prepared in DMSO and stored at -20 °C. Working solutions were prepared in normal Ringer at the day of the experiments. Drugs were bath applied to triangularis sterni explants and incubated for 30 min. Redox imaging was performed in axons close to the NMJ as these fibers run superficially and are thinner myelinated, thus pharmacological access is better than in the proximal intercostal nerve. Imaging was performed with the settings described above. Movies were recorded for 5 min at 1 Hz.

In vivo two photon imaging of mitochondrial redox changes after axotomy

To image mitochondrial redox changes in spinal axons, a spinal cord imaging technique was adapted (Kerschensteiner et al., 2005; Misgeld et al., 2007b). Animals were anaesthetized by intraperitonal injection of KX and the spinal cord was surgically exposed by a lumbar laminectomy (lumbar vertebrae 1-3). Anesthesia was maintained by reinjection of half the initial dose of anesthetic when the animal became responsive to hind paw touch (~ every 90 minutes). The dura was kept intact unless stated otherwise. The surgical opening was surrounded with 2% agarose in PBS and the resulting reservoir was superfused with mouse artificial cerebrospinal fluid (maCSF). For two-photon imaging an FV1000 MPE microscope (Olympus) equipped with a femtosecond-pulsed Ti:Sapphire laser (Mai Tai HP, Newport/Spectra-Physics) and a high numerical aperture water immersion objective (x25/1.05 N.A.) was used. Small z-stacks (3 images with a z-distance of 0.8-1 µm) of the superficial dorsal spinal cord were acquired.

To determine the two-photon emission spectra of the Grx1-roGFP2 sensor *in vivo*, the sensor was first reduced with DTT (200 mM, diluted in maCSF). The two-photon laser excitation was tuned in 10 nm steps from 750 to 980 nm and images were recorded for each step. Then, the sensor was fully oxidized with H_2O_2 (50 mM, diluted in maCSF) and the measurements were repeated at each wavelength. By comparing the emission intensities of the oxidized and reduced sensor, the optimal wavelengths for ratiometric measurements was determined to be 800/940 nm.

For measuring the *in vivo* dose-response of the Grx1-roGFP2 sensor in the spinal cord, I first applied 200 mM DTT diluted in maCSF to the exposed spinal cord to reduce the sensor and then added increasing doses of H_2O_2 (0.5, 1, 2.5, 5, 10, 50, 100 mM H_2O_2 diluted in maCSF). These high doses of H_2O_2 were necessary to penetrate the dura and do not reflect the actual concentration at spinal axons. After 5 min of incubation time, image z-stacks (3 images with a z-distance of 0.8-1 µm) were acquired using excitation wavelengths at 800 nm and 940 nm as described above.

To record mitochondrial redox changes after axon injury, I performed laser axotomies (Yanik et al., 2004) in the spinal cord of living mice. For this purpose, the two-photon laser was tuned to 760-800 nm, the power increased to 100% (~2.9 W laser output) and focused on a small circle (diameter ~25 µm) for 90 sec. After laser exposure, a local

increase in fluorescence indicated the site of axon transection. To follow mitochondrial changes over time, I acquired image stacks at 800 and 940 nm every 5 min during the first hour and every 10 min for the rest of the experiment. The imaging field was ~500 µm x ~300 µm (x25/1.05 N.A., Olympus). To determine the effect of laser axotomies at a single mitochondrial resolution, the optical zoom was increased to ~5. Mitochondria at the lesion site, ~300-400 µm away from the lesion in transected axons and in non-transected axons were visualized.

In vivo confocal redox imaging of single mitochondria

To image mitochondrial shape and redox state with higher temporal resolution in the spinal cord or to perform laser axotomies in the triangularis sterni explant, I used an FV1000 MPE microscope (Olympus) equipped with a femtosecond pulsed Ti:Sapphire laser (Mai Tai HP, Newport/Spectra-Physics), as well as 405 and 488 nm laser lines for single-photon excitation and x40/0.8 N.A. (Nikon) or x25/1.1 N.A (Nikon) water immersion objectives. For imaging spinal axons, I exposed the spinal cord of *Thy1*-mito-Grx1-roGFP2 mice as described above. The dura was removed and axons in the superficial spinal cord were selected for imaging. It was necessary to remove the dura to improve the penetration of the 405 nm laser. Superficial axons were laser-transected using the protocol described above but with lower laser power (1.9 W laser output) and shorter laser exposure (5-10 sec) to minimize the lesion (diameter ~25 µm) and to allow higher time-resolution of mitochondrial changes. To rapidly alternate 405 and 488 nm excitation, sequential lines with 405 and 488 nm excitation laser were scanned (line scan duration: ~4.5 ms) and the emission light was collected (BP: 492-592 nm) in separate channels using a 50/50 beam-splitter. Small z-stacks (4-5 images with a z-distance of 1 to 1.5 µm) were acquired at a frame rate of ~0.2 Hz. For evaluation (see below), acquisition times were binned to 0.2 Hz as frame rates differed slightly between experiments. Laser axotomies in the triangularis sterni explant followed the same protocol. For pharmacological interventions, n-acetylcysteine (NAC, 1 mM, Sigma) was diluted in maCSF. Laser lesions in *Thy1*-mito-Grx1-roGFP2 x MnSOD and *Thy1*-mito-Grx1-roGFP2 x Cyp D knockout animals were performed in the same way. Transgene

negative littermates served as controls. To determine the role of extracellular calcium, 5 mM EGTA was added to maCSF and Ca^{2+} was replaced by Mg^{2+}. The pH was adjusted to pH 7.3.

In order to ascertain that the observed axotomy effects are not confounded by the KX anesthesia protocol, axotomy experiments were repeated using two different classes of general anesthesia. For this, standard isoflurane gas anesthesia (1-2% in O_2) and triple-combination injection anesthesia with fentanyl, midazolam and medetomidin were used (Mrsic-Flogel et al., 2007).

In vivo two-photon imaging of axonal calcium levels

To determine intra-axonal calcium changes after axotomy, transgenic mice that express the calcium-sensitive FRET (fluorescence resonance energy transfer) sensor, TN-XXL (Heim et al., 2007) under control of the *Thy1* promoter were used. Axotomies were induced as described above and imaging was performed on an FV1000 MPE microscope (Olympus) equipped with a femtosecond-pulsed Ti:Sapphire laser (Mai Tai HP, Newport/Spectra-Physics) and a high numerical aperture water immersion objective (x0.25/1.05 N.A., Olympus). The sensor was excited at 840 nm and the frame rate was ~0.2 Hz. Signals were recorded in two emission channels (dichroic mirror: 505 nm; band pass filters 460-500 nm for CFP and 520-560 nm for YFP).

Preparation of brain slices

Thy1-mito-Grx1-roGFP2 x *Thy1*-OFP animals were sacrificed with CO_2 at postnatal day (P)15 to P25 and decapitated. *Thy1*-OFP mice express the orange fluorescent protein cytoplasmtically. 300 µm thick sagital brain slices were prepared using a standard brain slicer. Brain slices were imaged on the FV-1000 confocal microscope (Olympus). 405, 488 and 559 nm laser lines were used to excite Grx1-roGFP2 and OFP. During imaging the brain slice was constantly superfused with carbogen gas-bubbled normal Ringer solution. Drugs to oxidize (10 mM diamide) and reduce (20 mM DTT) the sensor were washed into the bath and incubated for 5 min. OFP was used to delineate neuronal cell bodies and axons/dendrites.

In vivo cortical imaging

A thinned skull preparation was performed in *Thy1*-mito-Grx1-roGFP2 (Grutzendler et al., 2011). Animals were anesthetized with KX, and the skull was thinned with a motor-driven drill until the cortical surface with the superficial vessels was visible. The head was glued to a plastic dish and fixed in a custom-built holder. Confocal redox imaging and induction of a laser lesion was performed as described above. Instead of a point scan, a line scan was used for laser lesion induction.

Crush injury of the peripheral nerve

To confirm that mitochondrial shape and redox changes as seen after laser axotomy also occur in a traumatic model, a nerve crush injury was used. A crush lesion of the peripheral nerve was induced in triangularis sterni explants by manual pressure application to the intercostal nerve for 10 seconds using fine surgical forceps (Fine Science Tools). Imaging started immediately after the crush in the vicinity of the lesion site using the imaging parameters described above for Grx1-roGFP2 imaging on the wide-field system.

Amyotrophic lateral sclerosis

To investigate mitochondrial redox changes during chronic neurodegeneration, a commonly-used model of amyotrophic lateral sclerosis was used that is based on the over-expression of a mutated form of the human superoxide dismutase 1 protein (SOD^{G93A}; Gurney et al., 1994). SOD^{G93A} mice (Tg(SOD1*G93A)1Gur/J; Marinkovic et al., 2012) were obtained from The Jackson Laboratory (Bar Harbor). Triangularis sterni explants were prepared as described above from double heterozygous SOD^{G93A} mice x *Thy1*-mito-Grx1-roGFP2 at postnatal days 90 and 135. Unaffected SOD^{G93A}-negative littermates served as controls. The glutathione redox potential of single mitochondria was assessed by wide-field fluorescence microscopy as described above. To discern the length and frequency of mitochondrial contraction in the SOD model, affected animals of SOD^{G93A} mice x *Thy1*-mito-CFP crosses and littermates were imaged at P60, 90 and 120.

Experimental autoimmune encephalomyelitis

For EAE experiments, *Thy1*-mito-Grx1-roGFP2 mice were crossed to *Thy1*-OFP mice in order to assess mitochondrial redox levels in conjunction with the axonal stage. EAE was induced by immunizing animals (6 weeks to 6 months of age) with 250 µg of MOG peptide 35-55 mixed 1:1 with complete Freud`s adjuvant. 100 µl of the emulsion was injected into each flank of the animal and 50 µl at the base of the tail. 50 ng of pertussis toxin (PTx) was injected ip at the day of immunization and two days after immunization. Animals were scored daily according to the standard EAE scoring system and used for imaging experiments at the peak of the disease, two and three days after disease onset (EAE score at least 2). Scoring of EAE axons followed the criteria established previously in the lab (Nikić et al., 2011).

Image processing and analysis

Images were analyzed using the open-source software Fiji (http://fiji.sc). Single mitochondria or clusters of mitochondria and background regions were selected as regions of interest. Mean intensity values were measured in the 408 nm (or 405 nm and 800 nm in confocal or two-photon imaging, respectively) and 488 nm (940 nm) channel and background was subtracted. No background subtraction was performed in confocal *in vivo* imaging as this caused an artificial decrease of the baseline ratio. This is due to the different signal to background levels at 405 and 488 nm – the fluorescence signal at 405 nm is much closer to background. The two channels were divided (408/488, 405/488, 800/940) to indicate the sensor's state of oxidation. This ratio was normalized by dividing by the mean ratio measured after reduction with DTT (R/R_{DTT}) in cases where DTT was used in the same experiment. Otherwise the experimental results are shown either as R/R_0, with R_0 being the ratio at the time before the mitochondrial contraction or the axotomy, or normalized to a suitable control population (e.g. R/R_{Rest} for analysis of mitochondrial movement, $R/R_{Control}$ for SOD mice). All calculations were performed in Excel (Microsoft).

Mitochondrial shape is expressed as "shape factor" (length/width of the mitochondrion). The speed of spreading oxidation or mitochondrial shape changes after axotomy was

defined as the distance of a mitochondrion from the lesion over the time it took for the mitochondrion at this site to reach 50% of its maximal stable rise in probe oxidation or to reach 50% of its maximal shape change. The time period used for determining the stable plateau was judged individually for each mitochondrion. The distance of each mitochondrion to the lesion site was measured. The speed of oxidation and shape change was derived by averaging the values of all single mitochondria. To calculate the speed of the intra-axonal calcium spread, the time to reach 50% of the maximal signal was used at several points along one axon. Speeds were calculated for each of these measurements to obtain the average speed for an individual axon. To analyze the spread of calcium and oxidation in comparable axon populations, I first determined the distribution of axon diameters in *Thy1*-mito-Grx1-roGFP2 x *Thy1*-OFP mice and then included only axons within a similar population (mean ± 2 standard deviations of the population measured in *Thy1*-mito-Grx1-roGFP2 x *Thy1*-OFP mice) in the analysis of *Thy1*-TN-XXL mice.

For the generation of pseudo-color images, the 488 nm (940 nm) channel was manually “thresholded” and “binarized” to serve as a segmentation mask. This mask was used to segment both channels. The resulting images were divided (408/488 nm, 405/488 nm, 800/940 nm) and “normalized” to the DTT measurements (R/R_{DTT}) or the ratio before the event (contraction or lesion induction, R/R_0). The spectral pseudo-color look-up table “fire” (Fiji) was used to display images (Fig. 3).

For quantifying calcium levels, ROIs were placed along the transected axon and on non-lesioned axons ("outside") serving as controls. Both channels were background-subtracted and the YFP/CFP ratio was determined before and after the lesion (R/R_0). Pseudo-color representations were obtained as described above.

For representation of multi-color micrographs, different channels of confocal image series were overlayed in pseudo-color using the “screen” function in Photoshop (Adobe software). To stitch multiple images into larger montages, masking was used to obscure borders between individual images. Gamma was adjusted non-linearly to show low-intensity objects (except when quantitative results are represented), and a “despeckle” filter was used in some panels to suppress detector noise. For stitched figures, combined objects were isolated with the "magic wand" tool in Photoshop and placed on

a black background to remove distracting interference background patterns.

For quadrant representation of single mitochondria (SOD and axotomy data), the quadrant border delineating increased probe oxidation was defined as two times the standard deviation above the mean of the population with normal $R/R_{control}$. The quadrant border delineating altered mitochondrial shape was defined as two times the standard deviation above the mean of the oxidized mitochondria (at P135 in SOD^{G93} mice or in the lesion area after laser axotomy).

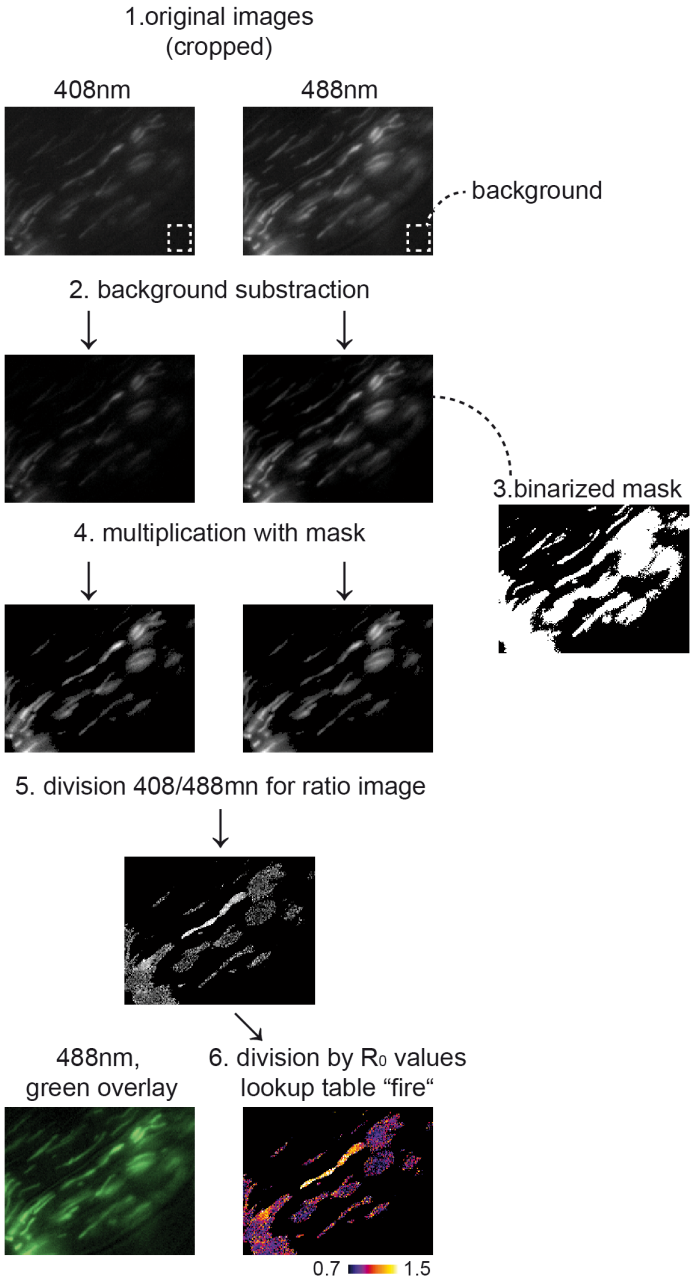

Figure 3: Representation of the workflow to create pseudo-color images

The figure describes the workflow that was used to create all pseudo-color representations of optical sensor dynamics. (**1**) Two channels were acquired at 408nm (405 nm in confocal and 800 nm in 2 photon) and 488 nm (940 nm for 2 photon). (**2,3,4**) Images were background-substracted and multiplied with the segmented binarized image. The creation of a segmentation mask is necessary to avoid artificial ratios in the image background where no mitochondria are present. Thus, the background is set to a pixel value of "0" by default. (**5)** Thresholded images were divided (408/488 nm). (**6**) The resulting image was divided by the avarge ratio before the contraction (R_0). Pseudo-color images (R/R_0) can be directly compared to image quantifications, which are usually shown next to the image series. All image manipulations were performed in FIJI. Adobe Photoshop and Illustrator were used for illustrations.

Buffers and solutions

4% Paraformaldehyde (PFA)	
Chemical	Quantity (1l total volume)
PFA	40 g
dH_2O	800 ml
10x PBS	100 ml
NaOH (2N)	125 µl

Store at -20 °C. Avoid freeze-thaw cylces.

10x Phosphate buffered saline (PBS)		
Chemical	Quantity (1l total volume)	Final concentration (mM)
NaH_2PO_4	2.56 g	18.6
Na_2HPO_4	11.94 g	84.1
NaCl	102.2 g	1750

Store at room temperature.

10x normal Ringer		
Chemical	Quantity (for 1l total volume)	Final concentration (mM)
$NaHCO_3$	21.84 g	260
NaH_2PO_4* H_2O	1.72 g	12.5
KCL	1.86 g	25
NaCl	73.05 g	1.2

Dissolved in dH_2O. 1 l total volume.

1x normal Ringer		
Chemical	Quantity (1l total volume)	Final concentration (mM)
$CaCl_2$, 1M	2 ml	2
$MgCl_2$, 1M	1 ml	1
Ringer solution (10x)	100 ml	
dH_2O	900 ml	
Glucose	3.6 g	20

Ketamin / Xylazine (KX)	
Chemical	Quantity for 20 ml total volume
Ketamine	300 mg
Xylazine	20 mg
Dissolved in dH_2O	20 ml total volume
Store at room temperature.	

A Mouse artificial cerebrospinal fluid (maCSF)	
Chemical	Quantity (500 l total volume)
$CaCl_2$* $2H_2O$	0.206 g
$MgCl_2$* $6H_2O$	0.163 g
NaCl	8.66 g
KCl	0.224 g
Dissolved in dH_2O	500 ml total volume

B Mouse artificial cerebrospinal fluid (maCSF)	
Chemical	Quantity (500 l total volume)
$Na_2 HPO_4$* $7H_2O$	0.214 g
NaH_2PO_4* H_2O	0.0273 g

Dissolved in dH_2O 500 ml total volume

Combine A and B, store at room temperature.

The protocol for maCSF can be found on the website of Alzet (Cupertino, USA) http://www.alzet.com/

Statistical analysis

Statistical testing was performed using PRISM (GraphPad). Statistical significance was tested using two-tailed t-tests for datasets including more than 12 values. For smaller data sets the Mann-Whitney test was applied. For multiple comparisons ANOVA with Bonferroni *post hoc* testing was used. P-values < 0.05 were considered to be significant and indicated by *; P-values < 0.01 were indicated by ** and < 0.001 by ***. Graphs show mean ± S.E.M. Trend-lines for dose response graphs were calculated with PRISM, assuming a dose-response saturation kinetic.

Results

In vitro comparison of different redox sensors

To compare the redox-sensitive proteins HyPer (Belousov et al., 2006) and Grx1-roGFP2 (Gutscher et al., 2008) concerning their reactivity towards H_2O_2 both constructs were expressed in HEK-293 cells under the *CMV* promotor and targeted to the cytosol or to mitochondria. Measurements were performed two to three days after transfection when bright fluorescence was detectable in more than ~30% of cells. The redox level under baseline conditions measured in cell culture medium without additives was almost completely reduced in accordance with previous reports (Dooley et al., 2004; Gutscher et al., 2008; Hanson et al., 2004). Both sensors could be oxidized by adding H_2O_2 to the perfusate (100 µM). Oxidation resulted in a strong decrease (Grx1-roGFP2, Fig. 4 a,b) or increase in fluorescence (HyPer, Fig. 4 c,d) when excited at 488nm. The dynamic range of Grx1-roGFP2 and HyPer was at least two-fold. Dual wavelength excitation was not performed in cell culture experiments. After oxidation and removal of the oxidant a spontaneous reduction of the Grx1-roGFP2 sensors occurred, due to the cellular recovery from the exogenously applied oxidative stress. The recovery was not measurable with HyPer indicating that the sensor might not be suitable to detect fast dynamic redox signals. Therefore (and because of the known pH-sensitivity of HyPer; Belousov et al., 2006; Roma et al., 2012) we decided to use Grx1-roGFP2 to generate a transgenic mouse line expressing mito-Grx1-roGFP2 under the *Thy1* promotor.

The *CMV*-roGFP2-Orp1 construct was tested in the same way. It showed a similar dose response when expressed in HEK cells and could be reversibly oxidized and reduced.

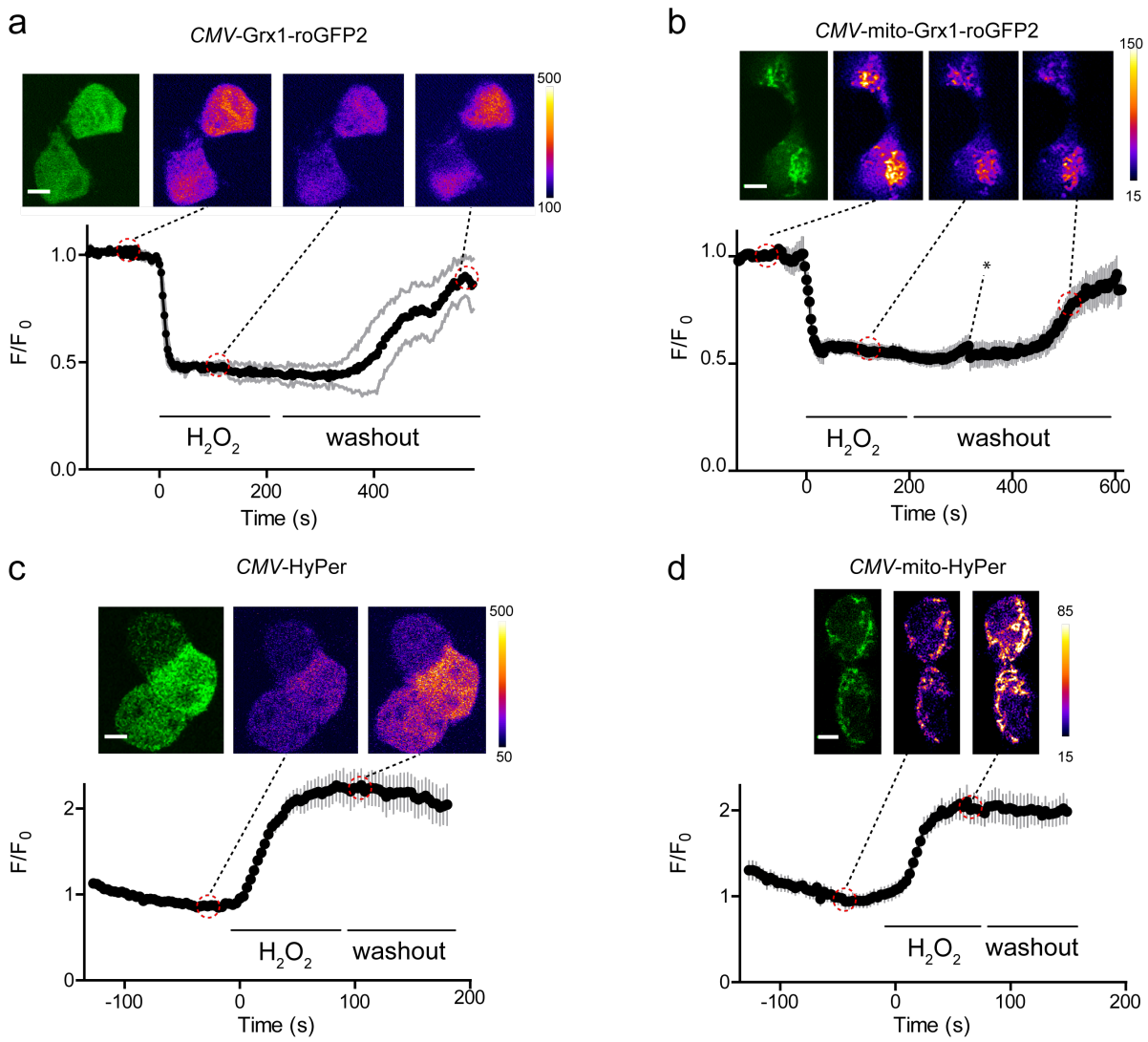

Figure 4: *In vitro* comparison of genetically-encoded redox sensors

HEK-293 cells were transfected 2-3 days prior to confocal measurements with the indicated construct. Panels show a 488nm image pseudo-colored in green on left and pseudo-color images with lookup table “fire” on right (representing the 488nm channel only) before and after oxidation with 100 µM H_2O_2. (**a**) *CMV*-Grx1-roGFP2 (**b**) *CMV*-mito-Grx1-roGFP2, (**c**) *CMV*-HyPer and (**d**) *CMV*-mito-HyPer. Quantifications below show mean ± SEM of 5-9 cells per condition of a representative experiment except of (**a**) where only 2 cells were quantified and both traces are shown in grey. Black trace represents the mean. Asterix (*) in (b) indicates out of focus frames. For a full estimation of the dose-response, dual-wavelength excitation at 405mn and 488nm would have been necessary, which I chose not to do, as the dynamic range in this setting has been reported previously (Belousov et al., 2006; Gutscher et al., 2008). Representative images of single optical sections are shown. Imaging rate is ~0.3 Hz. Scale bar is 5 µm for all micrographs. Calibration bar represents the fluorescence intensity in the 488 nm channel.

Generation of *Thy1*-mito-Grx1-roGFP2 mice

To generate *Thy1*-mito-Grx1-roGFP2 mice ("mito-Grx mice") blunt-end cloning of the mito-Grx1-roGFP2 plasmid into the *Thy1* backbone was performed. We decided to target the fluorescent protein (XFP) to mitochondria because we were especially interested in the mitochondrial contribution to cellular redox stress. After several unsuccessful attempts to PCR amplify the mito-Grx1-roGFP2 construct and to generate sticky-end cloning sites for further cloning into the *Thy1* backbone, the blunt end cloning strategy turned out to be successful (Fig. 5). The *Thy1* vector and the mito-Grx1-roGFP2 construct were bluntly cut and ligated using standard molecular biological techniques. After re-testing the construct and its functional responsiveness towards H_2O_2 in HEK cell culture, the construct was isolated from *E. coli* and purified on a polyacrylamide gel that was run without ethidium bromide to prevent the mutagenizing effects of the intercalating dye. The quality and concentration of the linearized DNA was determined photometrically. The concentration of the linearized DNA that was used for pronuclear injections was 215 ng/µl. The generation of the transgenic line was performed at the transgene facility of the Max Planck Institute for Molecular Cell Biology and Genetics, Dresden by standard pronuclear injections into pseudo-pregnant host mice. The *Thy1*-mito-roGFP2-Orp1 line was generated with the same approach. *I thank Anja Schmalz (Kerschensteiner lab) for cloning the Thy1-roGFP2-Orp1 construct.*

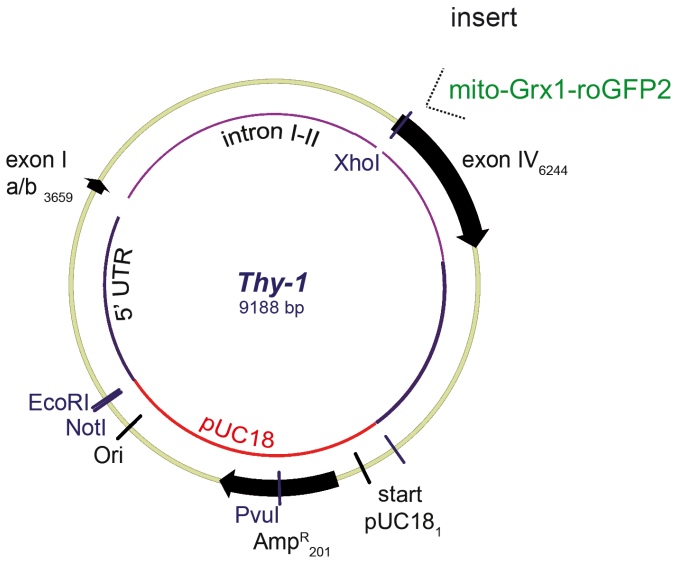

Figure 5: Cloning strategy for *Thy1*-mito-Grx1-roGFP2 mice

Blunt end cloning of the mito-Grx1-roGFP2 construct into the *Thy1* vector was performed. This scheme shows the insertion site of mito-Grx1-roGFP2 into the *Thy1* vector. Image modified from Marinković *et al*, 2011, CSHL Press.

Morphological characterization of transgenic lines

I thank Franz Pfister, MD (Kerschensteiner lab) for help with the morphological screening and with baseline redox measurements in Thy1-mito-Grx1-roGFP2 triangularis sterni explants.

We obtained 11 PCR-positive *Thy1*-mito-Grx1-roGFP2 founder lines from the Max Planck facility that were screened for their expression pattern. Three lines (mito-Grx 676, 690 and 920) turned out to be particularly useful as they showed strong expression in the CNS and PNS. All of these lines are "full" lines with ~90% labeling density within labeled neuron populations (*e.g.* ~90% of all motor neurons in the spinal cord are labeled; Fig. 6 a-d). For complete screening, XFP expression in the cortex, hippocampus, cerebellum, retina, spinal cord and peripheral nerve was assessed (Table 1). The generation of *Thy1*-mito-roGFP2-Orp1 resulted also in 11 founder lines. Orp1 is an enzyme from yeast that acts as a direct H_2O_2 sensor and is able to transfer electrons from H_2O_2 to the thiol groups of roGFP (Gutscher et al., 2009). Unfortunately, the Orp lines were all very dim so that even with high laser intensities the signal especially at 408 nm remains only slightly above background. The line *Thy1*-mito-roGFP2-Orp1-177 is the brightest line and a spinal cord section with single mitochondrial labeling is shown in Fig. 6 e,f. For this reason, the *Thy1*-mito-roGFP2-Orp1 mice were not pursued in depth.

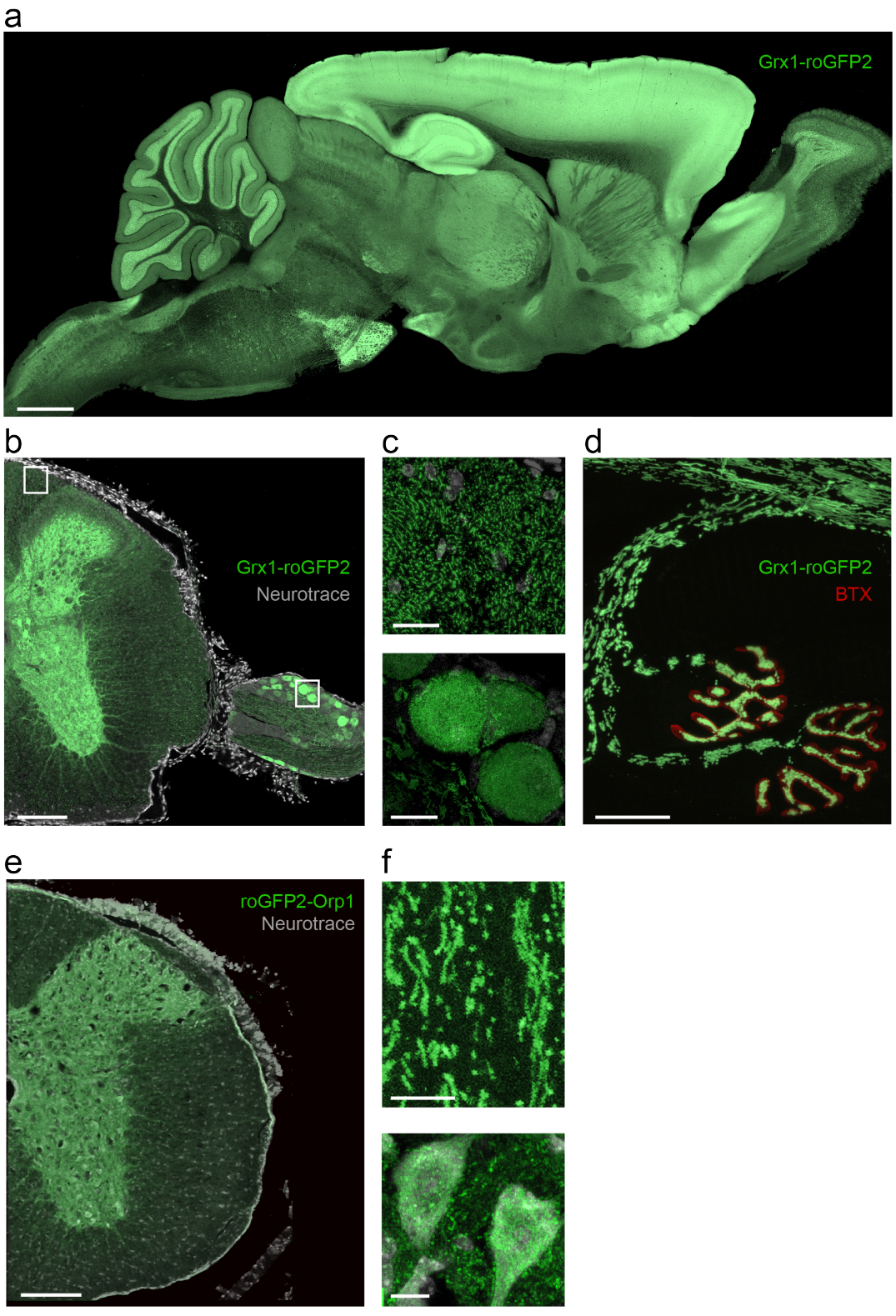
a
Grx1-roGFP2
b
Grx1-roGFP2
Neurotrace
c
d
Grx1-roGFP2
BTX
e
roGFP2-Orp1
Neurotrace
f

Figure 6: Morphological characterization of *Thy1*-mito-Grx1-roGFP2 and *Thy1*-mito-roGFP2-Orp1 mice

Eleven founder lines were generated for each construct and screened for expression of the sensor protein in the CNS and PNS. (**a**-**d**) *Thy1*-mito-Grx1-roGFP2 mice show high XFP expression in the central and peripheral nervous system. (**b**) Left image shows a horizontal hemi-section of the spinal cord. (**c**) Magnifications of the boxed areas: the dorsal funiculus (top) and cell bodies in the dorsal root ganglion (bottom). (**d**) Two neuromuscular junctions with the post-synaptic sites labeled in red. (**e-f**) The expression of the mito-roGFP2-Orp1 sensor is much weaker. The image in (**e**) shows a horizontal section of the spinal cord of a *Thy1*-mito-roGFP2-Orp1 mouse. (**f**) illustrates the labeling of single mitochondria in the dorsal funiculus, showing normal mitochondrial morphology (upper image) and neuronal cell bodies in the ventral horn (lower image). Scale bars are 1mm in (**a**), 200µm in (**b** and **e**), 20µm in (**c** and **d** insets) 5µm in (**f**, upper image) and 10µm in (**f**, lower image).

Line	Spinal cord		Retina			Cortex	Cerebellum			Hippocampus				Expres-sion level
	MN	DRG	RG	AC	BC		GC	MF	PC	DG	CA1	CA2	CA3	
920	+	+ > 50%	sub	+	sub	+ full	-	-	+	+	+	+	+	Bright
676	+	+ > 75%	+	-	-	+ full	+	-	-	-	-	-	-	Bright
690	+	+ > 40%	+	+	-	+ sub	+	-	-	+	+	-	+	Very bright

Table 1: Characterization of the expression pattern of *Thy1*-mito-Grx1roGFP lines

Comparison of the expression pattern of three mito-Grx lines (920, 676 and 690). These lines were selected for further experiments. Most experiments were performed in the 920 line.
Table legend: +: expression in most cells; sub=subset: expression in < 80% of cells, AC: amacrine cells; BC: bipolar cells; CA: cornu ammonis; DG: dentate gyrus; DRG: dorsal root ganglion; GC: granule cells; L: cortical layer; MF: mossy fibers; MN: motor neurons; PC: Purkinje cells; RG: retinal ganglion cells

Anatomical and behavioral analysis of mito-Grx mice

In order to assess the health of the novel transgenic lines, mito-Grx animals were screened for neurological and behavioral deficits. Transgene-negative littermates or mito-CFP animals served as controls. No significant differences were found in all parameters tested ($p>0.05$ for all tests, Fig. 7). This included morphological (mitochondrial shape factor, mitochondrial density in axons, mitochondrial transport, muscle diameter, mitochondrial density in neuromuscular junctions, size of the NMJ), as well as physiological parameters (body weight, open field locomotor test and ladder rung test). Morphological and functional measurements (mitochondrial transport) were performed in the triangularis sterni explant. Behavioral testing was aimed to assess gross motor function (BBB), as well fine motor skills and corticospinal tract function (ladder rung test; Basso et al., 1995; Scheff et al., 2002). The different tests aimed at assessing parameters of neuronal health, with a focus on the motor system, as my analysis focused on motor axons and the sensor is highly expressed in these neurons.

Physiological concentrations of ROS can be measured

The functional responsiveness of Grx1-roGFP2 and roGFP2-Orp1 was confirmed in triangularis sterni explants of transgenic animals (Kerschensteiner et al., 2008). Explants were kept between 32°C and 35°C and continuously superfused with carbogen-bubbled normal Ringer's solution. After reduction of the preparation with 500µM DTT, increasing concentrations of H_2O_2 (6.25, 12.5, 25, 50, 100, 200, 400, 800, 1000 µM) were added to the perfusion bath. Incubation time was 5 min. The mitochondrial redox potential was measured at the NMJ by dual wavelength excitation with 408 and 488nm using a polychromator-equipped wide-field setup (Olympus BX-51). Superficial NMJs were chosen for redox measurements in order to facilitate the diffusion of the chemical to the NMJ. The dynamic range of mito-Grx1-roGFP2 (Fig. 8 a,b) and of mito-roGFP2-Orp1 was 2.6 (Fig. 8 c,d) and both sensors could be reversibly oxidized and reduced. As the *Thy1*-mito-roGFP2-Orp1-177 line is quite dim further experiments were performed only with the mito-Grx lines.

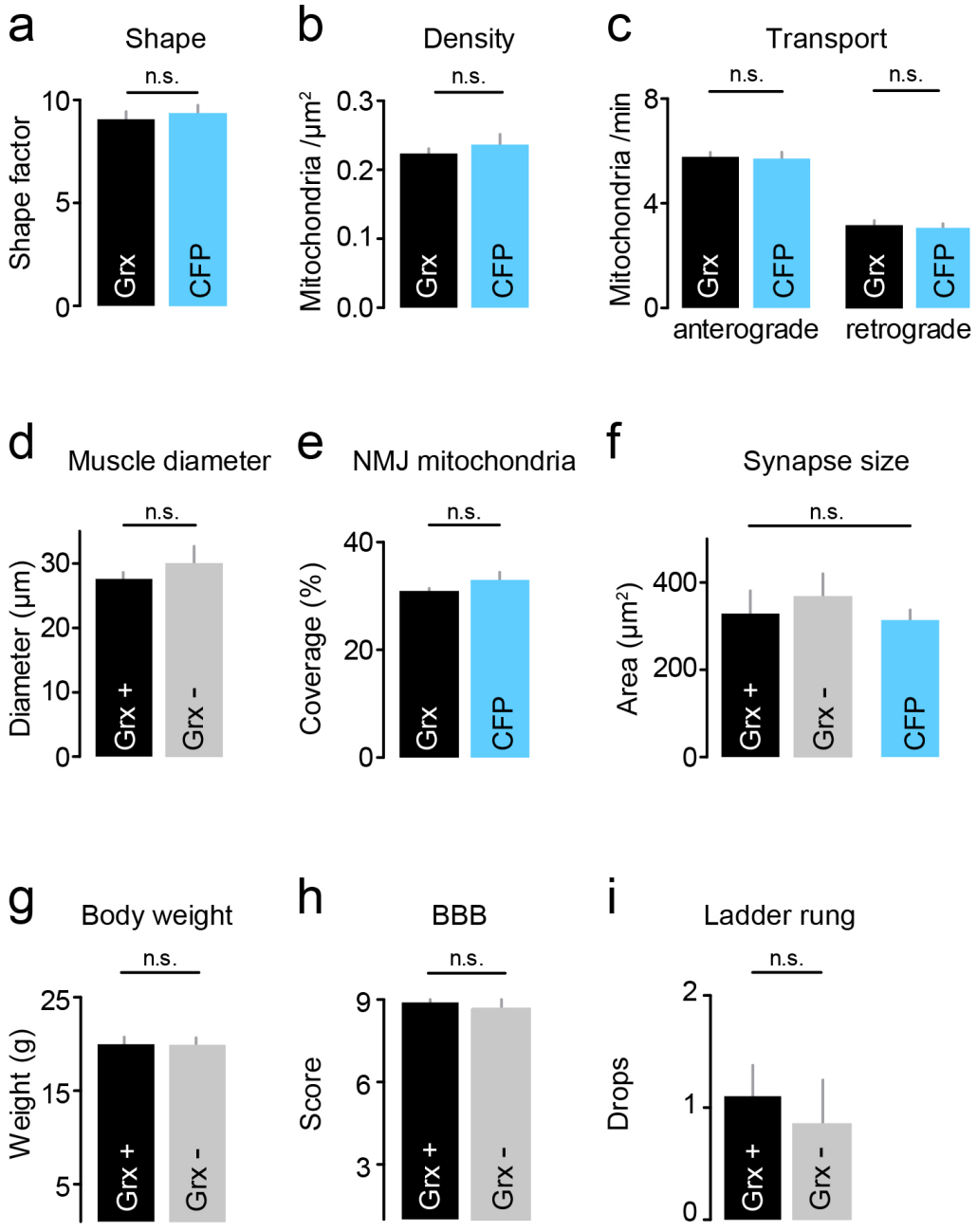

Figure 7: No neurological abnormalities are seen in *Thy1*-mito-Grx1-roGFP2 mice

(**a-c**) Quantification of mitochondrial shape factor, density and transport in intercostal nerve axons of *Thy1*-mito-Grx1-roGFP2. *Thy1*-mito-CFP mice served as controls. (**d**) Assessment of the diameter of alexa 635-conjugated phalloidin-stained muscle fibers. (**e,f**) Comparison of mitochondrial density (**e**) and size (**f**) of Alexa 594-conjugated bungarotoxin-stained NMJs. (n ≥ 3 mice per group for **a**-**f**). (**g**) Body weight of 6-8 week old *Thy1*-mito-Grx1-roGFP2 and non-transgenic littermates. (**h,i**) Assessment of motor function of 6-8 week old *Thy1*-mito-Grx1-roGFP2 and non-transgenic littermates. (n ≥ 6 animals per group for **g-i**). I acknowledge help with data acquisition and analysis (for panel a-f) by Petar Marinković, PhD (Misgeld lab).

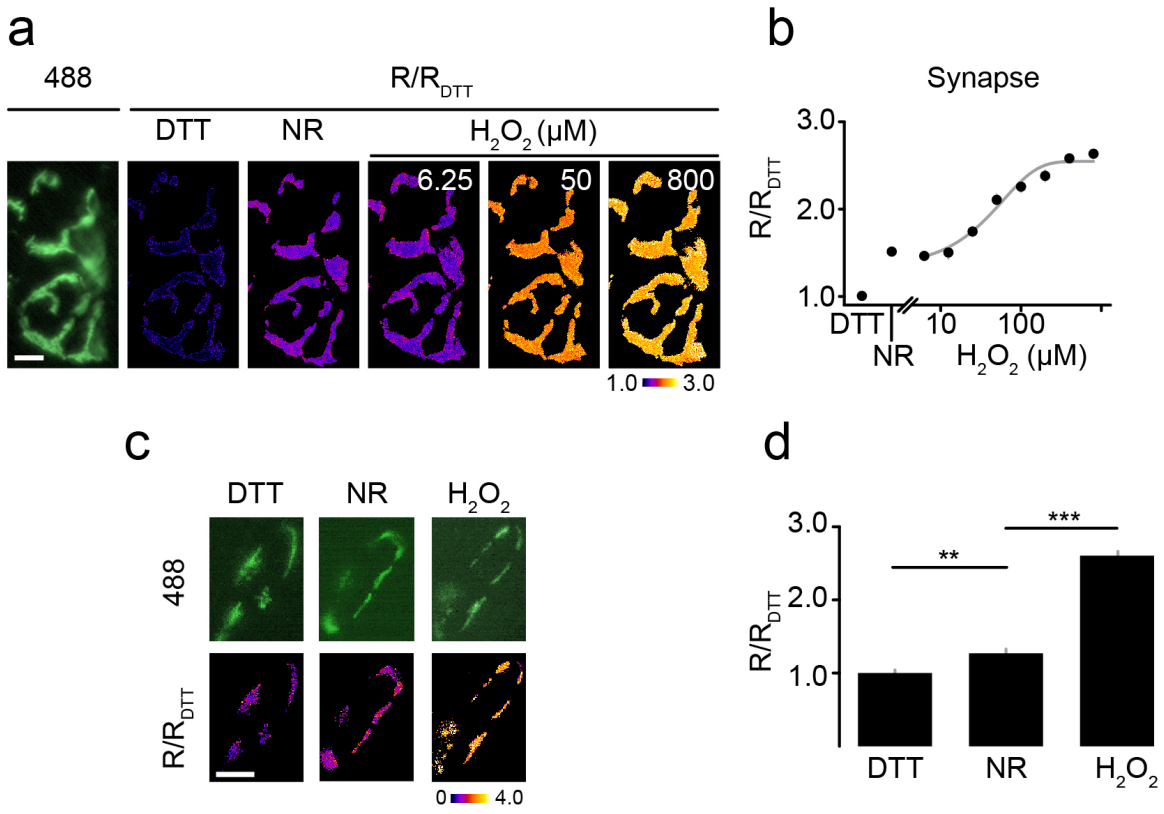

Figure 8: *In situ* dose-response experiments allow the quantification of the mitochondrial glutathione redox potential and mitochondrial H_2O_2 levels

(a) 488 nm wide-field image (left) and pseudo-colored images (R/R_{DTT}; right) of the same NMJ during the addition of 500 µM of the reducing agent DTT, normal Ringer's solution (NR) or the oxidant H_2O_2 (6.25, 50, 800 µM). Pseudo-coloring indicates the normalized fluorescence ratio (R/R_{DTT}). (**b**) Full dose-response in triangularis sterni explants from *Thy1*-mito-roGFP2 measured at NMJs shows a dynamic range of 2.6 (n ≥ 14 synapses, 3-4 mice; note that at several concentrations error bars are smaller than data symbols). (**c**) 488 nm wide-field image (upper row) and pseudo-colored images (lower row) during the addition of 500 µM DTT, NR or 1mM H_2O_2. (**d**) shows the dose-response quantification in *Thy1*-mito-roGFP2-Orp1 explants (n > 10 synapses, 3 mice). Scale bar in (**a**) and (**c**) = 5µm.

The glutathione potential is tightly regulated

In triangularis sterni explants, measurements of the glutathione redox potential of single mitochondria can be performed easily in the intercostal nerve axons. In contrast to the neuromuscular junction, where mitochondria reside very close to neighboring mitochondria and cannot be resolved as single entities, axonal mitochondria lay

seperated in the axon. Redox levels of resting and moving mitochondria in the axon showed no difference. Also, mitochondria that were anterogradely or retrogradely transported had indistinguishable redox states (Fig.9 a,b). The redox state did not depend on the size of the mitochondrion. There was only a weak correlation between mitochondrial shape factor and redox state (r^2: 0.14, 223 mitochondria, 3 mice).

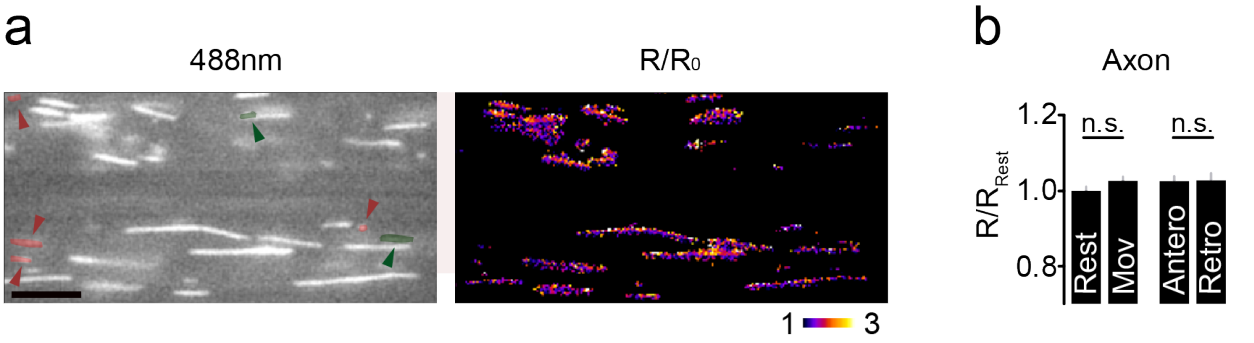

Figure 9: The glutathione potential is tightly regulated and independent of organelle location or movement

Illustration of mitochondrial redox levels in the intercostal nerve measured in triangularis sterni explants from *Thy1*-Grx1-roGFP2 mice. Panel shows two parallel-running axons in the proximal intercostal nerve (**a**). The redox level is almost completely reduced and homogenous within the mitochondrial population. There is no difference between resting ("Rest") and moving ("Mov") mitochondria. Also mitochondria that are anterogradely ("Antero", red overlay in 488 nm image) or retrogradely ("Retro" green overlay) transported show no difference in their redox potential. Quantification of redox levels in (**b**) shows different populations of axonal mitochondria (normalized to resting mitochondria; n ≥ 88 mitochondria, 3 mice). Scale bar = 5µm.

Mitochondria show spontaneous contractions

Even though the redox potential is tightly regulated overall, a small fraction of mitochondria (0.6 ± 0.1 per hour in proximal axons, n=594 mitochondria, 14 recordings, 3 mice) exhibited short-lasting "oxidative bursts" which were accompanied by a reversible shortening of the organelle. We dubbed these fast cycles of shortening and elongation of single mitochondria "mitochondrial contractions". Contractions can be visualized in sensory and motor axons (saphenous and intercostal nerve) and were observed *in vivo* (dorsal funiculus of the spinal cord) and in various types of explants

(tibialis nerve, triangularis sterni). They are also observed in the NMJ and occur more frequently at distal nerve sites.

Mitochondria that reside in the immediate vicinity of a contracting one are not apparently affected by the contraction, showing that it is a highly local, and perhaps organelle-autonomous event. Smaller mitochondria become rounded before they re-elongate (Fig. 10). while longer mitochondria have a “pearl-on-string” appearance during the contraction (Fig. 11 a). Single mitochondria can also show multiple rounds of contractions and elongations during a short period of time (Fig. 10).

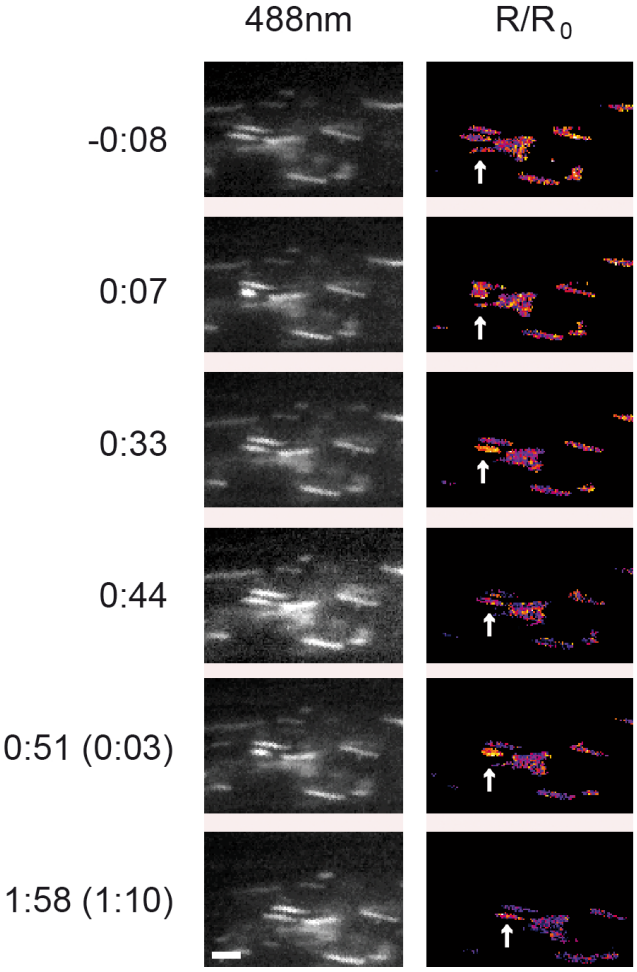

Figure 10: Mitochondria undergo spontaneous contractions without obvious effect on neighboring mito-chondria

Time-lapse series shows an example of a repetitively contracting mitochondrion (white arrow). During the contraction the mitochondrion rounds up and re-elongates. Note that the mitochondrion contracts twice after having gone back to the relaxed state. During the contraction the glutathione pools reversibly oxidizes. Time point 0:00 indicates the onset of the contraction. Time (min:sec). Only a small percentage of mitochondria (<1%) contracts multiply times during the usual imaging time of 5 min per movie. Scale bar 2 µm.

Contractions are linked to an oxidative burst

During contractions, the Grx1-roGFP sensor reversibly oxidizes (Fig. 11 b). ~25% of the glutathione pool oxidizes during the contraction, under the estimation that the addition of

800 µM H_2O_2 (see Fig. 8b) leads to the oxidation of the entire glutathione pool. The onset of the redox signal is markedly slower than the morphological shortening ($\tau_{rise\ (50\%)}$: 50 sec compared to 1 sec for the morphological change). The oxidation lasts for ~180 sec until it returns to baseline values ($\tau_{decay\ (1/e)}$: ~125 sec). The oxidative shift was always associated with a contraction. Non-contracting mitochondria showed no fluctuations in their redox potential. Given the "delayed" oxidation compared to the shape change, the goal of the following experiments was to further characterize the ionic fluxes that occur during such contractions as well as to better understand the initiation and function of contractions.

The membrane potential drops reversibly during the contraction

To probe additional parameters of mitochondrial function, I established three color imaging of the mitochondrial inner membrane potential (Ψ) using the potential-sensitive dye tetramethylrhodamin-methylester (TMRM) in conjunction with mito-Grx1-roGFP2 imaging in triangularis sterni explants. The dye needs to be loaded with a foam pad at least one day in advance, as it is not efficiently taken up into intercostal nerve axons upon bath application (see materials and methods). Excitation was performed at 408/488/550nm on the polychromator setup. During contractions, visualized in the proximal intercostal nerve, the mitochondrial inner membrane potential drops instantly, simultaneously with the shape change, whereas the glutathione oxidation is relatively delayed (Fig.11 c,d). The matrix potential remains lowered for ~200 sec and only recovers slowly. TMRM measurements were performed in the proximal intercostal nerve where the nerve is not in proximity to muscle fibers because TMRM also stains muscle mitochondria and adheres unspecifically to lipophilic tissues.

The contraction is accompanied by a spike of the matrix pH

To further dissect the molecular events occurring during mitochondrial contractions, AAV-1/2 injections into the cervical spinal cord of C57B/6 wildtype animals were performed to express additional molecular sensors in intercostal nerve (ICN) axons (for details regarding the injection procedure, see materials and methods). The injections were targeted to α-motorneurons in the ventral horn of the spinal cord that give rise to intercostal nerve axon bundles. AAV-mito-SypHer was used to measure the

mitochondrial matrix pH (Poburko et al., 2011; Santo-Domingo et al., 2013). pH measurements together with TMRM recordings also allow an estimatation of the proton motive force (PMF: Ψ + ΔpH). Virally delivered mito-SypHer was expressed strongly in spinal motorneurons and single mitochondria could be discerned in the intercostal nerve and at the NMJ ~2 weeks after injection. Single mitochondria that contracted showed a short peak in the matrix pH (~5 sec) that was followed by a long-lasting acidification of the mitochondrial matrix without an obvious recovery during the observation time of 5 minutes (Fig.11 e,f).

Matrix calcium levels do not increase during the contraction

What could cause the drop of the matrix potential and the short alkaline spike? An obvious candidate would be a cation influx, *e.g.* of calcium ions. This would lead to a drop of the matrix potential. Also, calcium is known to promote the speed of the matrix dehydrogenases that supply the electron transport chain with reductive educts and thus to amplify the reaction speed of the electron transport chain (Scheffler, 2011).

I used the same viral strategy as for the SypHer delivery to measure matrix calcium levels during contractions. AAV-mito-GCaMP-3 and AAV-mito-RGECO-1 both targeted to the mitochondrial matrix were used (Akerboom et al., 2012; Tian et al., 2009; Zhao et al., 2011). GCaMP-3 showed a 35% increase from baseline fluorescence during the contraction but also proved to be highly pH sensitive. When the Ringer's solution was alkalized to a pH of 8.5, GCaMP-3 showed a 230% signal increase, thus indicating that the GCaMP signal is most likely “contaminated” by the observed pH change. Newer generation of genetically-encoded calcium indicators, including RGECO-1, have been shown to be less pH sensitive than GCaMP-3 (Akerboom et al., 2012). When mitochondrial contractions were visualized in explants from wildtype animals injected with AAV-mito-RGECO-1, the matrix calcium level remained almost unchanged during contractions (Fig.11 g,h). The small signal bump at the beginning of the contraction represents only ~1% of the dynamic range of the sensor (compared to the signal seen after axotomy, see below) and is most likely due to the shape change of the organelle. Therefore, calcium is most likely not the driving cation that leads to matrix depolarization during contractions.

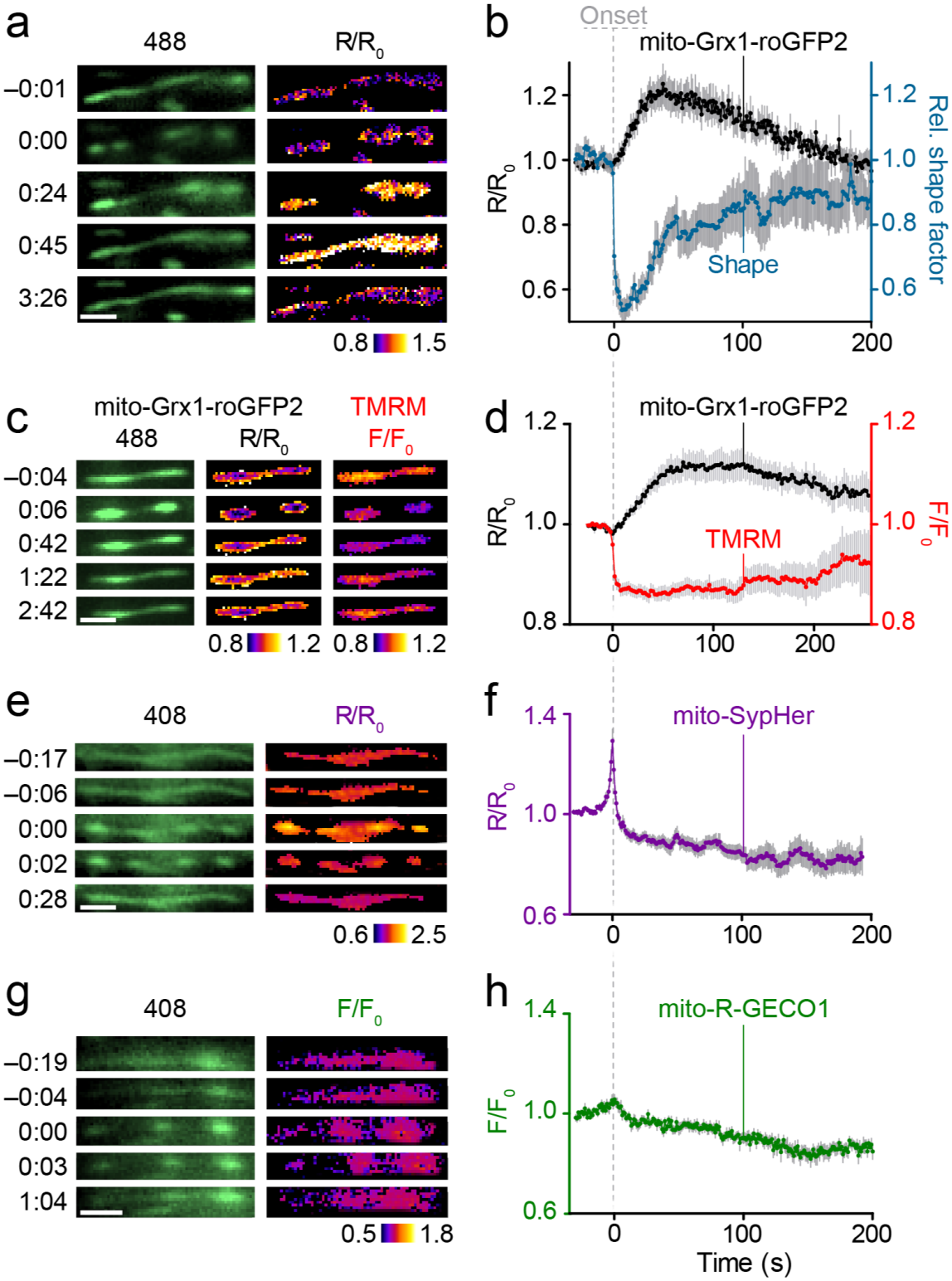
a
488
R/R0
–0:01
0:00
0:24
0:45
3:26
0.8
1.5
b
Onset
mito-Grx1-roGFP2
R/R0
Rel. shape factor
Shape
1.2
1.0
0.8
0.6
0
100
200
c
mito-Grx1-roGFP2
488
R/R0
TMRM
F/F0
–0:04
0:06
0:42
1:22
2:42
0.8
1.2
d
mito-Grx1-roGFP2
TMRM
e
408
R/R0
–0:17
–0:06
0:00
0:02
0:28
0.6
2.5
f
mito-SypHer
1.4
g
408
F/F0
–0:19
–0:04
0:00
0:03
1:04
0.5
1.8
h
mito-R-GECO1
Time (s)

Figure 11: Mitochondria undergo spontaneous contractions

(**a**) Example of a contracting mitochondrion in an intercostal axon of a triangularis sterni explant from a *Thy1*-Grx1-mito-roGFP2 mouse. Note the pearl-on-string morphology of longer mitochondria during the contraction (in contrast, smaller mitochondria just round up; *cf.* Fig, 10). (**b**) Quantification of the glutathione redox potential, which shows reversibly oxidation of the glutathione pool during the contraction. The oxidation is preceded by a sudden decrease of the mitochondrial shape factor, which normalizes within ~180 sec (n = 9 contractions, 5 mice). (**c**) Example of a contracting mitochondrion loaded with the membrane potential-sensitive dye TMRM, which allowed determining potential as well as glutathione redox potential. (**d**) Quantification of the mitochondrial membrane potential and the glutathione redox potential during contractions (n = 15 contractions, 3 mice). (**e**) Example of a contracting mitochondrion in a wild-type mouse injected with AAV-mito-SypHer. (**f**) Quantification of the mitochondrial matrix pH during contractions (n = 23 contractions, 6 mice). (**g**) Example of a contracting mitochondrion labeled with AAV-mito-RGECO-1. (**h**) Quantification of the mitochondrial matrix calcium during contractions (n = 23 contractions, 3 mice).

To rule out experimental artefacts affecting contraction characteristics *e.g.* due to viral labelling or the imaging conditions, a number of control experiments were performed. These are described in the following paragraphs.

Viral labelling of motor neurons does not cause major toxicity

AAV injections yielded broad and stable expression in ventral horn neurons of the spinal cord including in α-motor neurons. Importantly, there was only minimal toxicity associated with AAV-mediated manipulations. Fig. 12 a shows a representative horizontal section of a cervical spinal cord of a C57BL/6 wildtype mouse injected with AAV-mito-SypHer. There was also good labelling in intercostal nerve axons and at the NMJ (Fig. 12 b,c). Overall, the sensors described above showed minimal toxicity and the intercostal nerve looked overall healthy. In a few animals there was some toxicity detectable in the peripheral nerve with end bulbs of dying-back axons. These were axons with very high expression levels of the XFP. Damaged axons were excluded from the analysis. Toxicity seemed to depend not only on the expression level, but also on the injected construct. An AAV-mito-roGFP-Orp1 construct caused widespread toxicity, again arguing against the usefulness of this sensor in the nervous system of mice.

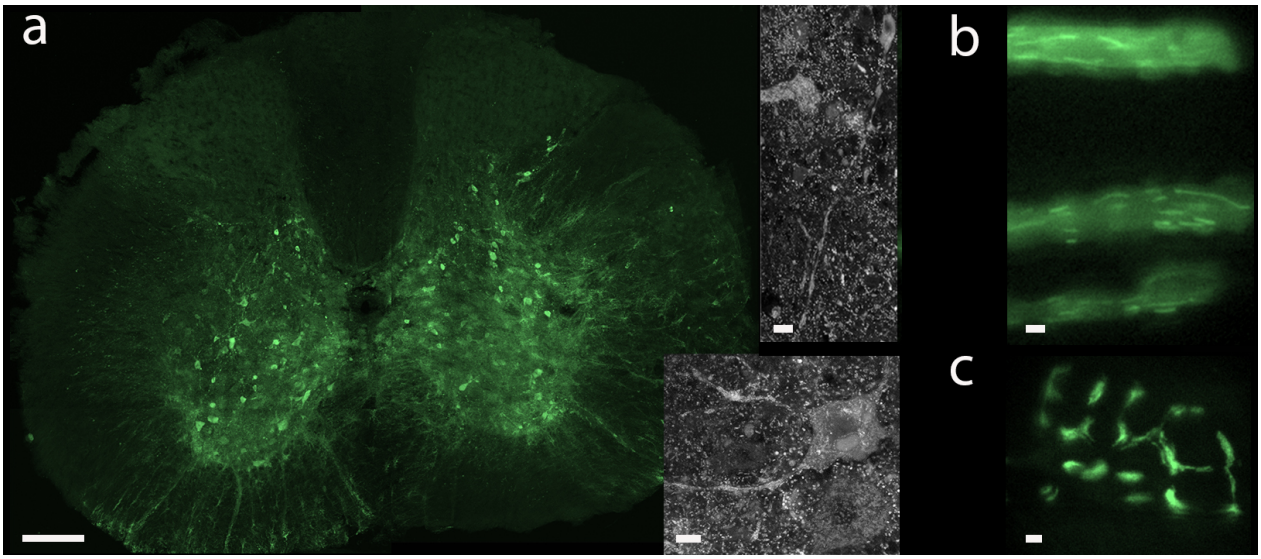

Figure 12: Cervical spinal cord, peripheral nerve and NMJ of a wildtype mouse injected with AAV-mito-SypHer

(a) Representative image of a horizontal spinal cord section of a wildtype mouse, which was bilaterally injected with AAV-mito-SypHer two weeks prior. Magnified images show motorneurons in the ventral horn with long projections that give rise to intercostal axons. **(b)** Three axons in the intercostal nerve with virally labelled mitochondria. Note that there is also fluorescent protein in the cytoplasm of the axons **(c)** Image of a virally labeled NMJ. Scale bar in is 200 µm in **(a)**, 10 µm in close ups and 2 µm in **(b)** and **(c)**.

Contractions are not an artifact of phototoxicity

One concern is that phototoxicity is contributing to mitochondrial contractions, especially as I observed that the frequency of contractions seemed increased under particularly bright illumination conditions. To delineate the role of phototoxicity, a number of control experiments were performed. First, a “light dose” experiment showed that also under very low light levels (illumination 488nm: 4ms and 408nm: 16ms) contractions still occurred with similar frequencies than with the standard “light dose” used in most other experiments (488nm: 30ms, 408nm: 150ms, Fig. 13a). Contractions were detectable independently of the fluorophore in mito-CFP, mito-Grx, mito-taqRFP-t and virally transduced animals (Fig. 13b). Additionally, when animals were directly sacrificed without prior imaging, morphological figures of “pearl-on-string” mitochondria that are indicative of contracted mitochondria could be discerned in the intercostal nerve (Fig. 13 c). Altogether mitochondrial contractions were visualized with a number of different

microscopes (wide-field, confocal single photon, 2-photon, spinning disc confocal) both *in vivo* and *ex vivo* in motor (triangularis explant) and sensory axons (in the dorsal funiculus and in the saphenous nerve). This largely rules out that mitochondrial contractions are a pure imaging artifact and suggests that phototoxicity had only a minor, if any effect on the quantitative analysis of contractions.

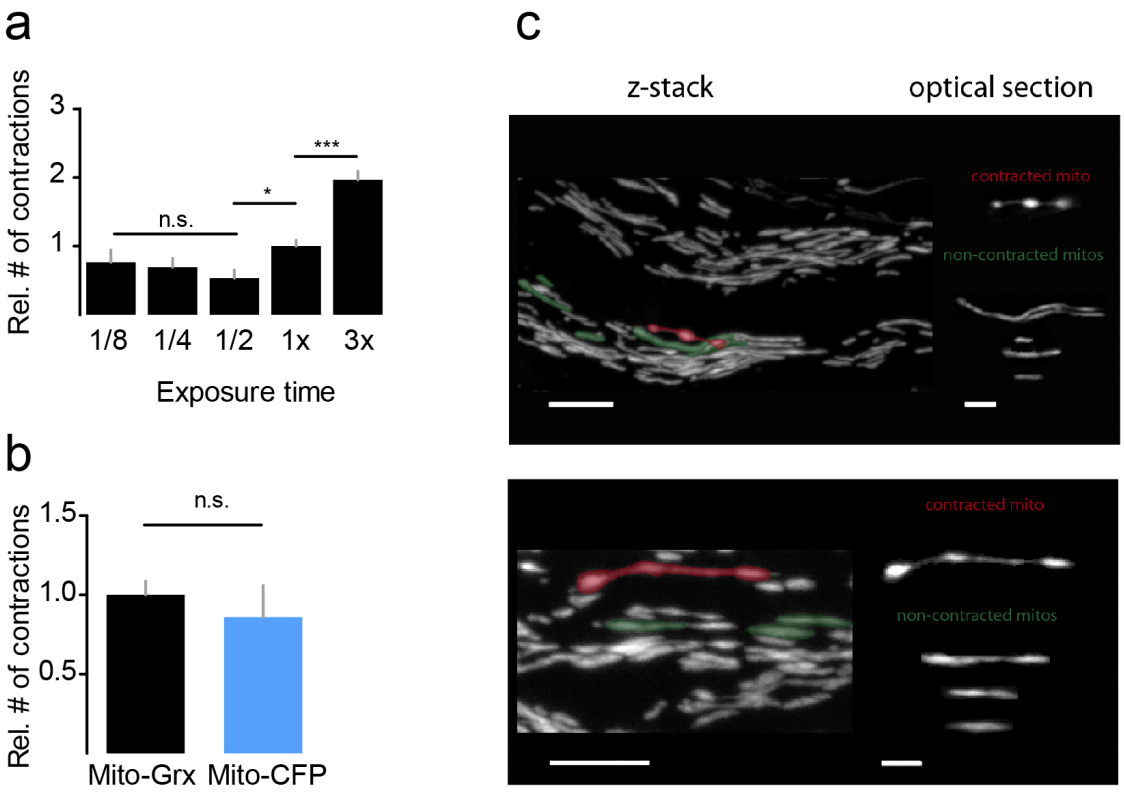

Figure 13: Controls for possible phototoxic effects on contractions.

(a) "Light dose-response" characterization shows a plateau at low light levels. Most experiments were performed at 1x (exposure times: 150ms at 408nm and 30ms at 488 nm; other values normalized to 1x). n = 2 to 5 animals. **(b)** Contractions occur independently of the fluorescent protein used to label mitochondria - *e.g.* the contraction frequency in motor axons does not differ between *Thy1*-mito-Grx1-roGFP2 ("Mito-Grx") and *Thy1*-mito-CFP ("Mito-CFP") mice. n=3-5 animals. **(c)** Two examples of mitochondria with a "pearl-on-string" morphology (pseudo-colored in red) in distal fascicles of intercostal nerves. The other mitochondria do not show morphological "swellings" or any other indication for a contracted state. A couple of "normal looking" mitochondria are pseudo-colored in green. Animals were perfused without prior imaging to exclude phototoxicity. The insets labeled "Optical sections" show a maximum intensity projection of 3-4 confocal planes centered on the organelle of interest (pseudo-colored in full z-stack on left). Scale bar, 5 µm in overview on left and 2 µm in magnified images. Image courtesy of Monika Brill, PhD, Misgeld lab (**c**).

Contractions seem to occur “randomly” in space and time (Fig. 14) and no “visually-apparent” spatial or temporal pattern emerged during the recordings, e.g. a predominance of contractions at the beginning or end of the recordings was not seen (n=214 contractions, 22 mice, Fig. 14). I did not perform a comprehensive statistical analysis to detect more subtle patterns of coherence between adjacent contracting mitochondria. Repetitive mitochondrial contractions were infrequently seen (Fig. 10) but not further analyzed regarding any temporal patterns of these “couplets.”

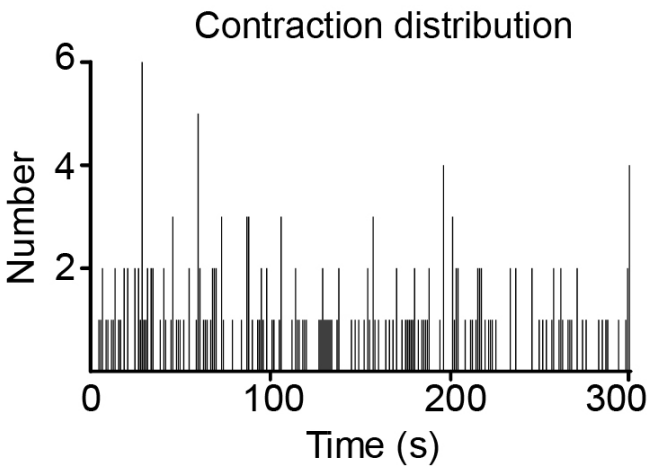

Fig. 14: Occurrence of mitochondrial contractions during recordings
Mitochondrial contractions occurr without apparent distribution during the recordings. The frequncy distribution of contractions is shown as a “spike diagrame” over all 22 recordings (214 contractions).

Deciphering the mechanistic cascade underlying contractions

To further characterize mitochondrial contractions, pharmacological and genetic manipulations were used. Drugs were dissolved in the perfusion solution, and the preparation was incubated for 30 minutes to allow penetration of the drug into the axon. Measurements were performed in the distal intercostal nerve, where pharmacological access is better. Blockage of complex I of the electron transport chain by rotenone led to a decrease of the contraction frequency in a dose-dependent manner (100 nM and 0.1 nM of rotenone $p<0.001$, Fig.15 a). Furthermore, I could show that the matrix acidification and late depolarization is likely mediated by uncoupling proteins, as UCP blockage with the inhibitor genipin (100 µM) diminishes the matrix acidification, as well as the depolarization of the inner membrane ($p<0.01$, Fig.15 b,c).

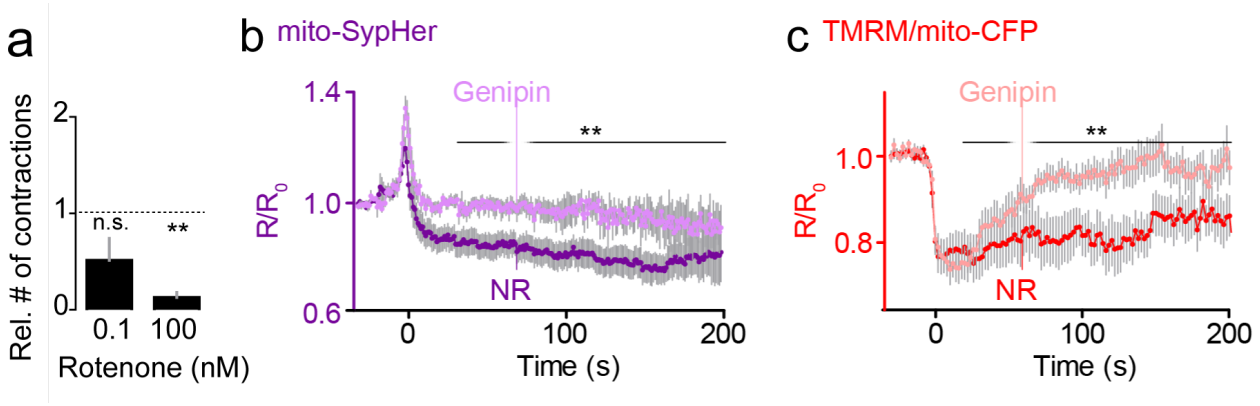

Figure 15: Uncoupling proteins open in the late phase of the contraction

(**a**) Relative contraction frequency during complex I inhibition by rotenone compared to base-line frequency in normal Ringer's solution. (**b**) Quantification of the matrix pH as in (Fig. 11 **f**) in normal Ringer's and during genipin treatment (100 µM) to inhibit uncoupling proteins. (**c**) Quantification of the mitochondrial potential in normal Ringer's and during genipin treatment (100 µM) in explants of *Thy1*-mito-CFP mice loaded with TMRM. Scale bars, 2 µm; * $p < 0.05$, ** $p < 0.01$.

In accordance with the absence of calcium signals during the contraction, application of modulators of mitochondrial calcium handling did not affect mitochondrial contraction frequencies: neither blocking the calcium uniporter with 100 µM Ru-360 (1.7 ±0.24 of baseline), nor blocking the mitochondrial transition pore with 20 µM cyclosporine (1.4 ±0.3) or genetically ablating cyclophilin D (0.9 ±0.1; Schinzel et al., 2005) altered the contraction frequency significantly ($p>0.05$ in comparison to normal Ringer treatment).

Contractions are a marker of various extrinsic and intrinsic stressors

What causes mitochondria to contract?

Mitochondria that will contract within the next 30 seconds do not differ regarding their calcium content nor their pH in comparison to non-contracting mitochondria (Fig. 16 a,b). Also, the cytoplasmic calcium level in the close vicinity of contracting mitochondria is not different (Fig.16 c). However, mitochondria that are prone to contract have a slightly higher redox potential in comparison to surrounding mitochondria in the same axon that will not contract. (408/488 nm ratio: 0.45 ± 0.01 of non-contracting mitochondria, n=279

vs. 0.49 ± 0.01 of contracting mitochondria, n=32, p<0.05, Fig. 16d). This indicates that increased oxidative stress in individual mitochondria makes the organelle susceptible to contract.

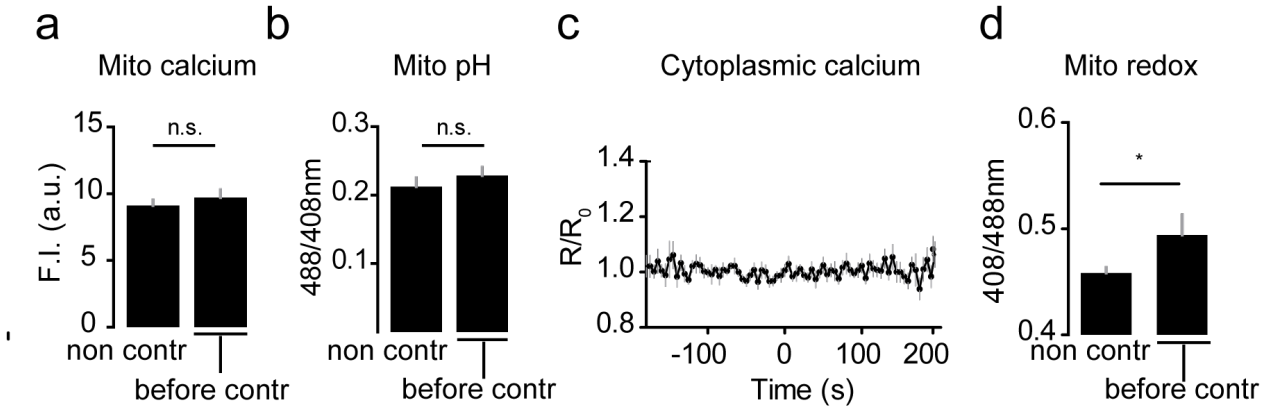

Figure 16: Mitochondrial redox, but not calcium or pH levels, correlate with contractions.

Mitochondria that are prone to contract within the next 30 seconds ("before contr") do not differ in their calcium level (**a**) compared to non-contracting mitochondria in their vicinity ("non-contr") measured in explants from AAV-mito-RGECO1 injected mice. Also the mitochondrial matrix pH between the two populations does not differ significantly, as measured in explants from AAV-mito-SypHer explants (**b**). The cytoplasmic calcium levels adjacent to contracting mitochondria is not altered during contractions, as measured in *Thy1*-TnXXL mice (**c**). However, mitochondria that will contract, have a slightly higher redox potential, as measured in explants from *Thy1*-Grx1-mito-roGFP2 mice (**d**). n≥3 mice per experiment in a-d.

Contractions are affected by oxidative stress

Additional pharmacological screenings of several compounds affecting the redox status of mitochondria show that contractions are induced by exogenous or intrinsic oxidative stress. Application of 50 mM H_2O_2 leads to a ~2-fold increase in contraction frequency, whereas application of the reducing agents 200 mM DTT decreases the contraction frequency. The high pharmacological doses were necessary because these measurements were performed in the thickly myelinated proximal intercostal nerve where pharmacological access is poor.

Additional experiments performed at the distal intercostal nerve with 1 µM of the antioxidant mitoQ (Murphy and Smith, 2007) or by genetically overexpressing MnSOD (Ibrahim et al., 2000) result also in a reduction of the mitochondrial contraction frequency by at least 50% (Fig. 17 a). Further analysis revealed that blockage of uncoupling proteins (UCPs) by 100 µM genipin (Zhang et al., 2006) led to significant mitochondrial oxidation (408/488nm: 0.75±0.01 vs. 0.48±0.01, $p<0.001$), as well a 1.8-fold increase in the contraction frequency. Conversely, inducing UCP activity using the oxidized lipid intermediate, 4-hydroxynonal (HNE, Echtay et al., 2005; Esterbauer et al., 1991) led to a 0.74-fold decrease of contractions and a reduction in the redox level (408/488nm: 0.40±0.01 vs. 0.44±0.01, $p<0.01$). The oxidative burst itself is mitigated by the addition of HNE and mitoQ indicating that the Grx-signal indeed represents an oxidative shift, which can be abrogated by antioxidants (Fig. 17 b). The addition of rotenone decreases the contraction frequency in a dose dependent manner (as shown in Fig. 15 a) and no contraction were discernable anymore after the addition of 1 µM rotenone. Some contractions were still detectable using the intermediate dose of 100 nM rotenone. These contractions however, did not show an oxidative shift anymore (Fig. 17 b), indicating that the activity of the electron transport chain leads to the production of oxidative equivalents.

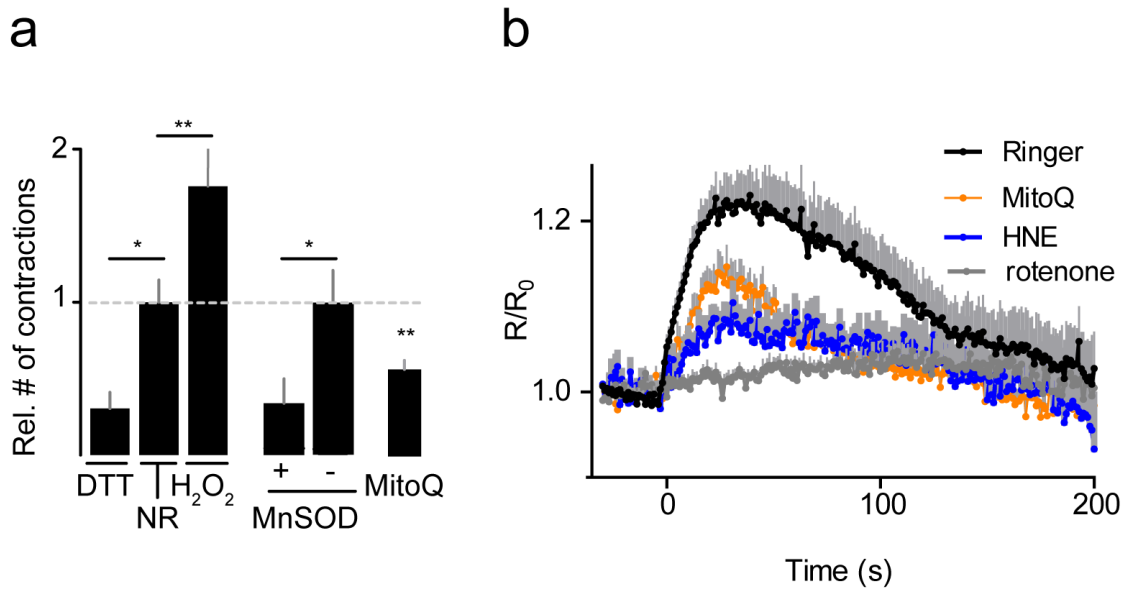

Figure 17: The contraction frequency decreases by the addition of antioxidants

(**a**) Comparison of the frequency of contractions after addition of DTT (200 mM), MitoQ (1 µM) and H_2O_2 (50 mM) and in MnSOD transgenic mice (n ≥ 13 recordings, 3-5 mice per group). The number of contractions is normalized to the number of contractions observed in normal Ringer's solution before the drug was administered or in littermate controls (MnSOD). Note that the high concentrations of DTT and H_2O_2 were used because measurements were performed in the proximal intercostal nerve where pharmacological access is poor. (**b**) Quantification of the redox potential during the contraction using various pharmacological treatments. Note that the oxidative shift is markedly mitigated by the treatment with HNE (35 µM) and MitoQ (1 µM).

Neuronal activity causes oxidation of the glutathione pool and contractions

In the next set of experiments I investigated whether physiological stimuli would alter mitochondrial redox levels and contraction frequencies. The primary function of neurons is to convey action potentials and thus transmit electrical signals over long distances. The constant de- and repolarization requires large amounts of ATP, which is primarily produced by mitochondria. How mitochondria respond to neuronal activity and an increase in the neuronal ATP demand is not well understood. In order to investigate this interplay, I performed experiments, during which I stimulated the intercostal nerve in triangularis sterni explants with a suction electrode. Stimulation as low as 1 Hz led to an increase of the redox potential in ICN and NMJ mitochondria. Mitochondria show long-

lasting elevations of their redox potential upon stimulation. Fig. 18 a shows a group of mitochondria before and after stimulation. The effect of neuronal activity is even more pronounced at 10 Hz (408/488nm: 0.47±0.01 vs. 0.43±0.01, $p<0.05$, 3-5 mice, Fig. 18b). This effect could be completely abolished by blocking action potential conduction with the voltage-gated Na^+-channel blocker TTX. The frequency of mitochondrial contractions also increased significantly after 10 Hz stimulation compared to baseline levels (2.5-fold increase of the contraction frequency, $p<0.05$, Fig. 18 c,d). The effect of the stimulation is sustained for minutes beyond the stimulation period indicating that a long-lasting alteration of metabolic activity is induced by neuronal activity. The underlying signaling remains unknown and is a topic of future investigation my host lab. Possible candidates would be *e.g.* a cation influx of Ca^{2+} or Na^+, or activity-dependent phosphorylation of proteins that regulate mitochondrial respiration. The altered mitochondrial redox state that results could itself convey signals via redox-sensitive modification of cystein residues in signaling proteins.

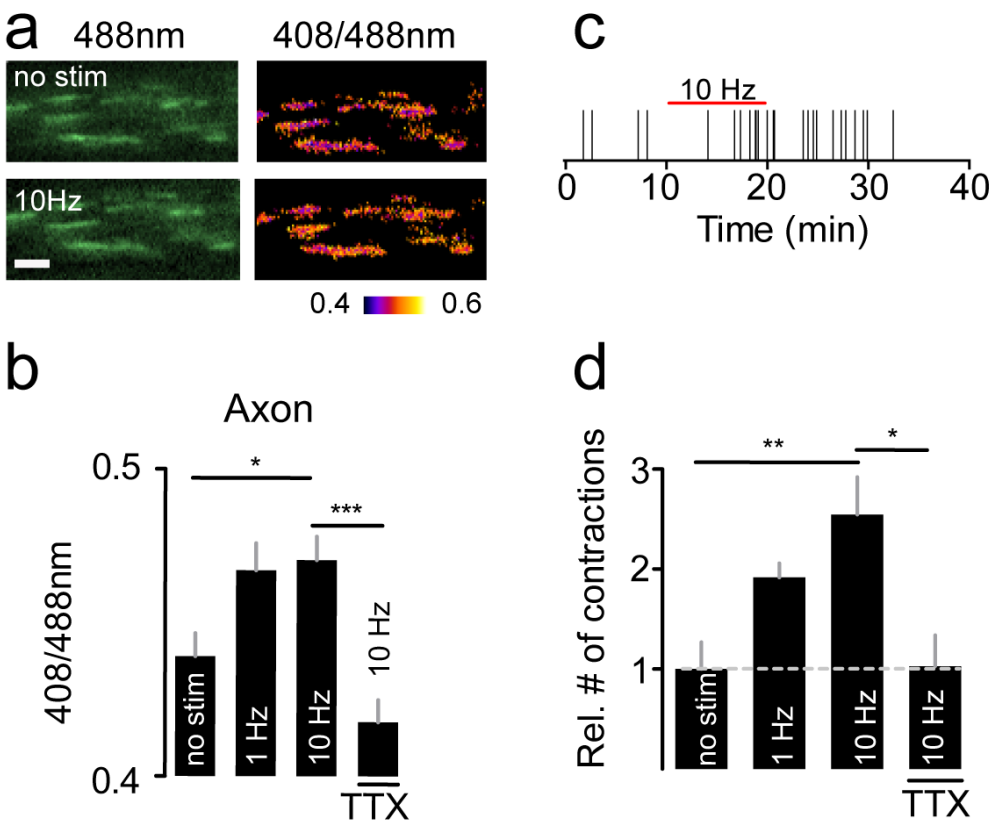

Figure 18: Mitochondrial contractions occur in response to physiological stressors

(**a**) Images show a group of mitochondria before and after electrical stimulation of the intercostal nerve with a suction electrode (10 Hz stimulation for 10 min). Note that the mitochondria have a slightly higher redox levels after electrical activity of the nerve. (**b**) Redox state of mitochondria after stimulation. (**c**) Representative "event plot" illustrating the occurrence of contractions during an electrical stimulation experiment. Red bar shows the time period of electrical stimulation with 10 Hz. Note that the increased contraction frequency is sustained beyond the stimulation period. (**d**) Bar graphs showing the relative frequency of contractions before ("no stim") and during stimulation. Significance was determined using the Kruskal-Wallis test with Dunn *post hoc* analysis. Tetrodotoxin (TTX, 1 µM) was used to block action potential conduction (n ≥ 78 mitochondria, 3-5 mice per group).

Mitochondrial redox signals during axonal pathology *in vivo*

In addition to investigating redox signaling under physiological conditions, the main motivation for the generation of these novel mouse lines was to determine the role of mitochondrial redox signals during pathological states. Therefore, I established a model of acute neurodegeneration following axotomy.

First, I further characterized the sensor`s *in vivo* properties. After ketamine/xylazine anesthesia of *Thy1*-mito-Grx1-roGFP2 mice a small laminectomy was performed at lumbar vertebra 1 to 3 (Nikić et al., 2011). The dorsal funiculus of the spinal cord is then accessible for *in vivo* imaging. The emission spectra of the sensor in its reduced (200 mM DTT) and oxidized state (50 mM H_2O_2) were measured by tuning the 2 photon laser in 10 nm steps while measuring the emission intensity at each excitation wavelength (Fig. 19 a,b). It turned out that 800 nm and 940 nm were optimal to ratiometrically read out the redox potential, similarly to previous reports that used 800/900 nm for ratiometric roGFP imaging (Xie et al., 2013). A dose response experiment measured *in vivo* in the spinal cord and performed analogously to the *ex vivo* dose response using increasing H_2O_2 doses (0.5, 1, 5, 10, 50, 100 mM) showed the same dynamic range of 2.6 as measured *ex vivo* (Fig. 19 c,d), albeit with different absolute concentrations due to reduced drug access.

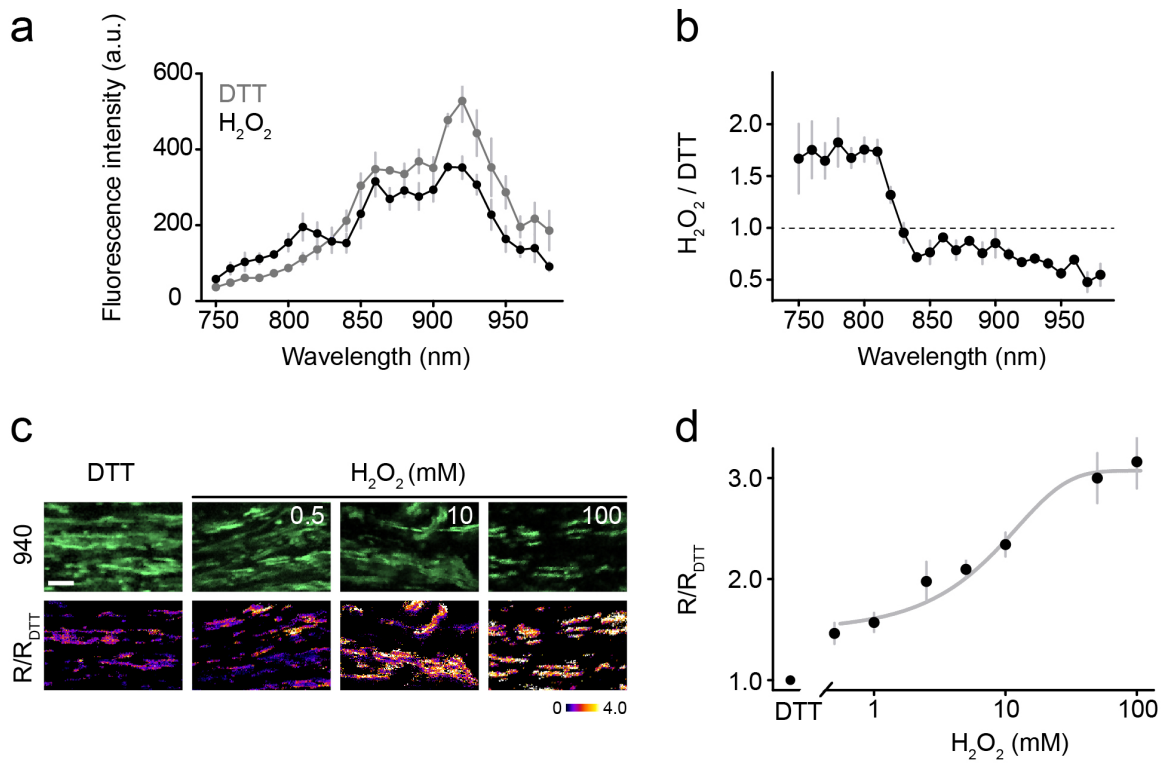

Figure 19: Two-photon properties of the redox sensor in *Thy1*-mito-Grx1-roGFP2 mice

(**a**) Emission spectrum of Grx1-roGFP2 in the fully reduced (200 mM DTT) and fully oxidized state (50 mM H_2O_2) measured in the spinal cord (n = 3 mice). (**b**) Ratio of the emission spectra (H_2O_2/DTT). (**c**) Pseudo-colored images (R/R_{DTT}) of spinal cord mitochondria upon administration of 200 mM DTT and 0.5, 10 or 100 mM H_2O_2. (**d**) *In vivo* dose-response curve showing a comparable dynamic range to the *ex vivo* dose-response. Note that high (millimolar) H_2O_2 doses were necessary to penetrate the dura mater, as the dura was kept intact in these experiments and pharmacological access is poor (n = 15 mitochondrial clusters, 3 mice). Scale bar 10 µm in (**c**).

During axotomy mitochondria oxidize and shorten

I laser-transected single axons by focusing a pulsed 2 photon laser on a small circle (~25 µm in diameter; Steinmeyer et al., 2010; Yanik et al., 2004). I made use of such axotomies both in triangularis sterni explants, as well as in the spinal cord of living mice. First, I strived to understand the long-term implications of such a lesion (on the order of hours) and imaged a large field of view (x-y dimensions of ~500 µm in x and ~300 µm in y) with 2-photon microscopy over 4 hours. After the lesion was induced, the glutathione

redox potential increases over the entire time of investigation in the transected axons. In addition to the oxidative shift, mitochondria at the lesion site became rounded (Fig. 20 a-d). These changes happened rapidly and could be observed already after 5 min. Rounding and oxidation of mitochondria was also seen 400 to 500 µm away from the lesion in transected axons, though to a lesser degree. Outside of the lesion - in non-transected axons - no apparent changes were detected. Similar results were obtained in a mechanical pin injury model (Fig 20 b, Kerschensteiner et al., 2005).

Four hours after the laser axotomy, acute axonal degeneration (AAD) was assessed with an average axon dieback of 53 µm ± 9.1 µm (n=12 axons, 2 mice). The extent of axonal dieback is less than reported previously (Kerschensteiner et al., 2005), possibly because of the different injury models (laser lesion *vs.* pin injury) or the different site of injury (lumbar *vs.* cervical spinal cord). AAD was quantified in fixed whole mount preparations of the spinal cord using *Thy1*-mito-Grx1-roGFP2 mice crossed to *Thy1*-OFP mice (Fig. 21) to co-visualize mitochondria and the axonal cytoplasm.

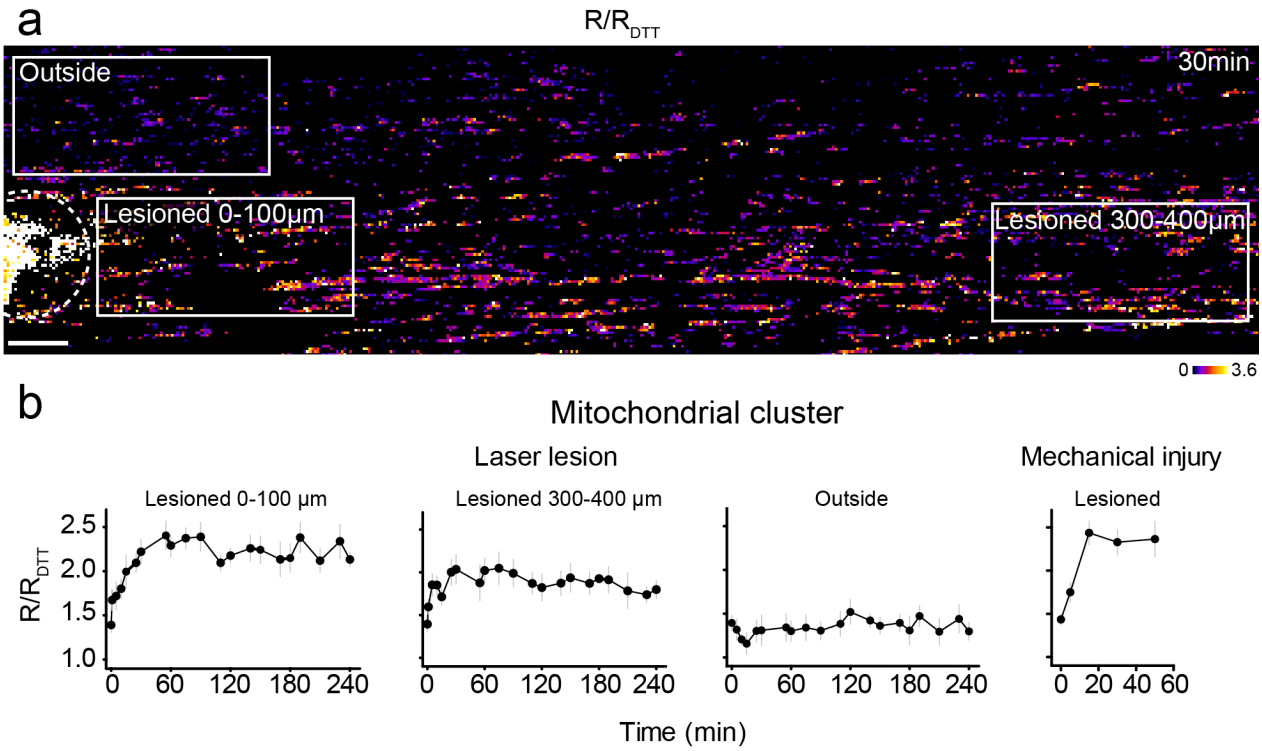

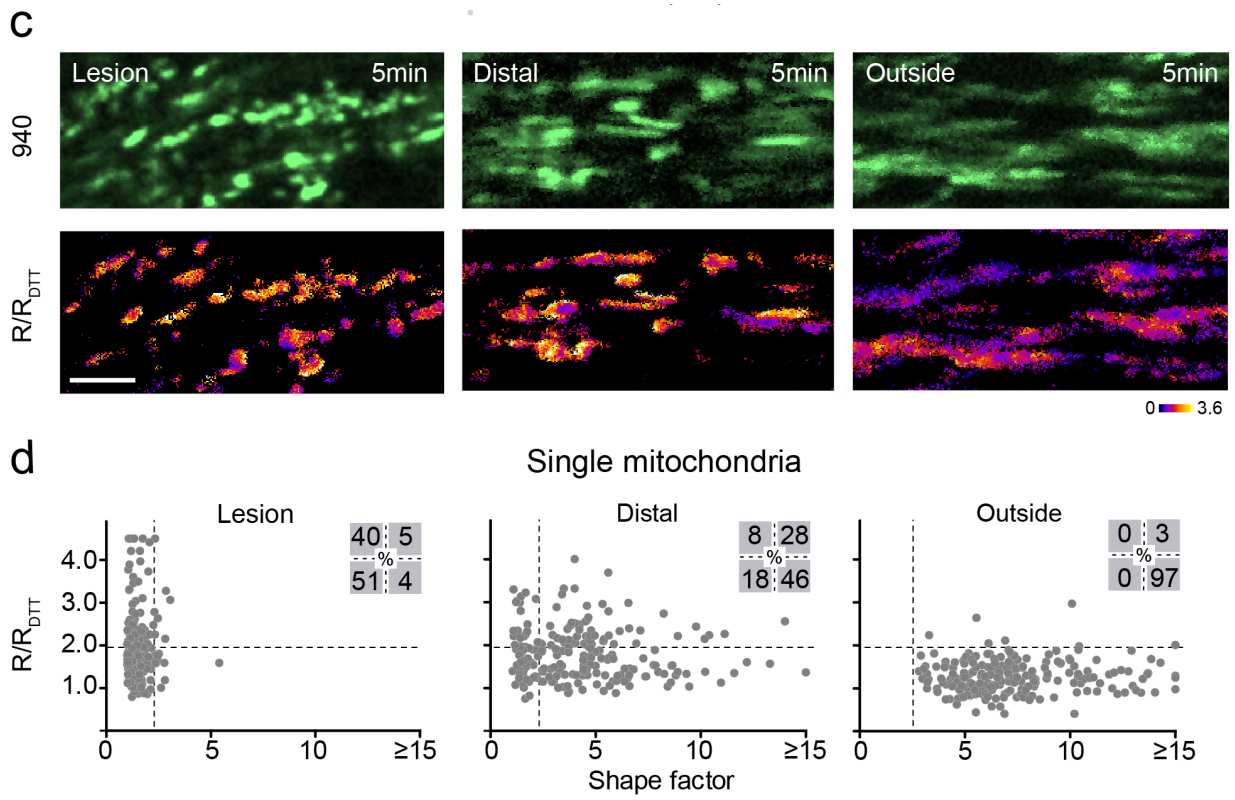

Figure 20: Two-photon imaging of mitochondrial shape and redox changes after spinal cord injury

(**a**) Two-photon ratiometric image acquired 30 min after laser lesion induction (indicated by dashed circle) in the spinal cord. (**b**) Quantification of the redox changes after laser axotomy at 0-100 µm and 300-400 µm from the site of transection as well as outside of the lesion area ("Outside", n > 5 mice). Right panel shows the quantification of redox changes after mechanical transection of axons in the spinal cord (measured adjacent to the lesion site, n = 3 mice). (**c**) High power two-photon images acquired 5 min after laser lesion at different distances from the lesion and outside of the lesion area ("Outside"). (**d**) Quantification of the mitochondrial shape factor and redox state (R/R_{DTT}; n > 200 mitochondria, 3 mice). Insets show percent of all mitochondria in the respective quadrants. Scale bars, 25 µm in (**a**), 5 µm in (**c**).

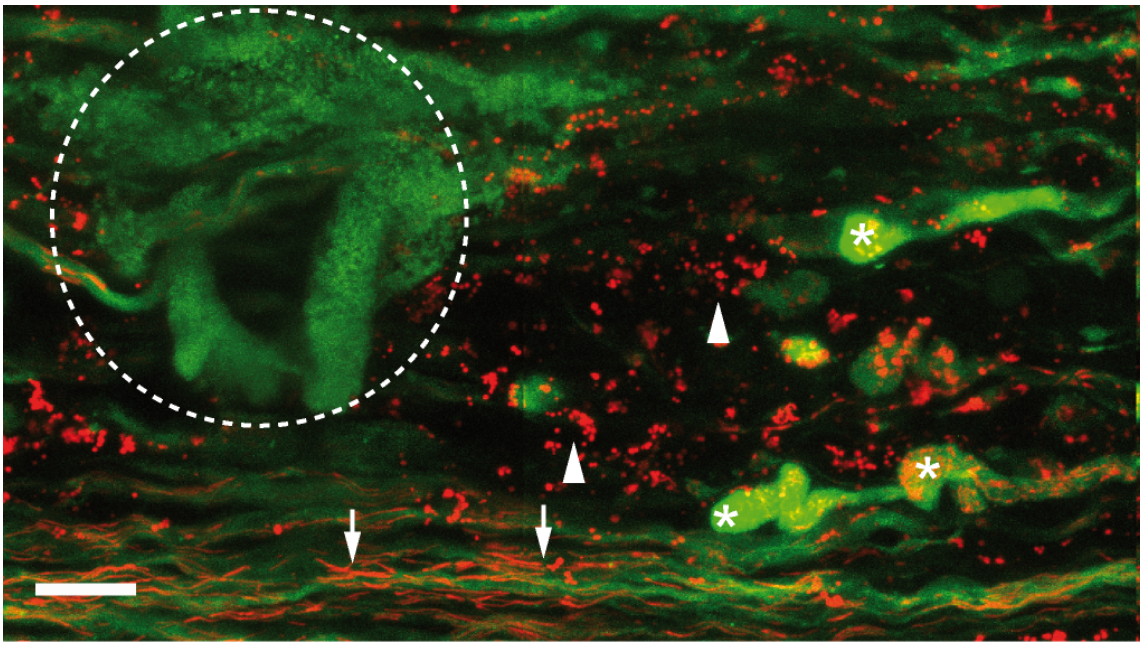

Figure 21: Laser lesion in the spinal cord leads to acute axonal degeneration

Confocal reconstruction of a whole-mount spinal cord preparation of a *Thy*1-mito-Grx1-roGFP2 x *Thy1*-OFP mouse after laser lesion. The animal was sacrificed four hours after induction of the lesion. The spinal cord was dissected and post-fixed in PFA and 30% sucrose. The image shows the lesioned area (dashed circle), axon dieback (acute axonal degeneration, which results in bulb-tipped axons, *), mitochondrial fragmentation and rounding (arrowhead) and unaffected non-transected axons with healthy looking mitochondria (arrow). OFP is colored in green, mito-roGFP2 in red. Scale bar 10 µm.

Spatial and temporal dynamics of mitochondrial redox shifts after axotomy

As switching between excitation wavelengths in the 2-photon approach is relatively slow (as no 2 photon systems with two lasers sharing the same light-path was available to me), the temporal resolution to detect mitochondrial shape and redox changes by 2 photon microscopy was limited. To circumnavigate this limitation, I established confocal ratiometric imaging *in vivo*, which promised higher temporal resolution. Indeed, the confocal approach proved to have better temporal (and spatial) resolution to reveal the dynamics of the redox changes associated with axotomies. Confocal microscopy using a 50/50 beamsplitter and line sequential scanning (line scan duration ~5 msec) enabled the resolution of a wave of “spreading oxidation”. This spreading oxidation occured after the laser lesion at the site of injury and traveled from transection along the axon.

Concomitantly to oxidation, mitochondria shortened by ~60%, a process that involves both rounding and fragmentation (fission) of mitochondria (Fig. 22 a,b). The speed of the oxidative spread can be estimated as 2.4 µm/sec. This was faster than the occurrence of the shape changes (1.4 µm/sec, Fig. 22c). The oxidation is persistent over hours and can be observed at least over 120 µm away from the lesion site. Unfortunately it is difficult to assess how far the oxidation spreads in the rostro-caudal direction and where it might stop due to the limited field of view. Axons often “dive” into the depth of the spinal cord where they cannot be tracked by confocal microscopy. Importantly, mitochondria within axons, that have not been laser-transected, do neither show morphological nor redox alterations during the entire imaging time (Fig. 22d).

Antioxidants do not prevent mitochondrial shape changes

In order to better understand the role of the spreading oxidation and to test whether this is the cause or consequence of the mitochondrial shape change I blocked mitochondrial oxidation pharmacologically with N-acetylcystein (NAC, 1 mM) and genetically using mice that overexpress the antioxidative enzyme MnSOD within mitochondria (Ibrahim et al., 2000; Kiningham et al., 1999; Miriyala et al., 2012). Even though I could block oxidation effectively, the shape changes of mitochondria still persisted. This established that mitochondrial oxidation is not a prerequisite for the morphological alteration (Fig. 22 d).

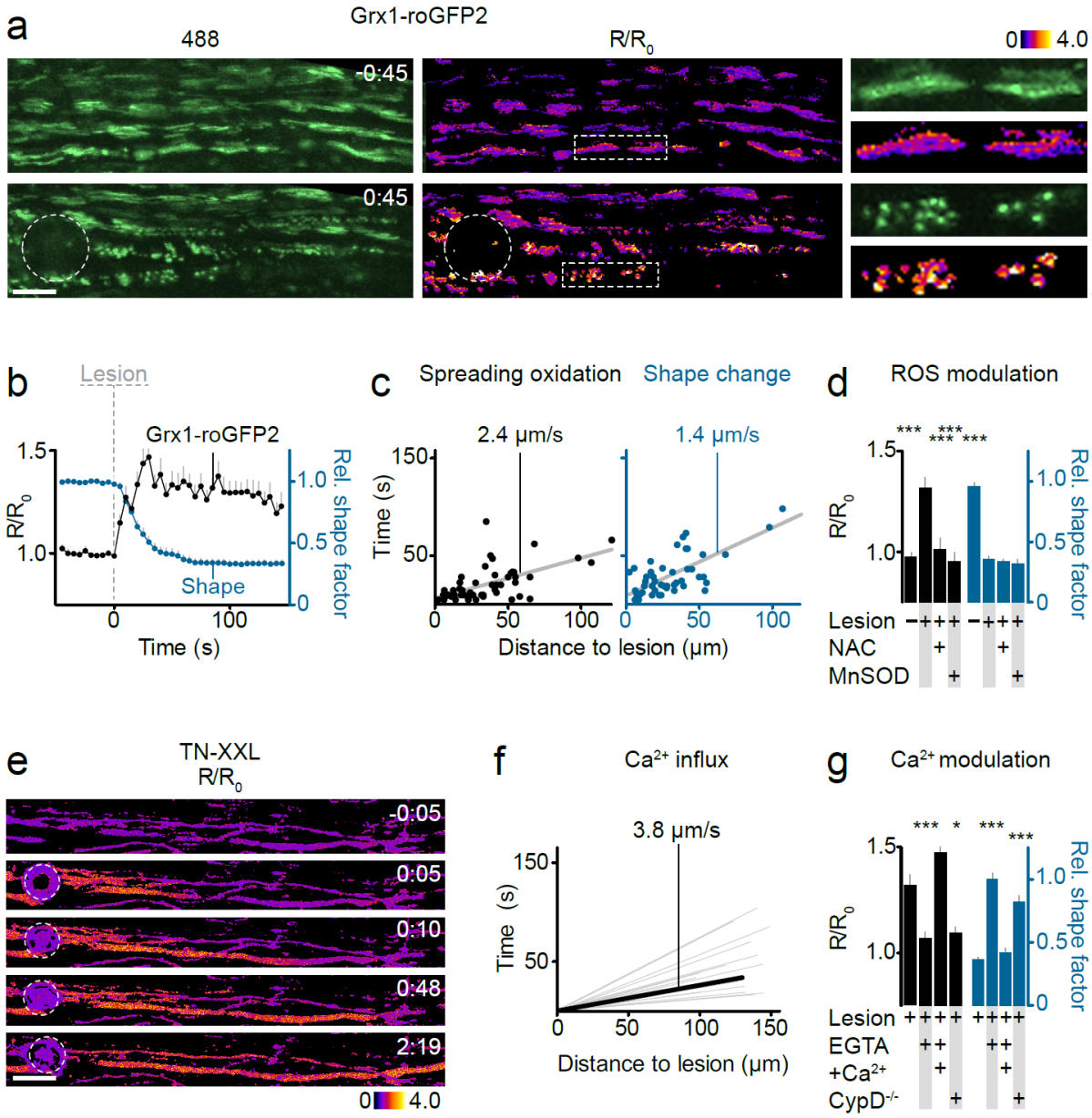

Figure 22: Axotomy induces spreading mitochondrial oxidation and structural alterations caused by the influx of extracellular calcium

(**a**) Laser axotomy in the spinal cord *in vivo*, imaged by ratiometric confocal microscopy. Images show several parallel-running axons before and after lesion induction (min:sec). Dashed circle indicates where the lesion was induced. Magnified insets (boxed in **middle** panels) show examples of mitochondria undergoing fragmentation and sensor oxidation. (**b**) Single mitochondrial dynamics after axotomy. Probe oxidation and shape factor are quantified in mitochondria of transected axons (0-50 µm away from the lesion site; n > 39 mitochondria, 4 mice). (**c**) Quantification of the spread (time to 50% change) of probe oxidation and mitochondrial shape changes along transected axons (n > 48 mitochondria, 4 mice). (**d**) Treatment with N-acetylcysteine ("NAC", 1mM) and over-

expression of MnSOD prevented the shift in the mitochondrial glutathione redox potential, but not mitochondrial shape changes in lesioned axons ("Lesion +"). "Lesion -" indicates mitochondria in non-transected axons. All statistical tests were performed in comparison to "Lesion +" condition; all values are normalized to mean before injury (n > 14 mitochondria, 3 mice for each condition). (**e**) *In vivo* two-photon time-lapse recording of the calcium increase in spinal axons induced by laser lesion (dashed circle) in *Thy1*-TN-XXL mice (time, min:sec before and after axotomy). (**f**) Speed of calcium spread along transected axons. The light grey lines represent the average speed for individual axons; their length indicates the distance of the most distal measurement point from the lesion (n = 16 axons from 3 mice). (**g**) Depletion of extracellular calcium ("EGTA") prevents mitochondrial shape changes and oxidation. After calcium is added back into the medium, mitochondria fragment and oxidize. Knockout of cyclophilin D ("CypD") blunts mitochondrial oxidation and shape changes compared to wildtype animals. All statistical tests were performed in comparison to "Lesion +" condition; values normalized to mean before injury (n > 14 mitochondria, 3 mice for each condition). Scale bars, 10 µm in (**a**) and 25 µm in (**e**).

Calcium influx is necessary and sufficient to cause mitochondrial pathology

As calcium is known to be an important second messenger in injury conditions, including axotomy (George et al., 1995; Stirling and Stys, 2010), I tested whether calcium elevations occur in the laser axotomy model using *Thy1*-TnXXL calcium indicator mice (Heim et al., 2007). Indeed, a spreading calcium wave was initiated at the lesion site that propagated even faster along the axon than the mitochondrial alterations (3.8 µm/s, Fig. 20 e,f). Mechanistically, exchanging Ca^{2+} by Mg^{2+} in maCSF and additionally chelating Ca^{2+} with 5 mM EGTA had drastic effects in the axotomy paradigm: the calcium rise could be almost completely abolished ($p<0.01$) and mitochondria showed neither shape alterations nor oxidation. When the modified maCSF was exchanged with normal maCSF containing calcium, mitochondria immediately started to fragment and to oxidize even when the lesion was induced already several minutes before (Fig. 22 g). This established that calcium entry into mitochondria and the axon is both necessary and sufficient for the mitochondrial - as well as the axonal pathology (George et al., 1995; Stirling and Stys, 2010).

Knockout of cyclophilin D mitigates mitochondrial pathology

Cyclophilin D mediates the opening of the mitochondrial permeability transition pore following mitochondrial calcium overload (Giorgio et al., 2013; Schinzel et al., 2005). Pore transitioning then leads to release of cytochrome C from the mitochondrial matrix into the cytoplasm and the initiation of apoptosis. Knockdown of cyclophilin D allows mitochondria to buffer more calcium before permeability pore transitioning occurs. Laser axotomies in *Thy1*-mito-Grx1-roGFP2 x cyclophilin D $^{-/-}$ knockout mice showed that the mitochondrial pathology is mitigated in terms of mitochondrial oxidation and shape changes compared to wildtype mice (Fig. 22 g). This further establishes the role of calcium as the driver of mitochondrial pathology. The protection of mitochondria by the knockdown of cyclophilin D was gene-dose dependent and heterozygous cyclophilin D $^{-/-}$ knockout mice showed partial protection of mitochondrial shape and redox level.

Anesthesia is not a confounding factor of redox signals

Mitochondria can be impaired in their function by anesthesia (Boscolo et al., 2013; Zhang et al., 2012). In order to ascertain that the phenomena I observed under KX anesthesia were not confounded, I repeated the axotomy experiments using two different classes of general anesthesia. Axotomies under isoflurane, as well as with triple-combination injection anesthesia (fentanyl, midazolam, medetomidin; Mrsic-Flogel et al., 2007), resulted in similar effects on the single mitochondria level compared to KX anesthesia. Spreading oxidation and the profound shape changes were seen (Fig. 23 a-d). Baseline glutathione oxidation was slightly lower under isoflurane anesthesia (Fig. 23 e). Mitochondrial redox and shape was not altered in non-transected axons that run close to the lesion, indicating that the laser lesion induces very local damage to the targeted, transected axon without disturbing surrounding axons (Fig. 23 f).

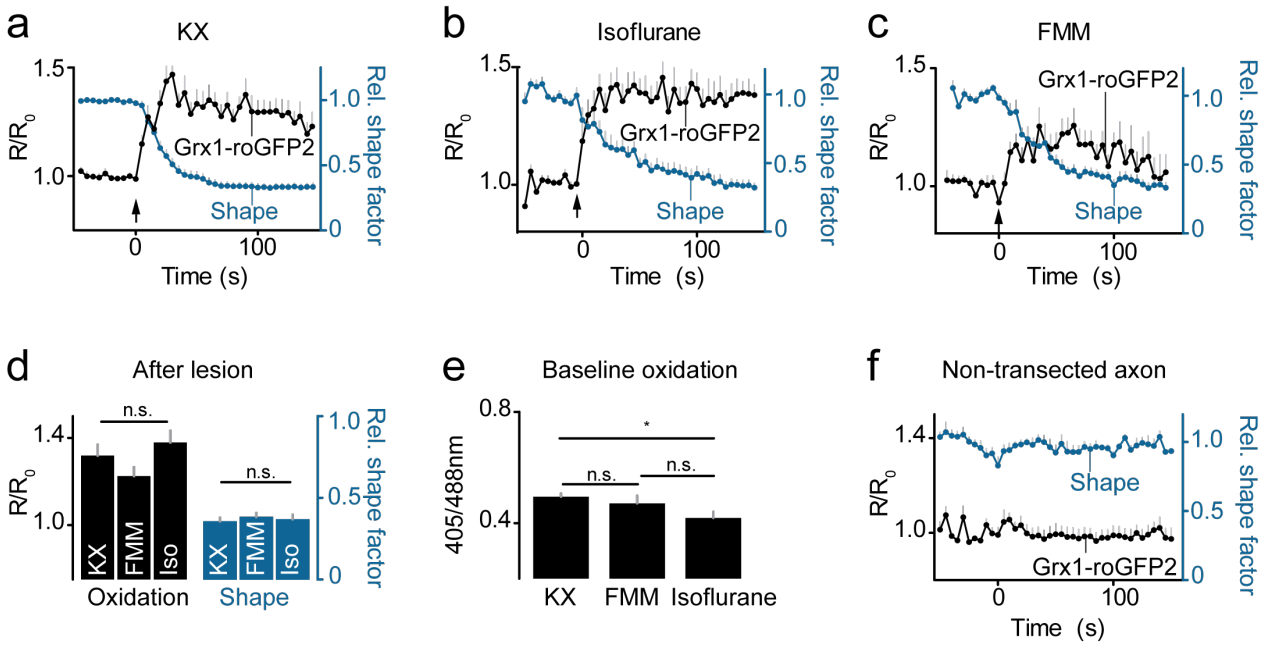

Figure 23: Different anesthetic regimes yield comparable results

Quantification of mitochondrial oxidation and shape changes after laser lesion induction *in vivo* using KX (n=59 mitochondria, **a**), isoflurane (n=4 mitochondria, **b**) and fentanyl, midazolam, medetomidin (FMM, n=12 mitochondria, **c**). The different anesthesia regimes show no significant differences regarding mitochondrial oxidation and rounding ($p>0.05$, ANOVA with Bonferoni *post-hoc* testing, "iso"=isoflurane, **d**). Baseline levels of mitochondrial redox levels before the lesion were slightly lower with isoflurane anesthesia (**e**). Mitochondrial redox and shape in neighbouring, non-transected axons was not altered by laser lesion induction (n=10 mitochondria, **f**). n ≥ 3 mice for all experiments.

Multiparametric imaging to dissect the sequence of pathology

Using the viral-transduction techniques described above, molecular sensors to additionally assay mitochondrial pH (SypHer) and calcium dynamics (GCaMP-3, RGECO-1) were expressed in triangularis sterni explants and subjected to laser axotomies. Spreading oxidation, as well as the shortening and rounding of mitochondria, can also be seen in motor axons of the intercostal nerve after laser axotomy (Fig. 24 a). Mitochondria acidify quickly after axotomy, probably due to the sudden dissipation of the proton motive force as pore transitioning takes place (Fig. 24 b). Disruption of the plasma membrane leads to a severe calcium influx into the cytoplasm (Fig. 24 c) which is taken up by mitochondria (Fig. 24 d,e). In summary, multi-parametric imaging by

combinatorial genetic labeling allowed assaying key mediators of mitochondrial pathology after axotomy. In the future, this approach could allow determining the exact temporal sequence of molecular signaling events. The axotomy paradigm could be used for pharmacological and genetic screenings to decipher pathways that mediate axonal protection and preserve neuronal function.

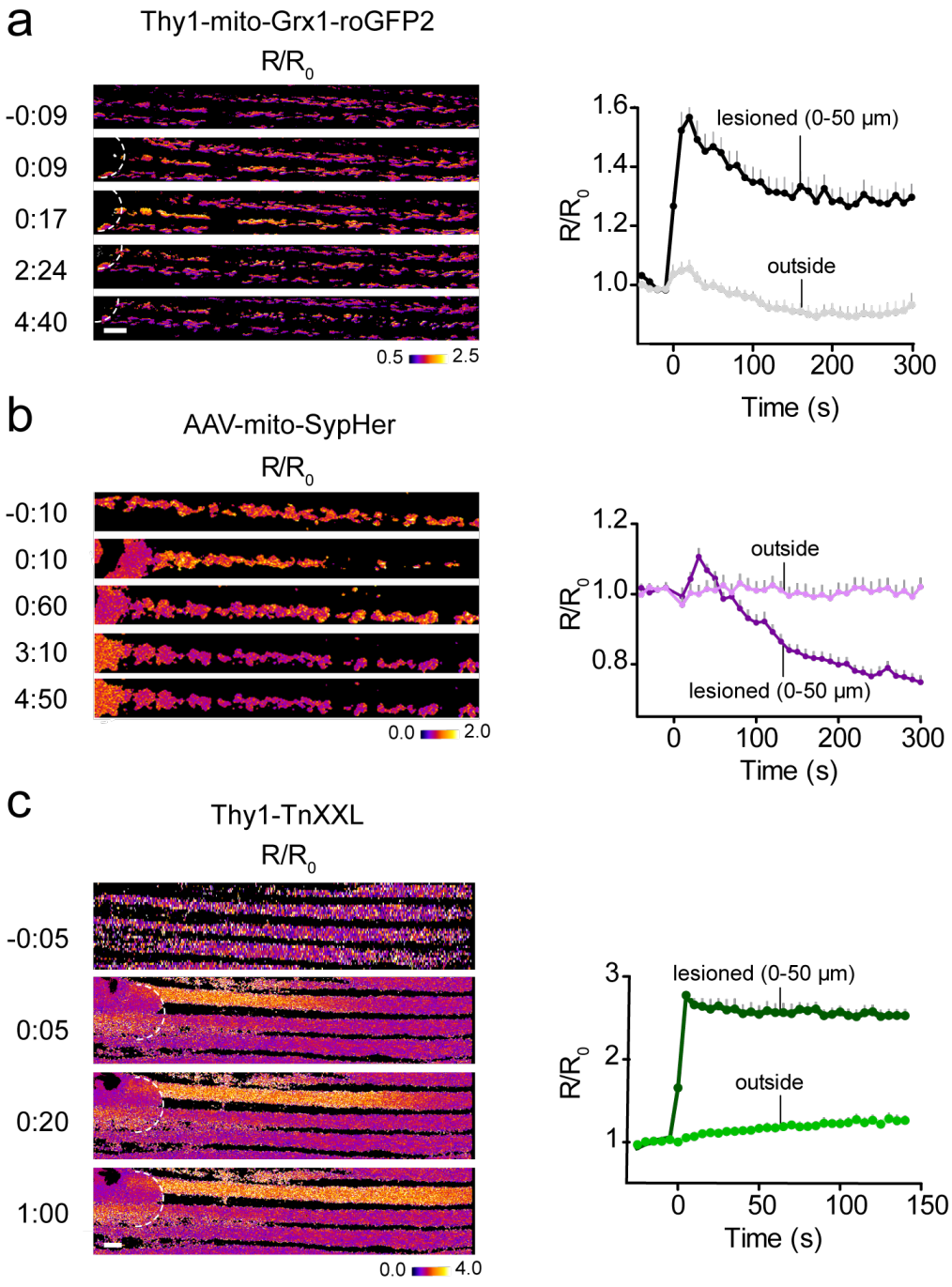

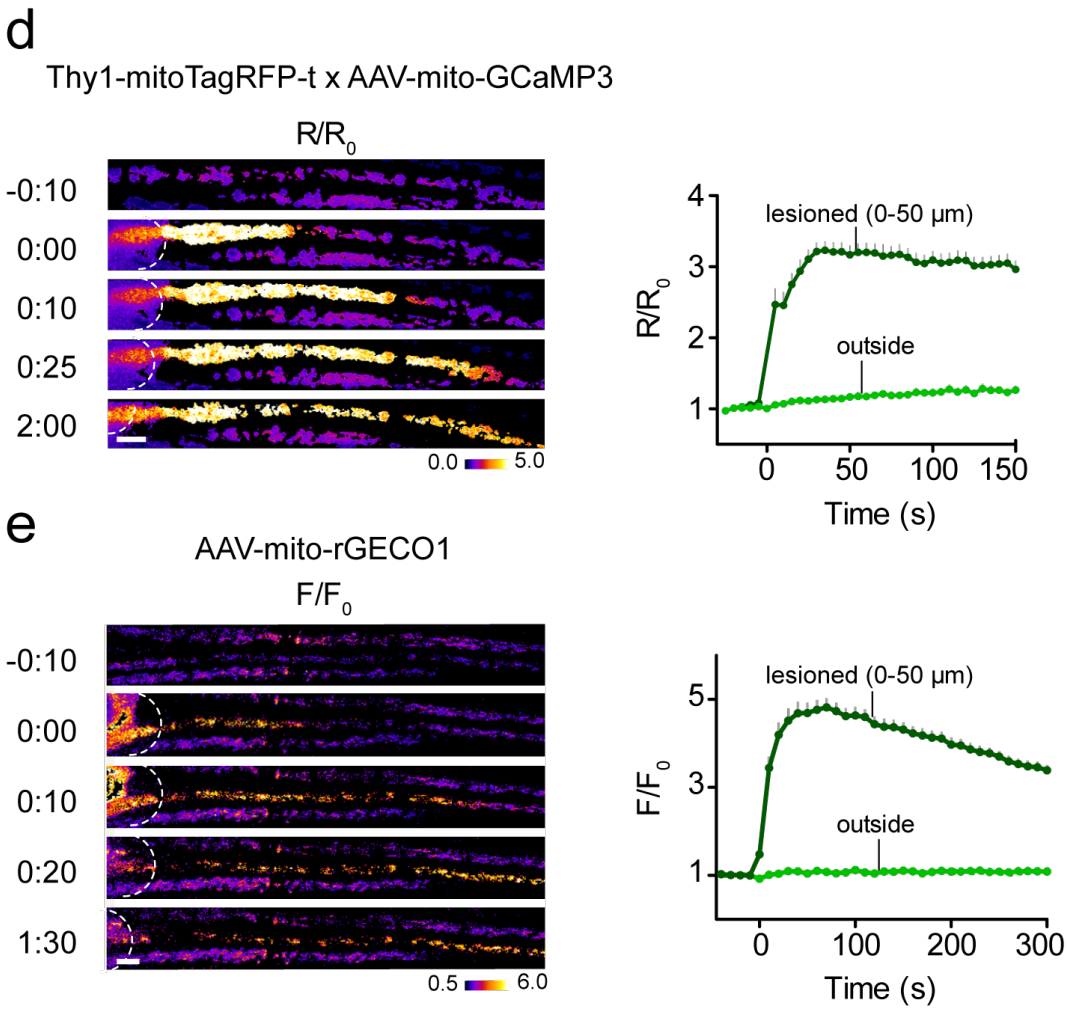

Figure 24: Multi-parametric imaging of mitochondrial dynamics after axotomy in the triangularis sterni explant

(**a-d**) Laser axotomies in triangularis sterni explants imaged by confocal microscopy. Images show several parallel-running axons before and after lesion induction (time, min:sec). Dashed circles indicate where the lesion was induced. Quantifications show single mitochondrial dynamics in lesioned axons (0-50 µm away from the lesion site) and unlesioned axons ("outside"). (**a**) Axotomy induced in explants of *Thy1*-mito-Grx1-roGFP2 mice. (**b**) Axotomy induced in explants prepared from wild-type mice injected with rAAV-mito-SypHer to measure pH alterations. (**c**) Axotomy induced in explants prepared from *Thy1*-TnXXL mice measuring cytoplasmic calcium levels. (**d**,**e**) Axotomy induced in explants prepared from *Thy1*-mitoTagRFP-t mice (**d**) injected with rAAV-mito-GCaMP-3 and (**e**) from wild-type mice injected with rAAV-mito-RGECO-1 to measure changes in matrix calcium (n >27 mitochondria, 2 mice for each sensor in **a-e**). Scale bars in all panels equal 5 µm.

Peripheral nerve crush leads to an increase of contractions

Might there be a link of permanent mitochondrial pathology after axotomy and reversible mitochondrial contractions as described in the first part of my work? In order to further assess the role of mitochondrial contractions during pathology, I used a model of acute nerve crush injury in the triangularis sterni preparation. Moderate pressure was applied on the intercostal nerve for 5-10 seconds with forceps under visual guidance and imaging was started immediately after the crush on a wide-field microscope. This allowed faster imaging (1 Hz) compared to the confocal microscopy approach and a better characterization of the mitochondrial pathology. I found that mitochondrial contractions are induced after the crush (~3.6 fold, Fig. 25 a,b). Interestingly, these contractions often last longer compared to the non-injury condition and ~82% are "irreversible" (over the imaging period), a phenomenon not seen under physiological conditions. Intriguingly, the oxidative status of mitochondria is closely related to the morphological state and contraction length of a mitochondrion (Fig. 25 c,d).

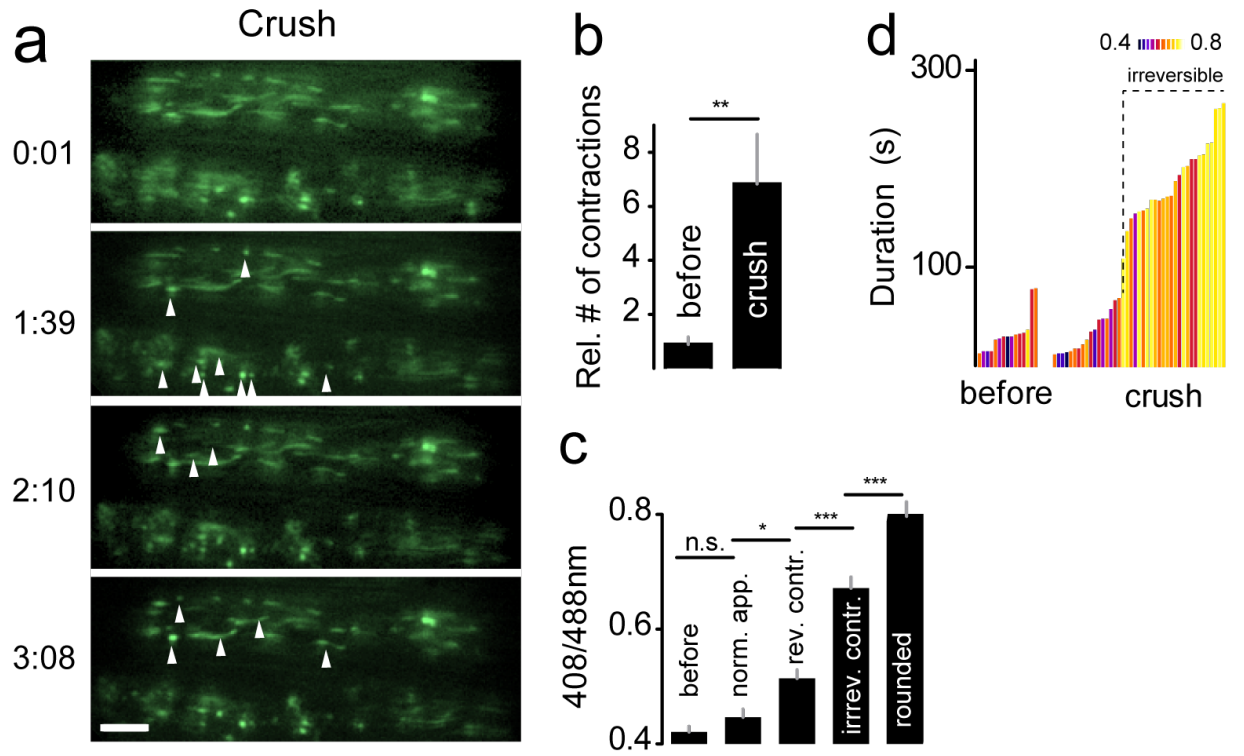

Figure 25: Mitochondria contract and oxidize after peripheral nerve crush

(**a**) Image series of a time-lapse movie showing multiple irreversible contractions (white arrowheads). Crush was induced to the left of the imaging field at time-point 0:00 (min:sec). (**b**) Number of contractions before and after crush (n ≥ 5 mice per group, significance was determined using the Mann-Whitney test). (**c**) The redox state is correlated to the morphological state. Mitochondrial redox levels before and after the crush. Several mitochondrial categories can be differentiated (normal appearing - “norm. app.”; reversible contracting - “rev. contr.”; irreversible contracting - “irrev. contr.” and rounded mitochondria) (**d**) Duration of contractions before and after the crush (n ≥ 5 mice per group). Each spike represents the duration of a single contraction (ordered by increasing duration). Contractions were considered irreversible if they lasted for at least 100 sec (mean + 2 times standard deviation of before group) and did not recover within the imaging period. Spikes are pseudo-colored according to the redox state of the mitochondrion during the contraction. Scale bar in (**a**) 2 µm.

In an ALS model contractions increase in frequency during the disease course

I acknowledge the help of Franz Pfister, MD (Kerschensteiner lab) and Petar Marinković, PhD (Misgeld lab) who mainly acquired ALS data.

Could chronic neuronal insults lead to mitochondrial changes that resemble what is found after acute injury? We tested this hypothesis in a model of ALS (SOD^{G93A}) crossed to *Thy1*-mito-Grx1-roGFP2 mice. SOD^{G93A} is a mutation found in human ALS, which was used for transgenic expression in mice (Gurney et al., 1994; Song et al., 2012). SOD^{G93A} mice develop a progressive motor neuron disease with motor weakness, altered mitochondrial transport and axon degeneration (Marinkovic et al., 2012; Parone et al., 2013). We found severe perturbations of the mitochondrial morphology and redox status that are progressing during the disease course (p90 *vs.* p135, Fig. 26 a-b). First mitochondria show morphological shortening, before ~21% exhibit increased oxidative levels at p135. The shortening of mitochondria almost seems like a prerequisite for oxidation as the percentage of mitochondria with elevated redox levels and normal shape factor is negligible (4% at p135). Whether mitochondrial shortening (and oxidation) has purely detrimental effects or might even be a protective reaction is unknown. Within a given axon, mitochondrial morphology and redox status are quite homogenous (Fig. 26 c), arguing against local "hot-spots" of damage. Of note is that also at late stages of the disease, axons with totally normal mitochondria can be found. These axons might represent disease-refractory motor axon subsets or sensory projections (Saxena and Caroni, 2011; Saxena et al., 2009). At late stages of the disease (p90 and p120), mitochondrial contractions are significantly increased compared to non-affected littermates. The length of contractions in SOD^{G93A} mice is also prolonged (Fig. 26 d,e). In contrast to the nerve crush experiments the vast majority of contractions in SOD^{G93A} animals is reversible. This is compatible with either a much slower progression from increased contraction-susceptibility to permanent morphological damage, or two different injury cascades (as revealed after axotomy). In the future, multi-parametric imaging could be used to disambiguate these possibilities.

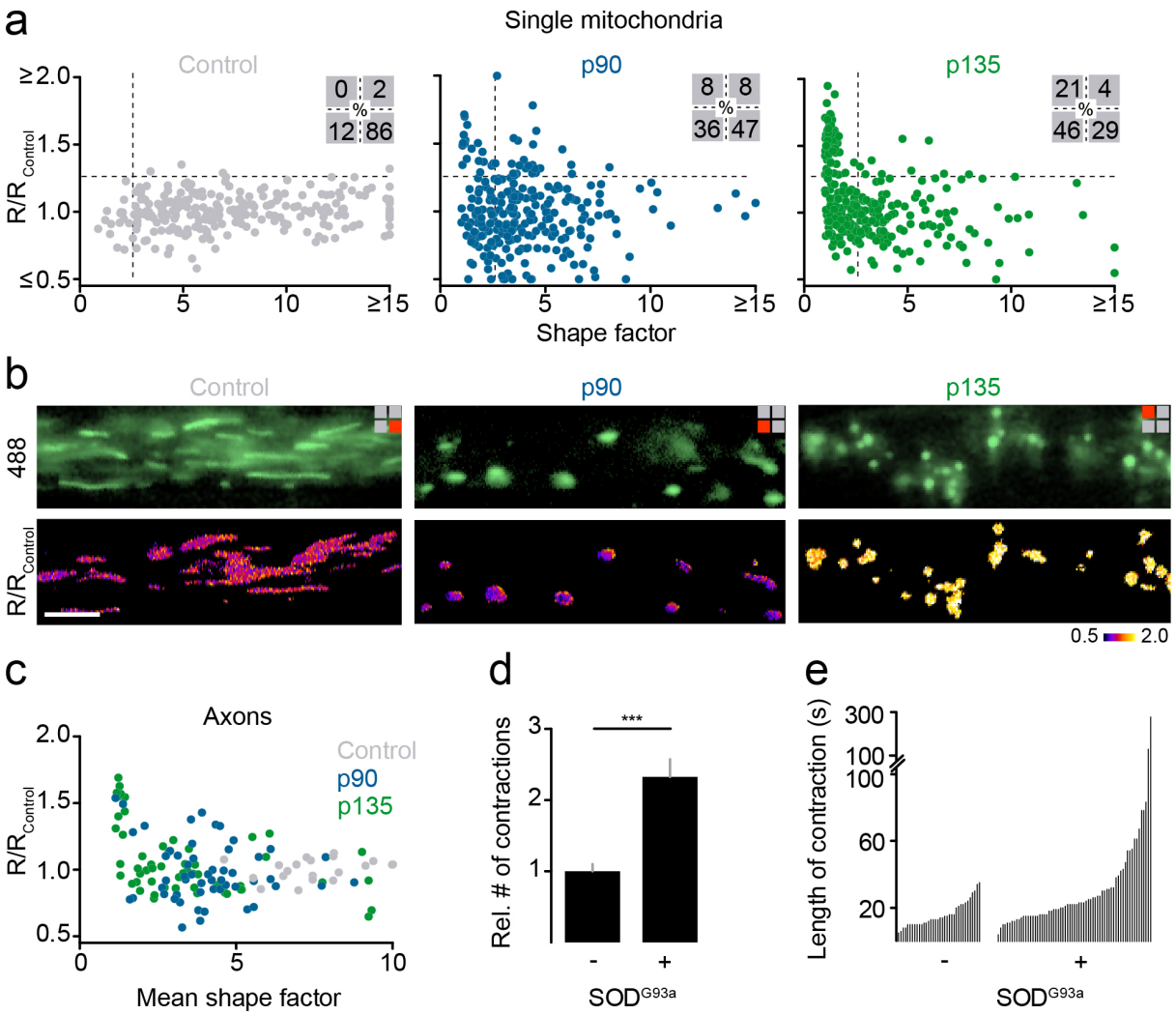

Figure 26: Mitochondrial shape and redox changes in a mouse model of ALS

(a) Quantification of mitochondrial shape factor and probe oxidation ($R/R_{Control}$; normalized to wildtype group) in triangularis sterni explants from SOD^{G93A} x *Thy1*-Grx1-mito-roGFP2 mice at postnatal days 90 and 135. Unaffected littermates served as controls. Points represent single mitochondria (n = 3 mice per group). Insets show percent of all mitochondria in respective quadrants. (**b**) Representative examples of the different mitochondrial shape and oxidation states for different quadrants (as indicated by symbols). (**c**) Average shape factor and probe oxidation of >5 mitochondria for a given axon. Points represent single axons. (**d,e**) Quantification of the frequency and lengths of contractions in SOD^{G93A} animals (p90, p135) and in age-matched, unaffected littermates (n ≥ 12 mice per group). Each vertical line in (**e**) represents the length of a contraction of a single mitochondrion. Scale bar in (**b**) 10 µm.

Redox levels correlate with the axonal fate in EAE

To test the versatility of redox imaging also for chronic inflammatory conditions of the central nervous system (CNS) and to better understand the axonal pathology seen neuroimmunological conditions, I induced EAE with MOG peptide$_{35-55}$ in *Thy1*-mito-Grx1-roGFP2 x *Thy1*-OFP mice. Important features of focal axonal degeneration (FAD), including mitochondrial damage, can be recapitulated by direct application of ROS or RNS to the healthy spinal cord (Nikić et al., 2011). This indicates that mitochondrial damage might be important in the damaging cascade that results in FAD. I correlated the degree of axonal damage and the redox state of mitochondria inside spinal axons during the acute phase of EAE at days 2 and 3 of disease onset (peak of disease). I found that redox levels are increased in diseased axons and correlate with the severity of axonal pathology (stage I *vs.* stage II, Fig. 27 a-b). The increased oxidation of mitochondria persists over time and is not altered on a short timescale of ~5 minutes of sampling. More refined analysis to understand the cascade of mitochondrial and axonal pathology in EAE and MS are ongoing in my host lab, but were not the scope of this thesis.

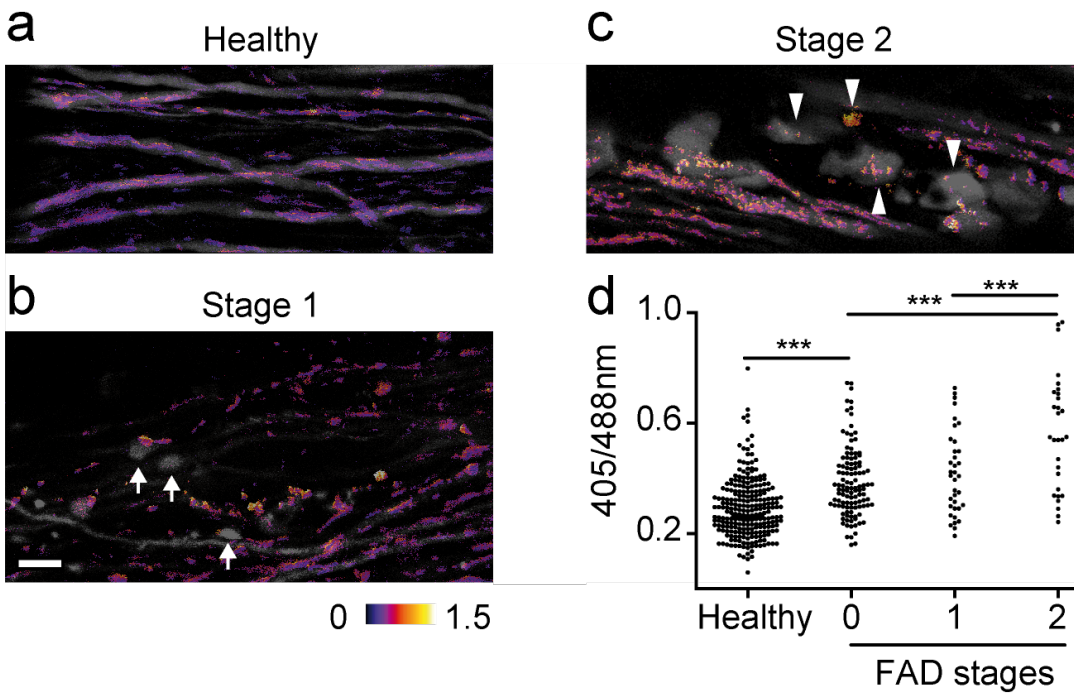

Figure 27: Mitochondrial redox levels correlate with the axonal state in EAE

(**a**) Representative *in vivo* confocal ratiometric image of a healthy control animal and an EAE animal at onset plus two, disease score of 3, (**b,c**) . Axonal stage 1 (axonal swellings indicated by the white arrows, **b**) and stage 2 (axonal fragments, arrowheads in **c**) are depicted. Pseudo-coloring represents oxidative ratio (405/488nm). Axonal morphology is shown as grey image. (**d**) Quantification of single mitochondrial redox levels in EAE, measured *in vivo* in the spinal cord at onset plus two in *Thy1*-mito-Grx1-roGFP2 x *Thy1*-OFP mice. n=33-264 mitochondria, 2-3 mice. ANOVA with Bonferoni *post-hoc* was used for statistical analysis. Scale bar 10 µm.

Mitochondrial redox changes can be measured in the brain

Other locations in the nervous system are of course also of interest for redox imaging. Fig. 28 shows an example of cortical *in vivo* confocal imaging in layer 1 / 2 using a thinned scull preparation (Grutzendler et al., 2011). Comparable results of mitochondrial oxidation and shortening were observed in cortical dendritic mitochondria after induction of a laser lesion. Interestingly, the oxidation spreads in a radial fashion in contrast to the linear spread in spinal axons. This is probably due to the anatomical projections of dendrites in the superficial cortical layers that spread in a radial fasion after ascending from deeper cortical layers (Fig. 28 b).

In a second approach using acute brain slices of *Thy1*-mito-Grx1-roGFP2 mice crossed to *Thy1*-OFP animals, the sensor could be easily imaged in the hippocampus and in neuronal somata from layer 5. By applying an oxidant (10mM diamide) and reducing agent (20mM DTT), the sensor could be reversibly oxidized and reduced (Fig. 28 c,d). One caveat with acute brain slices seems however, that severed neurons, that have been damaged during slicing, exhibit increased redox levels. That is why recordings need to be performed in deeper layers of the slice that have not been damaged during brain slicing. That is why roGFP imaging in brain slices, probably requires 2 photon microscopy (Guzman et al., 2010).

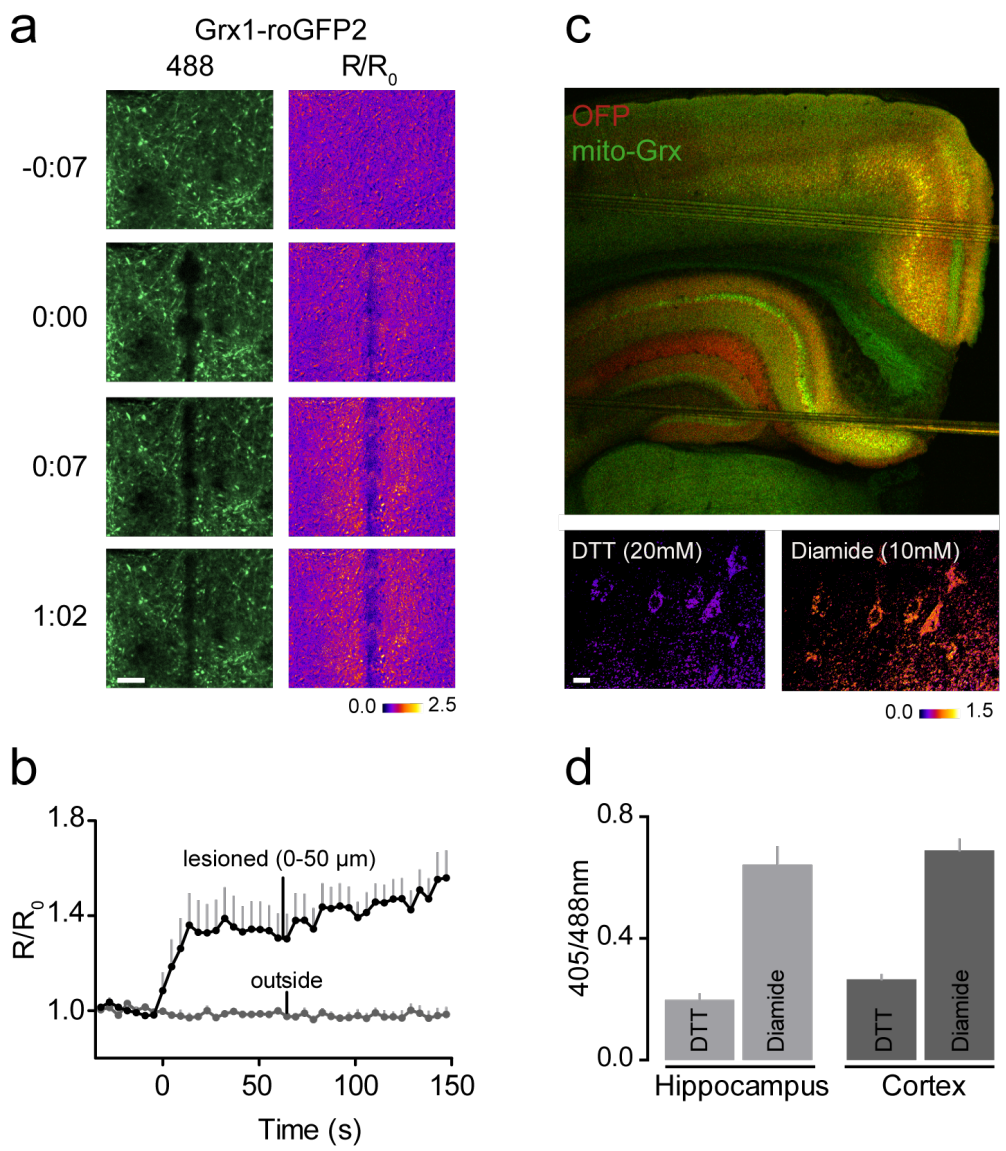

Figure 28: Cortical imaging of mitochondrial shape and redox changes after laser lesion. (**a**)

In vivo time-lapse of mitochondrial changes in the cortex of a *Thy1*-mito-Grx1-roGFP2 mouse after a line-shaped laser lesion (arrow-heads) was induced at time-point 0:00 (time, min:sec). (**b**) Quantification of mitochondrial redox changes after induction of the cortical laser lesion (quantified 0-50 µm away from the lesion site) and outside of the affected area (n = 22 mitochondria, 2 mice). (**c**) Illustration of an acute cortical brain slice of a *Thy1*-OFP x *Thy1*-mito-Grx1-roGFP2 mouse. Magnified images show layer 5 cortical neurons after reduction (with 20mM DTT) and oxidation (with 10mM diamide). The image is distorted by the grid that is used to stabilize the brain slice (**d**) Quantification of the mitochondrial redox potential in the reduced and oxidized state in hippocampal and cortical neurons (n=24 neurons in one representative brain slice). Scale bars, 10 µm.

Discussion

Imaging redox pathways – accomplishments and technical challenges

Reactive oxygen species play important roles in physiological signaling and in pathological processes including neurological disease (Bartosz, 2009; Dröge, 2002; Lin and Beal, 2006). For example, focal axonal degeneration was described in EAE and MS by my host laboratory as a putatively ROS-dependent mechanism of neuroinflammatory axon loss (Nikić et al., 2011). Indeed, it was demonstrated that a process mimicking FAD is initiated by exogenous application of reactive oxygen and nitrogen species. To better understand their origin and effects as well as to assess ROS as a potential therapeutic target, new techniques had to be developed.

However, until recently, the quantification of reactive species *in vivo* was not possible. Research on ROS mainly relied on *in situ* stainings of oxidized lipids and proteins on tissue sections (Haider et al., 2011), as well as on *in vitro* studies in cell culture using synthetic dyes. These dyes have a number of drawbacks, namely chemical unspecificity and poor cellular targeting. The development of redox-sensitive GFPs (roGFP; Dooley et al., 2004; Hanson et al., 2004) and the generation of newer enzyme-coupled versions of this sensor (Gutscher et al., 2008; 2009) were therefore major steps forward towards a better understanding of redox biology (Herrmann and Dick, 2012). The goal of my thesis was to transfer these novel fluorescent sensors to *in vivo* applications in mice and to use them in the study of EAE and other neurological disease models.

Different redox sensors were first tested in cell culture, before transgenic *Thy1*-mito-Grx1-roGFP2 mice were generated. These novel mice were screened for suitable expression patterns, before mitochondrial redox measurements under physiological conditions were performed. Here, we made the surprising finding of spontaneous redox bursts occurring during mitochondrial contractions (for a detailed discussion, see following paragraph). Next we turned to various disease models (including ALS and nerve injury models) to investigate pathological redox signals.

The detailed dissection of redox pathways during contractions and in disease models turned out to be more complex (and time-consuming) than expected. To better define

the nature of redox signals, additional sensors were established to read out underlying pathways. That is why the initial goal of defining the role of ROS during axonal pathology in EAE was eventually not met during the time of my thesis and is now being pursued by my host labs in a follow-up project. I established, however, a number of tools that should facilitate the dissection of redox pathways in EAE.

A number of challenges arose during the development of redox imaging:

1. The approach to generate transgenic mouse lines expressing roGFP2 was not as straightforward as assumed. We generated three transgenic lines: *Thy1*-mito-Grx1-roGFP2 turned out to be successful. This transgenic line is the mainstay of my thesis and future work in EAE. *Thy1*-mito-roGFP2-Orp1 yielded only insufficient expression levels not suitable for *in vivo* imaging. *Thy1*-Grx1-roGFP2, a cytoplasmic version of the redox sensor, did not show any expression in the founder lines, even though the transgene was inserted in the genome as proven by PCR.

The generation, screening and cross-breeding of transgenic lines is quite time-consuming (~6 months). That is why we tried to establish viral approaches for faster expression of transgenes. Lentiviral vectors (Dittgen et al., 2004) yielded only insufficient expression levels and caused toxicity. Adeno-associtated viruses turned out to be more suitable for transgene expression in my hands. Their expression is relatively fast within 10-14 days post injection and I could obtain robust expression of various sensors in triangularis sterni explants by cervical spinal cord injections of virus particles. Injections into the dorsal root ganglion to express transgenes in the dorsal funiculus for *in vivo* spinal cord imaging would be a nice extension of this work, which however was not pursued in my PhD work.

2. *In vivo* imaging of Grx1-roGFP2 is difficult with conventional 2-photon microscopy because the sensor requires two-wavelength excitation for ratiometric measurements. This can be done ideally with two 2-photon lasers and line-sequential scanning. Such a setup was not available to me. The alternative of tuning the laser between 800 nm and 940 nm is time consuming (~2 sec) and allows only frame-sequential scanning. This is problematic as movement artifacts occur, especially in spinal imaging, which lead to

shifts in the image plane of the two channels. That is why I turned to confocal microscopy to use line-sequential scanning (~4 msec per line). With the confocal approach, shifts of the imaging plane between channels are minimal. I obtained a time resolution of ~0.2 Hz which is sufficient to detect the relatively slow and long-lasting oxidative changes following axotomy. Confocal imaging however has known disadvantages for *in vivo* imaging such as less depth penetration and increased out-of-focus phototoxicity and photo-bleaching, compared to 2-photon microscopy. That is why we tried to establish an emission ratiometric sensor by crossing *Thy1*-mito-Grx1-roGFP2 to *Thy1*-mito-TagRFP-H mice. This approach might allow 2-photon emission ratiometric imaging by normalizing the redox sensitive Grx1-roGFP2 signal by the redox insensitive TagRFP signal. Proof-of-principle experiments for this “novel” redox sensor are on-going.

3. The development of a spinal cord injury model took some time. Finally, I established a laser lesion model, that yields very “clean”, reproducible axonal transections. Classical models of contusion injury, which certainly mimic the clinical condition better, have the disadvantage that it takes time until imaging can be started after lesion induction. The laser lesion model allowed the integration of the lesion induction into the imaging paradigm, so that redox changes that occur immediately after axonal transections can be monitored.

All these are reasons why I only performed proof of principle experiments in the EAE model and concentrated on less complex disease models (laser lesion). Also, we made the unexpected observation of mitochondrial contractions, which I decided to persue in more depth.
Alltogether, the approach to measure mitochondrial redox signals using *Thy1*-mito-Grx1-roGFP2 mice and to further dissect the underlying signaling cascades using viral, genetic and pharmacological apporoaches was successful. Thus, I could define two distinct redox pathways occurring during reversible contractions and in permanent mitochondrial rounding.

Mitochondrial contractions are a marker of mitochondrial stress

Mitochondrial contractions were a serendipitous finding. They were already observed in *Thy1*-mito-CFP mice (Misgeld et al., 2007a) but not further investigated (unpublished observation by T. Misgeld and M. Kerschensteiner). I hypothesized that this phenomenon could be of potential interest for physiological and pathological conditions even though their significance was not clear. Over the course of my thesis I generated evidence that mitochondrial contractions are indeed linked to oxidative and cellular stress and that their frequency and length increases during pathological states.

By making use of various optical sensors (mito-Grx1-roGFP2, mito-GCaMP-3, mito-RGECO-1, mito-SypHer, Tn-XXL, TMRM) as well as genetic and pharmacological manipulations, I could define a mechanistic framework for mitochondrial contractions (Fig.29 a). There are a number of reports of spontaneous mitochondrial signals in the literature that were dubbed "potential fluctuations", "pulses", "superoxide bursts" or "oscillations" (Buckman and Reynolds, 2001; Chalmers and McCarron, 2008; Kurz et al., 2010; Schwarzlander et al., 2012; Wang et al., 2008). These spontaneous mitochondrial signals were described in plants, cardiomyoctes, smooth muscle cells and neurons. Most of these reports relied on mitochondrial membrane potential measurements and are in line with the reversible mitochondrial membrane depolarization that I describe. We decided to introduce the term "mitochondrial contraction" because the morphological shortening and re-elongation of the organelle is quite striking. Other reports did not describe morphological changes, possibly because mitochondria cannot be observed as single entities in other preparations as easily. Also, when TMRM is the only label, mitochondria loose their fluorescence upon membrane potential drop, so the morphology cannot be judged. In axons, mitochondria are sparse and many resting organelles can be visualized over hours. This facilitates time-lapse observations. Mitochondria however are quite motile in plants or very dense in cardiomyocytes, which makes single-organelle observations more difficult. Other reports did not describe an oxidative shift but rather an influx of calcium during the pulse (Schwarzlander et al., 2012; Wang et al., 2013). Blocking the mitochondrial transition pore, abrogated these calcium-dependent mitochondrial dynamics (Wang et al., 2008). This is in contrast to mitochondrial contractions, which were both calcium and transition-pore independent.

The detected calcium signal during contractions using mito-RGECO1 was bellow 2% of the absolute signal amplitude of the sensor, so we excluded a major calcium influx during the contraction.

Given the influence of oxidative stress and neuronal activity on contraction frequency, contractions might be linked to different functional states of mitochondria that have been described to influence mitochondrial morphology (Perkins and Ellisman, 2011; Scalettar et al., 1991). It is well conceivable that contractions occur when mitochondria undergo a conversion of their functional state and membrane re-organisation might help to change membrane-to-surface area to meet functional requirements. At this point the function of contractions is not entirely clear. We suggest a “fuse-like” mechanism due to the long-lasting depolarization and acidification we observed. This indicates that mitochondria produce less ATP and become temporary “inactive” during the contraction. One hypothesis would be that mitochondria with increased redox states contract to allow recovery from oxidative stress by downregulating their activity. Further functional measurements to directly measure ROS like H_2O_2 would be necessary to prove this idea. Additionally, probing possible upstream and downstream effects using *e.g.* sodium, potassium or ATP-sensors would be important to mechanistically understand the origins and effects of contractions. A cation influx like Na^+ or K^+ could explain the observed membrane depolarization. The underlying mechanism causing the morphological change is also not clear. Possible explanations include a redox sensitive pore that, upon opening or closure, leads to an ionic flux and passive osmotic swelling. This could result in a reorganization of the mitochondrial matrix (for which the pearl-on-string morphology of contracting mitochondria is suggestive). Unfortunatly, superresolution or electron microscopy would be necessary to fully resolve the mitochondrial inner and outer membrane. These techniques are unfortunately not compatible with time-resolved, dynamic measurements of complex tissues.

Altogether, it is very likely that the different phenomena that are described in the literature share common mechanisms and probably functions, but have evolved in different ways to meet cell-type specific requirements.

Permanent mitochondrial rounding occurs in spinal cord injury and ALS

Next to the investigation of mitochondrial contractions, I focused on redox signals that occur in neurological disase models. I established a laser axotomy paradigm using a femto-second, high energy Ti:sapphire laser. This injury model proved to be ideal due to its excellent reproducibility and the feasibility of imaging different stages of mitochondrial and axonal pathology. This includes mitochondrial contractions, rounding and fragmentation (fission), as well as acute axonal degeneration. In contrast to reversible contractions, which go along with transient calcium-independent redox signals, the mitochondrial pathology seen after axotomy is characterized by long-lasting redox perturbations and permanent, calcium-dependent rounding (Fig.29 b). This is in line with previous reports, which described calcium-influx and arrest of mitochondrial transport after axotomy (Avery et al., 2012) as well as the protection of severed axons from degeneration by the depletion of extracellular calcium (George et al., 1995).

Similarly, mitochondrial oxidation and shortening was observed in late stages of the ALS model (p90 and 120). As the pathology develops over weeks and months and measurements were performed in acute triangularis sterni explants, it was not possible to dissect the exact cascade of mitochondrial pathology. Presumably, mitochondrial undergo irreversible contractions but also increased fission might occur that leads to the shortening. Contraction frequency and contraction length was increased in triangularis sterni explants – all contractions were however reversible. The functional consequence of mitochondrial shortening and oxidation remains uncertain. It would be interesting to use the multiparametric imaging approach (described in the next paragraph) in the ALS model to better understand *e.g.* the role of cytoplasmic and mitochondrial calcium dynamics. As a note of caution, recent publications are suggestive that the mitochondrial pathology in ALS models might be rather a bystander effect, than a driver of neuronal pathology (Marinkovic et al., 2012; Parone et al., 2013).

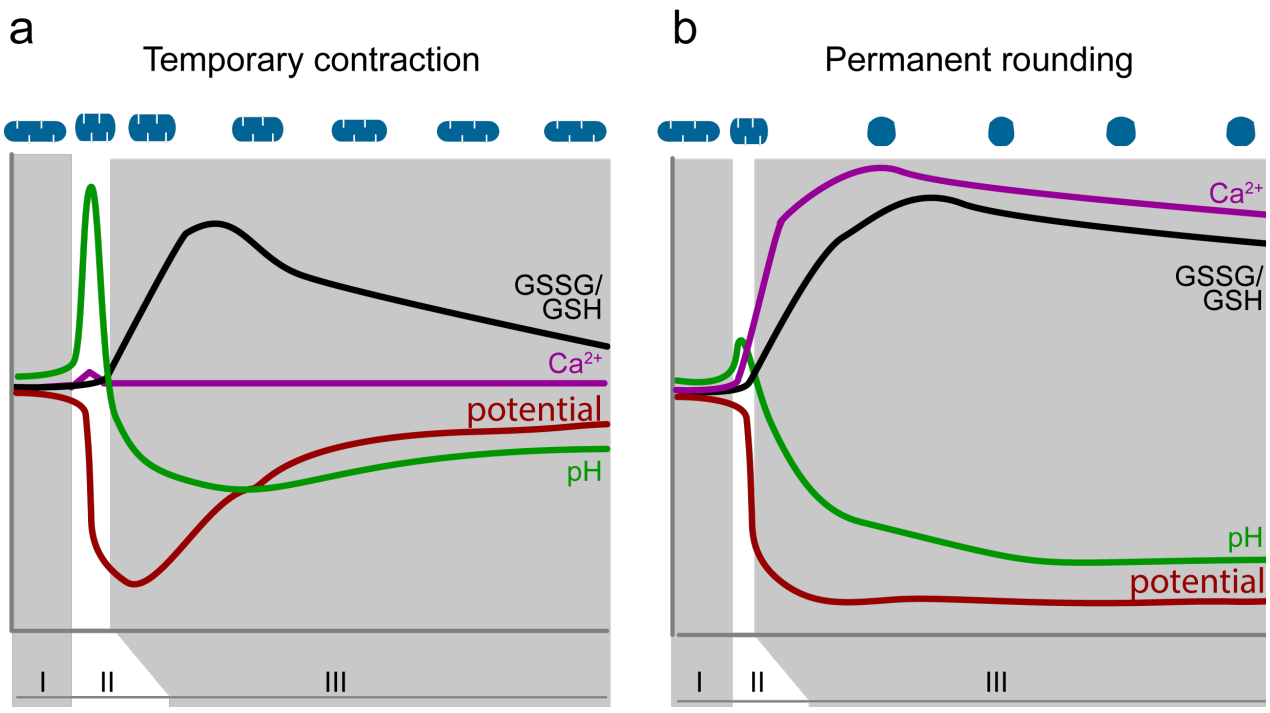

Figure 29: Schematic comparison of physiological mitochondrial contractions and pathological mitochondrial rounding/fragmentation after axotomy

Mitochondrial glutathione potential, calcium level, inner membrane potential (ψ) and matrix pH dynamics are shown as schematic traces. Phase I represents the period before the contraction (**a**) or the axotomy (**b**). Phase II indicates the event itself (contraction/axotomy) and phase III is the time after the contraction/axotomy. Note the reversible nature of contractions *vs.* the permanent rounding following the axotomy.

Opto-bioenergetics

By combining various sensors and pharmacological and genetic manipulations, mitochondrial contractions and permanent rounding could be clearly differentiated with their different causes and mechanisms. Altogether this establishes a multi-parametric imaging toolkit to define pathways implicated in physiology and pathology. As my investigations involved mainly mitochondria and their role in redox signaling, one can consider this as a first step towards “opto-bioenergetics”. This is analogous to the fields of optophysiology and optogenetics (Zhang et al., 2007) - even though optical actuators to regulate mitochondrial function are largely still missing (Bulina et al., 2005; Shu et al., 2011). Using the different sensors described above one can read out important

mitochondrial functions such as redox state, calcium level, proton gradient and inner membrane potential. Additional readouts to measure mitochondrial ATP and H_2O_2 levels (Gutscher et al., 2009; Imamura et al., 2009) were tested but results were inconclusive (data not shown).

As other biosensors, such as genetically encoded calcium sensors (GECIs), are increasingly spanning the spectral palette (Akerboom et al., 2013; Grienberger and Konnerth, 2012), it can be expected that the combination of different sensor modalities will synergistically increase the power of imaging to better reveal the intricate interplay between different signaling pathways, such as redox and calcium signals. This will in particular allow co-visualizing signals in different compartments and organelles. Especially, the viral techniques I describe in my thesis are very versatile. The approach can be extended not only to other cell types, such as oligodendrocytes or astrocytes, but also to involve knockdown or overexpression of genes in motor or sensory axons.

The investigation of redox signaling and its analogy to calcium signaling

The generation of the *Thy1*-mito-Grx1-roGFP2 mice proved to be a useful tool. These mice allowed the dissection of two different redox signals implicated in mitochondrial physiology (reversible contractions) and pathology (permanent rounding). Redox biology is an emerging research field. Until recently tools were missing to investigate redox changes and their effects *in vivo*. But this has changed with the development of redox-sensitive GFP (Dooley et al., 2004; Hanson et al., 2004) and the recent generation of enzyme-coupled roGFP variants (Gutscher et al., 2008; 2009). These novel fluorescent sensors allow the investigation of defined redox pairs overcoming many of the problems associated with redox-sensitive dyes that were the only option for *in vivo* recordings of redox signals before (Meyer and Dick, 2010). It can be postulated that redox signaling might be just as important as calcium or kinase signaling in regulating cellular processes and that now the necessary tools are becoming available to push the field of redox biology forward into the *in vivo* realm (Herrmann and Dick, 2012). Grx1-roGFP2 senses the ratio of reduced and oxidized glutathione (GSH/GSSG). This defined redox pair does not reflect the entire oxidative state of a given compartment because additional redox

pairs exist, such as exposed cystein residues in proteins or thioredoxin. Hence, it is possible that under specific conditions, some redox systems are selectively modified without affecting others (Albrecht et al., 2011; Chouchani et al., 2013). Additionally, the equilibrium of the different redox pairs does not only depend on reactive species that are present, but also on the concentration of the reducing enzymes and necessary co-factors like NADPH. Indeed, it has been shown previously that different redox pairs are not necessarily in the same state of oxidation (Albrecht et al., 2011). This adds another layer of complexity to the investigation of redox signals. Also, it is important to keep in mind that Grx1-roGFP2 does not directly measure ROS, but rather the glutathione redox potential (E_{GSH}). We anticipated this limitation and therefore tried to develop roGFP2-Orp1 as a parallel *in vivo* tool. Unfortunately, this approach to measure H_2O_2 directly was inconclusive due to the low expression levels of the sensor. As Orp1 is a protein from yeast it can be speculated that for unknown reasons it is not efficiently expressed in mammalian neurons, even though its expression in other mouse tissues is unproblematic (T. Dick, personal communication).

For the future it would be desirable to develop redox sensors with larger signal amplitudes and to expand their spectral palette to enable co-assaying different redox pairs in parallel. If additional sensors, specific for different redox pairs, became available, a true multi-parametric assessment of a cell`s "redox state" would be possible, as well as a quantitative description of "ROS stress". H_2O_2 appears still to be one of the prime targets for a true ROS sensor. But also superoxide, the hydroxyl radical and peroxynitrite seem interesting and important targets. All of them are more reactive than H_2O_2 and are probably responsible for most of the detrimental effects of ROS. It is unfortunate that the published cpYFP-based sensors, including HyPer, are very pH-sensitive. It is therefore controversial whether these sensors are truly measuring O_2^- and H_2O_2, especially in mitochondria, where drastic pH changes are common and could “contaminate” the measured "redox" signal. (Belousov et al., 2006; Schwarzländer et al., 2011; 2012; Wang et al., 2008; Wei-LaPierre et al., 2013).

Sensitivity to pH is not only an issue for cpYFP-based probes but also GFP variants like GCaMPs suffer from this problem. When measuring neuronal activity, pH sensitivity is not seen as a drawback for a probe because one assumes that no major pH shifts occur

during the recording. Given the dynamic pH changes that characterize different metabolic states of mitochondria and their relative alkaline milieu compared to the cytoplasm and other organelles, pH sensitivity can be a confounding factor that one has to control for. Recently, newer GCaMP variants like RGECO-1 were engineered to be less pH sensitive. In my hand RGECO-1 was indeed markedly less pH sensitive than GCaMP-3, which is in line with the reported literature (Akerboom et al., 2013).

Calcium overload as a therapeutic target for mitochondrial and axonal pathology

Blocking the axotomy-induced calcium elevation completely prevented mitochondrial and axonal pathology after axotomy. This striking effect was experimentally achieved by depleting calcium from the extracellular space (George et al., 1995). Knockdown of cyclophilin D, which is known to improve the calcium-buffering capacity of mitochondria (Forte et al., 2007; Fransen, 2012; Schinzel et al., 2005), also mitigated the mitochondrial pathology in the laser lesion model. This corroborates the importance of calcium in the damaging cascade. Probably, mitochondria that do not undergo transition-pore opening maintain their inner membrane potential and the ability to produce ATP. This might in addition have a neuroprotective effect.

Calcium, of course, has multi-fold roles (*e.g.* in the clotting cascade, during action potential conduction and intracellular signaling) and depleting calcium is obviously not a valid therapeutic option. Even in the experimental situation, calcium depletion led to an exacerbation of bleeding from the surgical site. Therefore, more fine-tailored pharmacological manipulations of calcium levels are needed. Unfortunately, there are many possible intra- and extracellular sources for calcium and thus candidates for pharmacological interventions. It was not the scope of this thesis to do a more systematic genetic or drug screen of calcium modulation. Given the results from my calcium-depletion experiments, it can be hypothesized that modifying calcium entry into axons after injury would be a potential target for therapy. Indeed, this possibility is currently under investigation in my host laboratories.

In the axotomy paradigm, calcium is upstream of the observed redox and shape changes. The significance of the spreading oxidation is not clear. Scavenging ROS or blocking redox changes did not prevent mitochondrial shape changes. Nevertheless, it can be postulated that the long-lasting mitochondrial oxidation, observed over the entire period of investigation (4 hours), has very likely detrimental effects for the axon itself and possibly for the neighboring tissue as well. Damage could be due to ROS generation itself but also due to malfunction of the electron transport chain and consecutive ATP-depletion of the axon (O'Donnell et al., 2013). Measuring ROS levels directly, as well as ATP levels (Berg et al., 2009; Imamura et al., 2009) would be an interesting extension of this work. Especially, whether diminishing ATP levels are a predictor for the development of local axonal swellings in FAD or the extent of AAD would be an important question. In the axotomy experiments abrupt gradients of calcium levels and mitochondrial shape alterations were detectable ~100 µm from the injury site. It would be informative to determine whether ATP depletion is confined to the same compartment. Not much is known about the local ATP distribution within axons, but it can be hypothesized that an ATP threshold exists that is necessary to promote the morphological and functional integrity of the neuron. Likewise studying a potential signaling role of ROS, *e.g.* in attracting leukocytes to the injury site or in priming regenerative processes, as proposed in zebrafish and xenopus would be worth studying (Love et al., 2013; Niethammer et al., 2009). The developed imaging tools together with pharmacological and genetic manipulations allow addressing such questions.

Investigating redox changes and their significance in EAE and beyond

As stated above, ROS production from extrinsic (inflammatory cells) and intrinsic sources (OXPHOS) are most likely a driving force for the neuronal damage seen in a number of neurological diseases, including MS (Nikić et al., 2011). This was a central motivation for my work. It will be a primary goal of subsequent projects to apply the developed techniques to neuroinflammatory models. EAE is inherently more complex than the acute laser lesion model because different cells types from the innate and adaptive immune system contribute to the injury of grey and white matter. A main challenge in understanding the mitochondrial contribution to neuronal pathology will be

to decipher at which stage of the disease mitochondrial ROS production occurs. ROS production could be both a cause, as well as a consequence of axonal pathology. Whether neuronal calcium increases are up- or downstream of the mitochondrial pathology can be addressed with the developed techniques. Similarly, the contribution of inflammatory cells to the ROS burden can be studies by the generation of new transgenic or viral approaches to express the molecular sensors in inflammatory cells. Of course, it is also conceivable to express these sensors in other resident cells that are important for the disease process, such as oligodendrocytes or astrocytes. Overall the approach of multi-parametric imaging promises to help deciphering the sequence of damaging events. This might be the first step to identify new therapeutic targets in EAE/MS and possibly other neurological diseases.

Acknowledgements

First, I would like to thank my advisors, Prof. Thomas Misgeld (TUM) and Prof. Martin Kerschensteiner (LMU) for the opportunity to work in their laboratories. I am grateful for their continuous support throughout the project. I really appreciated the stimulating environment, the discussions and help to set up experiments, analyze data and to overcome obstacles. The atmosphere of intellectual freedom as well as the opportunity to pursue own ideas was great. Throughout my time in the lab I got to know a very analytical and rigorous way of conducting science. I truly learned a lot during these years and I enjoyed being a part of their laboratories.

I am indebted to all members of the Misgeld and Kerschensteiner laboratory for their help, the discussions, the positive and friendly atmosphere and the numerous “Football table timeouts.”

Especially during the manuscript revision a number of people helped to push the project forward and the progress that we made would not have been possible without the extraordinary efforts of a number of people. I would like to thank especially Franz Pfister, Peter Bradley, Petar Marinković, Anja Schmalz, Monika Brill, Phil Wiliams, Leanne Godinho, Florence Bareyre, Geraldine Heitmann and Barbara Plomer.

I would also like to thank Dietmar Beyer, Felix Beyer, Kristina Wullimann and Christine Karrer for their great technical support.

I also thank Dana Matzek, Manuela Budak, Nebi Budak, Ljiljana Marinković and Petra Apostolopoulos for animal husbandry.

Finally, I simply cannot thank enough my family and my wife Laura for their loving support.

Publications resulting from the PhD

1) **Breckwoldt MO**, Pfister F, Bradley, PM, Marinković P, Williams PR, Brill MS, Plomer B, Schmalz, A, St. Clair DK, Naumann R, Griesbeck O, Schwarzländer M, Godinho L, Bareyre FM, Dick TP, Kerschensteiner M* and Misgeld T*, Muti-parametric optical analysis of redox signals during neuronal physiology and pathology *in vivo*. Nature Medicine, in press (* equal contribution)

2) Plucińska G, Marinković P, **Breckwoldt, MO**, Misgeld T. Studying dynamics of neuronal mitochondria *in vivo.* (in preparation)

3) Fujikawa Y, Sobotta M, Kuntz G, Diaz MB, **Breckwoldt MO**, Herzig S, Müller-Decker K, Misgeld T, Kerschensteiner M and Dick TP, Histological redox imaging with genetically encoded probes. (in preparation)

Conference contributions and presentations

1) Mitochondrial dynamics in health and disease, Sardinia, Italy, 9/2011 (poster)
2) German Neuroimmunology Meeting, Seeon, Germany 2/2012 (oral presentation)
3) Neurology Department, Göttingen 6/2012 (invited talk)
4) German National Academic Foundation, fellows conference, Berlin, Frankfurt, 2011, 2012 (oral presentation)
5) Gertrud Reemtsma Foundation, Cologne, 2011, 2012 (oral presentation)
6) Interact PhD student conference, Munich, 5/2013 (oral presentation)

Curriculum Vitae

not included in the electronic version for privacy protection

References

Abou-Sleiman, P.M., Muqit, M.M.K., and Wood, N.W. (2006). Expanding insights of mitochondrial dysfunction in Parkinson's disease. Nat Rev Neurosci *7*, 207–219.

Akerboom, J., Chen, T.W., Wardill, T.J., Tian, L., Marvin, J.S., Mutlu, S., Calderon, N.C., Esposti, F., Borghuis, B.G., Sun, X.R., et al. (2012). Optimization of a GCaMP calcium indicator for neural activity imaging. Journal of Neuroscience *32*, 13819–13840.

Akerboom, J., Carreras Calderón, N., Tian, L., Wabnig, S., Prigge, M., Tolö, J., Gordus, A., Orger, M.B., Severi, K.E., Macklin, J.J., et al. (2013). Genetically encoded calcium indicators for multi-color neural activity imaging and combination with optogenetics. Front Mol Neurosci *6*, 1–29.

Al-Mehdi, A.B., Pastukh, V.M., Swiger, B.M., Reed, D.J., Patel, M.R., Bardwell, G.C., Pastukh, V.V., Alexeyev, M.F., and Gillespie, M.N. (2012). Perinuclear mitochondrial clustering creates an oxidant-rich nuclear domain required for hypoxia-induced transcription. Science Signaling *5*, 1–10.

Albrecht, S.C., Barata, A.G., Großhans, J., Teleman, A.A., and Dick, T.P. (2011). In vivo mapping of hydrogen peroxide and oxidized glutathione reveals chemical and regional specificity of redox homeostasis. Cell Metabolism *14*, 819–829.

Avery, M.A., Rooney, T.M., Pandya, J.D., Wishart, T.M., Gillingwater, T.H., Geddes, J.W., Sullivan, P.G., and Freeman, M.R. (2012). WldS prevents axon degeneration through increased mitochondrial flux and enhanced mitochondrial Ca^{2+} buffering. Current Biology *22*, 596–600.

Babior, B.M. (1984). The respiratory burst of phagocytes. J. Clin. Invest. *73*, 599–601.

Ballinger, S.W. (2005). Mitochondrial dysfunction in cardiovascular disease. Free Radical Biology and Medicine *38*, 1278–1296.

Bareyre, F.M. (2008). Neuronal repair and replacement in spinal cord injury. Journal of the Neurological Sciences *265*, 63–72.

Bartosz, G. (2009). Reactive oxygen species: Destroyers or messengers? Biochemical Pharmacology *77*, 1303–1315.

Basso, D.M., Beattie, M.S., and Bresnahan, J.C. (1995). A sensitive and reliable locomotor rating scale for open field testing in rats. J. Neurotrauma *12*, 1–21.

Batlevi, Y., and La Spada, A.R. (2011). Mitochondrial autophagy in neural function, neurodegenerative disease, neuron cell death, and aging. Neurobiology of Disease *43*, 46–51.

Belousov, V.V., Fradkov, A.F., Lukyanov, K.A., Staroverov, D.B., Shakhbazov, K.S., Terskikh, A.V., and Lukyanov, S. (2006). Genetically encoded fluorescent indicator for intracellular hydrogen peroxide. Nat Meth *3*, 281–286.

Berg, J., Hung, Y.P., and Yellen, G. (2009). A genetically encoded fluorescent reporter of ATP:ADP ratio. Nat Meth *6*, 161–166.

Boscolo, A., Milanovic, D., Starr, J.A., Sanchez, V., Oklopcic, A., Moy, L., Ori C, C., Erisir, A., and Jevtovic-Todorovic, V. (2013). Early exposure to general anesthesia disturbs mitochondrial fission and fusion in the developing rat brain. Anesthesiology *110*, 57–52.

Bratic, A., and Larsson, N.-G. (2013). The role of mitochondria in aging. J. Clin. Invest. *123*, 951–957.

Buckman, J.F., and Reynolds, I.J. (2001). Spontaneous changes in mitochondrial membrane potential in cultured neurons. Journal of Neuroscience *21*, 5054–5065.

Bulina, M.E., Chudakov, D.M., Britanova, O.V., Yanushevich, Y.G., Staroverov, D.B., Chepurnykh, T.V., Merzlyak, E.M., Shkrob, M.A., Lukyanov, S., and Lukyanov, K.A. (2005). A genetically encoded photosensitizer. Nat Biotechnol *24*, 95–99.

Charcot, J. (1868). Histologie de la sclerose en plaques. Gazette des hopitaux*, 41*, 554–5

Chalmers, S., and McCarron, J.G. (2008). The mitochondrial membrane potential and Ca^{2+} oscillations in smooth muscle. Journal of Cell Science *121*, 75–85.

Chandrasekaran, K., Hazelton, J.L., Wang, Y., Fiskum, G., and Kristian, T. (2006). Neuron-specific conditional expression of a mitochondrially targeted fluorescent protein in mice. Journal of Neuroscience *26*, 13123–13127.

Chang, K.T., Niescier, R.F., and Min, K.-T. (2011). Mitochondrial matrix Ca^{2+} as an intrinsic signal regulating mitochondrial motility in axons. Proc. Natl. Acad. Sci. U.S.A. *108*, 15456–15461.

Chazotte, B. (2011). Labeling mitochondria with TMRM or TMRE. Cold Spring Harb Protoc *2011*, 895–897.

Chen, H., and Chan, D.C. (2009). Mitochondrial dynamics-fusion, fission, movement, and mitophagy-in neurodegenerative diseases. Human Molecular Genetics *18*, 169–176.

Chen, Y., and Dorn, G.W. (2013). PINK1-phosphorylated mitofusin 2 is a parkin receptor for culling damaged mitochondria. Science *340*, 471–475.

Choi, H.B., Gordon, G.R.J., Zhou, N., Tai, C., Rungta, R.L., Martinez, J., Milner, T.A., Ryu, J.K., McLarnon, J.G., Tresguerres, M., et al. (2012). Metabolic communication between astrocytes and neurons via bicarbonate-responsive soluble adenylyl cyclase. Neuron *75*, 1094–1104.

Chouchani, E.T., Methner, C., Nadtochiy, S.M., Logan, A., Pell, V.R., Ding, S., James, A.M., eacute, H.M.C., Reinhold, J., Lilley, K.S., et al. (2013). Cardioprotection by S-nitrosation of a cysteine switch on mitochondrial complex I. Nat Med *19*, 753–759.

Corrado, M., Scorrano, L., and Campello, S. (2012). Mitochondrial dynamics in cancer and neurodegenerative and neuroinflammatory diseases. International Journal of Cell Biology *2012*, 1–13.

Cowan, W.M., Harter, D.H., and Kandel, E.R. (2000). The emergence of modern neuroscience: some implications for neurology and psychiatry. Annu. Rev. Neurosci. *23*, 343–391.

Direnberger, S., Mues, M., Micale, V., Wotjak, C.T., Dietzel, S., Schubert, M., Scharr, A., Hassan, S., Wahl-Schott, C., Biel, M., et al. (2012). Biocompatibility of a genetically encoded calcium indicator in a transgenic mouse model. Nature Communications *3*, 1031–10.

Dittgen, T., Nimmerjahn, A., Komai, S., Licznerski, P., Waters, J., Margrie, T.W., Helmchen, F., Denk, W., Brecht, M., and Osten, P. (2004). Lentivirus-based genetic manipulations of cortical neurons and their optical and electrophysiological monitoring in vivo. Proc. Natl. Acad. Sci. U.S.A. *101*, 18206–18211.

Dooley, C.T., Dore, T.M., Hanson, G.T., Jackson, W.C., Remington, S.J., and Tsien, R.Y. (2004). Imaging dynamic redox changes in mammalian cells with green fluorescent protein indicators. J. Biol. Chem. *279*, 22284–22293.

Drago, I., De Stefani, D., Rizzuto, R., and Pozzan, T. (2012). Mitochondrial Ca^{2+} uptake contributes to buffering cytoplasmic Ca^{2+} peaks in cardiomyocytes. Proc. Natl. Acad. Sci. U.S.A. *109*, 12986–12991.

Dröge, W. (2002). Free radicals in the physiological control of cell function. Physiol. Rev. *82*, 47–95.

Dutta, R., McDonough, J., Yin, X., Peterson, J., Chang, A., Torres, T., Gudz, T., Macklin, W.B., Lewis, D.A., Fox, R.J., et al. (2006). Mitochondrial dysfunction as a cause of axonal degeneration in multiple sclerosis patients. Ann Neurol. *59*, 478–489.

Echtay, K.S., Pakay, J.L., Esteves, T.C., and Brand, M.D. (2005). Hydroxynonenal and uncoupling proteins: a model for protection against oxidative damage. BioFactors *24*, 119–130.

Ertürk, A., Mauch, C.P., Hellal, F., Förstner, F., Keck, T., Becker, K., Jährling, N., Steffens, H., Richter, M., Hübener, M., et al. (2011). Three-dimensional imaging of the unsectioned adult spinal cord to assess axon regeneration and glial responses after injury. Nat Med *18*, 166–171.

Esterbauer, H., Schaur, R.J., and Zollner, H. (1991). Chemistry and biochemistry of 4-hydroxynonenal, malonaldehyde and related aldehydes. Free Radical Biology and Medicine *11*, 81–128.

Fatokun, A.A., Stone, T.W., and Smith, R.A. (2008). Oxidative stress in neurodegeneration and available means of protection. Front. Biosci. *13*, 3288–3311.

Feng, G., Mellor, R.H., Bernstein, M., Keller-Peck, C., Nguyen, Q.T., Wallace, M., Nerbonne, J.M., Lichtman, J.W., and Sanes, J.R. (2000). Imaging neuronal subsets in transgenic mice expressing multiple spectral variants of GFP. Neuron *28*, 41–51.

Filli, L., and Schwab, M.E. (2012). The rocky road to translation in spinal cord repair. Ann Neurol. *72*, 491–501.

Forte, M., Gold, B.G., Marracci, G., Chaudhary, P., Basso, E., Johnsen, D., Yu, X., Fowlkes, J., Rahder, M., Stem, K., et al. (2007). Cyclophilin D inactivation protects axons in experimental autoimmune encephalomyelitis, an animal model of multiple sclerosis. Proc. Natl. Acad. Sci. U.S.A. *104*, 7558–7563.

Fransen, M. (2012). Cyclophilin D: a therapeutic target to counteract reactive oxygen species-mediated damage in neurodegenerative disease? Brain *135*, 3525–3526.

Friese, M.A., Craner, M.J., Etzensperger, R., Vergo, S., Wemmie, J.A., Welsh, M.J., Vincent, A., and Fugger, L. (2007). Acid-sensing ion channel-1 contributes to axonal degeneration in autoimmune inflammation of the central nervous system. Nat Med *13*, 1483–1489.

Frohman, E.M., Racke, M.K., and Raine, C.S. (2006). Multiple sclerosis—the plaque and its pathogenesis. New England Journal of Medicine *354*, 942–955.

George, E.B., Glass, J.D., and Griffin, J.W. (1995). Axotomy-induced axonal degeneration is mediated by calcium influx through ion-specific channels. J. Neurosci. *15*, 6445–6452.

Giorgio, V., Stockum, von, S., Antoniel, M., Fabbro, A., Fogolari, F., Forte, M., Glick, G.D., Petronilli, V., Zoratti, M., Szabò, I., et al. (2013). Dimers of mitochondrial ATP synthase form the permeability transition pore. Proc. Natl. Acad. Sci. U.S.A. *110*, 5887–5892.

Goldberg, J.A., Guzman, J.N., Estep, C.M., Ilijic, E., Kondapalli, J., Sanchez-Padilla, J., and Surmeier, D.J. (2012). Calcium entry induces mitochondrial oxidant stress in vagal neurons at risk in Parkinson's disease. Nat Neurosci *15*, 1414–1421.

Grienberger, C., and Konnerth, A. (2012). Imaging Calcium in Neurons. Neuron *73*, 862–885.

Grutzendler, J., Yang, G., Pan, F., Parkhurst, C.N., and Gan, W.-B. (2011). Transcranial two-photon imaging of the living mouse brain. Cold Spring Harb Protoc *2011*.

Gurney, M.E., Pu, H., Chiu, A.Y., Dal Canto, M.C., Polchow, C.Y., Alexander, D.D., Caliendo, J., Hentati, A., Kwon, Y.W., and Deng, H.X. (1994). Motor neuron degeneration in mice that express a human Cu,Zn superoxide dismutase mutation. Science *264*, 1772–1775.

Gutscher, M., Pauleau, A.-L., Marty, L., Brach, T., Wabnitz, G.H., Samstag, Y., Meyer, A.J., and Dick, T.P. (2008). Real-time imaging of the intracellular glutathione redox potential. Nat Meth *5*, 553–559.

Gutscher, M., Sobotta, M.C., Wabnitz, G.H., Ballikaya, S., Meyer, A.J., Samstag, Y., and Dick, T.P. (2009). Proximity-based protein thiol oxidation by H_2O_2-scavenging peroxidases. Journal of Biological Chemistry *284*, 31532–31540.

Guzman, J.N., Sanchez-Padilla, J., Wokosin, D., Kondapalli, J., Ilijic, E., Schumacker, P.T., and Surmeier, D.J. (2010). Oxidant stress evoked by pacemaking in dopaminergic neurons is attenuated by DJ-1. Nature *468*, 696–700.

Haider, L., Fischer, M.T., Frischer, J.M., Bauer, J., Hoftberger, R., Botond, G., Esterbauer, H., Binder, C.J., Witztum, J.L., and Lassmann, H. (2011). Oxidative damage in multiple sclerosis lesions. Brain *134*, 1914–1924.

Hamanaka, R.B., and Chandel, N.S. (2010). Mitochondrial reactive oxygen species regulate cellular signaling and dictate biological outcomes. Trends in Biochemical Sciences *35*, 505–513.

Hansen, J.M., Go, Y.-M., and Jones, D.P. (2006). Nuclear and mitochondrial compartmentation of oxidative stress and redox signaling. Annu. Rev. Pharmacol. Toxicol. *46*, 215–234.

Hanson, G.T., Aggeler, R., Oglesbee, D., Cannon, M., Capaldi, R.A., Tsien, R.Y., and Remington, S.J. (2004). Investigating mitochondrial redox potential with redox-sensitive green fluorescent protein indicators. J. Biol. Chem. *279*, 13044–13053.

Heim, N., Garaschuk, O., Friedrich, M.W., Mank, M., Milos, R.I., Kovalchuk, Y., Konnerth, A., and Griesbeck, O. (2007). Improved calcium imaging in transgenic mice expressing a troponin C–based biosensor. Nat Meth *4*, 127–129.

Hemmer, B., Nessler, S., Zhou, D., Kieseier, B., and Hartung, H.-P. (2006). Immunopathogenesis and immunotherapy of multiple sclerosis. Nat Clin Pract Neurol *2*, 201–211.

Herrero-Mendez, A., Almeida, A., Fernández, E., Maestre, C., Moncada, S., and Bolaños, J.P. (2009). The bioenergetic and antioxidant status of neurons is controlled by continuous degradation of a key glycolytic enzyme by APC/C–Cdh1. Nat. Cell Biol. *11*, 747–752.

Herrmann, J.M., and Dick, T.P. (2012). Redox Biology on the rise. J. Biol. Chem. *393*, 999–1004.

Hirst, J. (2012). Mitochondrial Complex I. Annu. Rev. Biochem. *82*, 551–575.

Hoppins, S., and Nunnari, J. (2012). Mitochondrial Dynamics and Apoptosis-the ER Connection. Science *337*, 1052–1054.

Hou, T., Zhang, X., Xu, J., Jian, C., Huang, Z., Ye, T., Hu, K., Zheng, M., Gao, F., Wang, X., et al. (2013). Synergistic Triggering of Superoxide Flashes by Mitochondrial Ca^{2+} Uniport and Basal ROS Elevation. Journal of Biological Chemistry *288*, 4602–4612.

Ibrahim, W., Lee, U.S., Yen, H.C., St Clair, D.K., and Chow, C.K. (2000). Antioxidant and oxidative status in tissues of manganese superoxide dismutase transgenic mice. Free Radical Biology and Medicine *28*, 397–402.

Imamura, H., Nhat, K.P.H., Togawa, H., Saito, K., Iino, R., Kato-Yamada, Y., Nagai, T., and Noji, H. (2009). Visualization of ATP levels inside single living cells with fluorescence resonance energy transfer-based genetically encoded indicators. Proc. Natl. Acad. Sci. U.S.A. *106*, 15651–15656.

Iyer, L.K., Islam, M.F., and Quastel, J.H. (1961). Biochemical Aspects of Phagocytosis. Nature *192*, 535–541.

Jakovcevski, M., and Akbarian, S. (2012). Epigenetic mechanisms in neurological disease. Nat Med *18*, 1194–1204.

Jares-Erijman, E.A., and Jovin, T.M. (2003). FRET imaging. Nat Biotechnol *21*, 1387–1395.

Karlsson, M., Kurz, T., Brunk, U.T., Nilsson, S.E., and Frennesson, C.I. (2010). What does the commonly used DCF test for oxidative stress really show? Biochem. J. *428*, 183–190.

Kerschensteiner, M., Reuter, M.S., Lichtman, J.W., and Misgeld, T. (2008). Ex vivo imaging of motor axon dynamics in murine triangularis sterni explants. Nat Protoc *3*, 1645–1653.

Kerschensteiner, M., Schwab, M.E., Lichtman, J.W., and Misgeld, T. (2005). In vivo imaging of axonal degeneration and regeneration in the injured spinal cord. Nat Med *11*, 572–577.

Kiningham, K.K., Oberley, T.D., Lin, S., Mattingly, C.A., and St Clair, D.K. (1999). Overexpression of manganese superoxide dismutase protects against mitochondrial-initiated poly(ADP-ribose) polymerase-mediated cell death. Faseb J. *13*, 1601–1610.

Kröncke, K.-D. (2001). Zinc Finger Proteins as Molecular Targets for Nitric Oxide-Mediated Gene Regulation. Antioxidants & Redox Signaling *3*, 565–575.

Kuhlmann, T., Lingfeld, G., Bitsch, A., Schuchardt, J., and Brück, W. (2002). Acute axonal damage in multiple sclerosis is most extensive in early disease stages and decreases over time. Brain *125*, 2202–2212.

Kurz, F.T., Aon, M.A., O'Rourke, B., and Armoundas, A.A. (2010). Spatio-temporal oscillations of individual mitochondria in cardiac myocytes reveal modulation of synchronized mitochondrial clusters. Proc. Natl. Acad. Sci. U.S.A. *107*, 14315–14320.

Lane, N. (2005). Power, sex, suicide: mitochondria and the meaning of life. Oxford University Press.

Lassmann, H., van Horssen, J., and Mahad, D. (2012). Progressive multiple sclerosis: pathology and pathogenesis. Nature Reviews Neurology *8*, 647–656.

Lin, M.T., and Beal, M.F. (2006). Mitochondrial dysfunction and oxidative stress in neurodegenerative diseases. Nature *443*, 787–795.

Love, N.R., Chen, Y., Ishibashi, S., Kritsiligkou, P., Lea, R., Koh, Y., Gallop, J.L., Dorey, K., and Amaya, E. (2013). Amputation-induced reactive oxygen species are required for successful Xenopus tadpole tail regeneration. Nat. Cell Biol. *15*, 222–228.

MacAskill, A.F., and Kittler, J.T. (2010). Control of mitochondrial transport and localization in neurons. Trends in Cell Biology *20*, 102–112.

Mank, M., Santos, A.F., Direnberger, S., Mrsic-Flogel, T.D., Hofer, S.B., Stein, V., Hendel, T., Reiff, D.F., Levelt, C., Borst, A., et al. (2008). A genetically encoded calcium indicator for chronic in vivo two-photon imaging. Nat Meth *5*, 805–811.

Marinkovic, P., Reuter, M.S., Brill, M.S., Godinho, L., Kerschensteiner, M., and Misgeld, T. (2012). Axonal transport deficits and degeneration can evolve independently in mouse models of amyotrophic lateral sclerosis. Proc. Natl. Acad. Sci. U.S.A. *109*, 4296–4301.

Martínez, J.A. (2006). Mitochondrial oxidative stress and inflammation: an slalom to obesity and insulin resistance. Journal of Physiology and Biochemistry *62*, 303–306.

McDonald, J.W., and Sadowsky, C. (2002). Spinal-cord injury. The Lancet *359*, 417–425.

Meyer, A.J., and Dick, T.P. (2010). Fluorescent protein-based redox probes. Antioxidants & Redox Signaling *13*, 621–650.

Millecamps, S., and Julien, J.-P. (2013). Axonal transport deficits and neurodegenerative diseases. Nat Rev Neurosci *14*, 161–176.

Miriyala, S., Spasojevic, I., Tovmasyan, A., Salvemini, D., Vujaskovic, Z., Clair, D.S., and Batinic-Haberle, I. (2012). Manganese superoxide dismutase, MnSOD and its mimics. BBA - Molecular Basis of Disease *1822*, 794–814.

Misgeld, T., Kerschensteiner, M., Bareyre, F.M., Burgess, R.W., and Lichtman, J.W. (2007a). Imaging axonal transport of mitochondria in vivo. Nat Meth *4*, 559–561.

Misgeld, T., Lichtenthaler, S.F., and Dichgans, M. (2013). Between new genetic discoveries and large randomized trials -neurological research in the era of systems medicine. EMBO Rep *14*, 489–492.

Misgeld, T., Nikić, I., and Kerschensteiner, M. (2007b). In vivo imaging of single axons in the mouse spinal cord. Nat Protoc *2*, 263–268.

Mrsic-Flogel, T.D., Hofer, S.B., Ohki, K., Reid, R.C., Bonhoeffer, T., and Hübener, M. (2007). Homeostatic Regulation of Eye-Specific Responses in Visual Cortex during Ocular Dominance Plasticity. Neuron *54*, 961–972.

Murphy, M.P. (2009). How mitochondria produce reactive oxygen species. Biochem. J. *417*, 1–13.

Murphy, M.P., and Smith, R.A.J. (2007). Targeting antioxidants to mitochondria by conjugation to lipophilic cations. Annu. Rev. Pharmacol. Toxicol. *47*, 629–656.

Murphy, M.P., Holmgren, A., Larsson, N.-G., Halliwell, B., Chang, C.J., Kalyanaraman, B., Rhee, S.G., Thornalley, P.J., Partridge, L., Gems, D., et al. (2011). Unraveling the biological roles of reactive oxygen species. Cell Metabolism *13*, 361–366.

Naik, E., and Dixit, V.M. (2011). Mitochondrial reactive oxygen species drive proinflammatory cytokine production. Journal of Experimental Medicine *208*, 417–420.

Nicholls, D.G., and Budd, S.L. (2000). Mitochondria and neuronal survival. Physiol. Rev. *80*, 315–360.

Nicholls, D.G., and Ward, M.W. (2000). Mitochondrial membrane potential and neuronal glutamate excitotoxicity: mortality and millivolts. Trends in Neurosciences *23*, 166–174.

Niethammer, P., Grabher, C., Look, A.T., and Mitchison, T.J. (2009). A tissue-scale gradient of hydrogen peroxide mediates rapid wound detection in zebrafish. Nature *459*, 996–999.

Nikić, I., Merkler, D., Sorbara, C., Brinkoetter, M., Kreutzfeldt, M., Bareyre, F.M., Brück, W., Bishop, D., Misgeld, T., and Kerschensteiner, M. (2011). A reversible form of axon damage in experimental autoimmune encephalomyelitis and multiple sclerosis. Nat Med *17*, 495–499.

Nunnari, J., and Suomalainen, A. (2012). Mitochondria: In sickness and in health. Cell *148*, 1145–1159.

Nylander, A., and Hafler, D.A. (2012). Multiple sclerosis. J. Clin. Invest. *122*, 1180–1188.

O'Donnell, K.C., Vargas, M.E., and Sagasti, A. (2013). WldS and PGC-1 regulate mitochondrial transport and oxidation state after axonal injury. Journal of Neuroscience *33*, 14778–14790.

Parone, P.A., Da Cruz, S., Han, J.S., McAlonis-Downes, M., Vetto, A.P., Lee, S.K., Tseng, E., and Cleveland, D.W. (2013). Enhancing mitochondrial calcium buffering capacity reduces aggregation of misfolded SOD1 and motor neuron cell death without extending survival in mouse models of inherited amyotrophic lateral sclerosis. Journal of Neuroscience *33*, 4657–4671.

Pasinelli, P., and Brown, R.H. (2006). Molecular biology of amyotrophic lateral sclerosis: insights from genetics. Nat Rev Neurosci *7*, 710–723.

Pearse, D.D., Sanchez, A.R., Pereira, F.C., and Andrade, C.M. (2007). Transplantation of Schwann cells and/or olfactory ensheathing glia into the contused spinal cord: Survival, migration, axon association, and functional recovery. Glia *55*, 976–1000.

Perkins, G.A., and Ellisman, M.H. (2011). Mitochondrial configurations in peripheral nerve suggest differential ATP production. Journal of Structural Biology *173*, 117–127.

Plucinska, G., Paquet, D., Hruscha, A., Godinho, L., Haass, C., Schmid, B., and Misgeld, T. (2012). In vivo imaging of disease-related mitochondrial dynamics in a vertebrate model system. Journal of Neuroscience *32*, 16203–16212.

Poburko, D., Santo-Domingo, J., and Demaurex, N. (2011). Dynamic regulation of the mitochondrial proton gradient during cytosolic calcium elevations. Journal of Biological Chemistry *286*, 11672–11684.

Pologruto, T.A., Yasuda, R., and Svoboda, K. (2004). Monitoring neural activity and Ca^{2+} with genetically encoded Ca^{2+} indicators. Journal of Neuroscience *24*, 9572–9579.

Poorkaj, P., Nutt, J.G., James, D., and Gancher, S. (2004). Parkin mutation analysis in clinic patients with early-onset Parkinson's disease. American Journal of Medical Genetics *129A*, 44–50.

Ransohoff, R.M. (2012). Animal models of multiple sclerosis: the good, the bad and the bottom line. Nat Neurosci *15*, 1074–1077.

Robinson, K.M., Janes, M.S., and Beckman, J.S. (2008). The selective detection of mitochondrial superoxide by live cell imaging. Nat Protoc *3*, 941–947.

Roma, L.P., Duprez, J., Takahashi, H.K., Gilon, P., Wiederkehr, A., and Jonas, J.C. (2012). Dynamic measurements of mitochondrial hydrogen peroxide concentration and glutathione redox state in rat pancreatic β-cells using ratiometric fluorescent proteins: confounding effects of pH with HyPer but not roGFP1. Biochem. J. *441*, 971–978.

Santo-Domingo, J., Giacomello, M., Poburko, D., Scorrano, L., and Demaurex, N. (2013). OPA1 promotes pH flashes that spread between contiguous mitochondria without matrix protein exchange. The EMBO Journal *32*, 1927–1940.

Saxena, S., and Caroni, P. (2011). Selective neuronal vulnerability in neurodegenerative diseases: from stressor thresholds to degeneration. Neuron *71*, 35–48.

Saxena, S., Cabuy, E., and Caroni, P. (2009). A role for motoneuron subtype–selective ER stress in disease manifestations of FALS mice. Nat Neurosci *12*, 627–636.

Scalettar, B.A., Abney, J.R., and Hackenbrock, C.R. (1991). Dynamics, structure, and function are coupled in the mitochondrial matrix. Proc. Natl. Acad. Sci. U.S.A. *88*, 8057–8061.

Scheff, S.W., Saucier, D.A., and Cain, M.E. (2002). A statistical method for analyzing rating scale data: the BBB locomotor score. J. Neurotrauma *19*, 1251–1260.

Scheffler, I.E. (2011). Mitochondria (Wiley-Liss). 2nd edition.

Schinzel, A.C., Takeuchi, O., Huang, Z., Fisher, J.K., Zhou, Z., Rubens, J., Hetz, C., Danial, N.N., Moskowitz, M.A., and Korsmeyer, S.J. (2005). Cyclophilin D is a component of mitochondrial permeability transition and mediates neuronal cell death after focal cerebral ischemia. Proc. Natl. Acad. Sci. U.S.A. *102*, 12005–12010.

Schwarzlander, M., Logan, D.C., Johnston, I.G., Jones, N.S., Meyer, A.J., Fricker, M.D., and Sweetlove, L.J. (2012). Pulsing of Membrane Potential in Individual Mitochondria: A Stress-Induced Mechanism to Regulate Respiratory Bioenergetics in Arabidopsis. The Plant Cell *24*, 1188–1201.

Schwarzländer, M., Fricker, M.D., and Sweetlove, L.J. (2009). Monitoring the in vivo redox state of plant mitochondria: Effect of respiratory inhibitors, abiotic stress and assessment of recovery from oxidative challenge. BBA - Bioenergetics *1787*, 468–475.

Schwarzländer, M., Logan, D.C., Fricker, M.D., and Sweetlove, L.J. (2011). The circularly permuted yellow fluorescent protein cpYFP that has been used as a superoxide probe is highly responsive to pH but not superoxide in mitochondria: implications for the existence of superoxide “flashes.” Biochem. J. *437*, 381–387.

Schwarzländer, M., Murphy, M.P., Duchen, M.R., Logan, D.C., Fricker, M.D., Halestrap, A.P., Müller, F.L., Rizzuto, R., Dick, T.P., Meyer, A.J., et al. (2012). Mitochondrial “flashes”: a radical concept repHined. Trends in Cell Biology *22*, 503–508.

Shu, X., Lev-Ram, V., Deerinck, T.J., Qi, Y., Ramko, E.B., Davidson, M.W., Jin, Y., Ellisman, M.H., and Tsien, R.Y. (2011). A genetically encoded tag for correlated light and electron microscopy of intact cells, tissues, and organisms. Plos Biol *9*, e1001041.

Shutov, L.P., Kim, M.-S., Houlihan, P.R., Medvedeva, Y.V., and Usachev, Y.M. (2013). Mitochondria and plasma membrane Ca^{2+}-ATPase control presynaptic Ca^{2+} clearance in capsaicin-sensitive rat sensory neurons. The Journal of Physiology *591*, 2443–2463.

Song, W., Song, Y., Kincaid, B., Bossy, B., and Bossy-Wetzel, E. (2012). Mutant SOD1G93A triggers mitochondrial fragmentation in spinal cord motor neurons: Neuroprotection by SIRT3 and PGC-1α. Neurobiology of Disease *51*, 72–81.

Steinmeyer, J.D., Gilleland, C.L., Pardo-Martin, C., Angel, M., Rohde, C.B., Scott, M.A., and Yanik, M.F. (2010). Construction of a femtosecond laser microsurgery system. Nat Protoc *5*, 395–407.

Stirling, D.P., and Stys, P.K. (2010). Mechanisms of axonal injury: internodal nanocomplexes and calcium deregulation. Trends in Molecular Medicine *16*, 160–170.

Sun C, Berardi MJ, Bushweller JH. (1998). The NMR solution structure of human glutaredoxin in the fully reduced form. J Mol Biol *4*, 687-701.

Surmeier, D.J., Guzman, J.N., and Sanchez-Padilla, J. (2010). Calcium, cellular aging, and selective neuronal vulnerability in Parkinson's disease. Cell Calcium *47*, 175–182.

Swerdlow, R.H. (2011). Brain aging, Alzheimer's disease, and mitochondria. BBA - Molecular Basis of Disease *1812*, 1630–1639.

Tantama, M., Hung, Y.P., and Yellen, G. (2011). Imaging intracellular pH in live cells with a genetically encoded red fluorescent protein sensor. J. Am. Chem. Soc. *133*, 10034–10037.

Tian, L., Hires, S.A., Mao, T., Huber, D., Chiappe, M.E., Chalasani, S.H., Petreanu, L., Akerboom, J., McKinney, S.A., Schreiter, E.R., et al. (2009). Imaging neural activity in worms, flies and mice with improved GCaMP calcium indicators. Nat Meth *6*, 875–881.

Trapp, B.D., and Nave, K.-A. (2008). Multiple Sclerosis: An Immune or Neurodegenerative Disorder? Annu. Rev. Neurosci. *31*, 247–269.

van Lith, M., Tiwari, S., Pediani, J., Milligan, G., and Bulleid, N.J. (2011). Real-time monitoring of redox changes in the mammalian endoplasmic reticulum. Journal of Cell Science *124*, 2349–2356.

Vaseva, A.V., Marchenko, N.D., Ji, K., Tsirka, S.E., Holzmann, S., and Moll, U.M. (2012). p53 Opens the Mitochondrial Permeability Transition Pore to Trigger Necrosis. Cell *149*, 1536–1548.

Veldwijk, M.R., Topaly, J., Laufs, S., Hengge, U.R., Wenz, F., Zeller, W.J., and Fruehauf, S. (2002). Development and optimization of a real-time quantitative PCR-based method for the titration of AAV-2 vector stocks. Mol. Ther. *6*, 272–278.

Vendelbo, M.H., and Nair, K.S. (2011). Mitochondrial longevity pathways. BBA - Molecular Cell Research *1813*, 634–644.

Wallace, D.C. (2012). Mitochondria and cancer. Nat Rev Cancer *12*, 685–698.

Wang, J.-Q., Chen, Q., Wang, X., Wang, Q.-C., Wang, Y., Cheng, H.-P., Guo, C., Sun, Q., Chen, Q., and Tang, T.-S. (2013). Dysregulation of mitochondrial calcium signaling and superoxide flashes cause mitochondrial genomic DNA damage in Huntington disease. Journal of Biological Chemistry *288*, 3070–3084.

Wang, W., Fang, H., Groom, L., Cheng, A., Zhang, W., Liu, J., Wang, X., Li, K., Han, P., and Zheng, M. (2008). Superoxide flashes in single mitochondria. Cell *134*, 279–290.

Wei-LaPierre, L., Gong, G., Gerstner, B.J., Ducreux, S., Yule, D.I., Pouvreau, S., Wang, X., Sheu, S.-S., Cheng, H., and Dirksen, R.T. (2013). Respective contribution of mitochondrial superoxide and pH to Mt-cpYFP flash activity. J. Biol. Chem. *288*, 10567–10577.

Weismann, D., Hartvigsen, K., Lauer, N., Bennett, K.L., Scholl, H.P.N., Issa, P.C., Cano, M., Brandstätter, H., Tsimikas, S., Skerka, C., et al. (2011). Complement factor H binds malondialdehyde epitopes and protects from oxidative stress. Nature *478*, 76–81.

Wekerle, H., Flügel, A., Fugger, L., Schett, G., and Serreze, D. (2012). Autoimmunity's next top models. Nat Med *18*, 66–70.

Westermann, B. (2010). Mitochondrial fusion and fission in cell life and death. Nat Rev Mol Cell Biol *11*, 872–884.

Wilcox, D.E., Schenk, A.D., Feldman, B.M., and Xu, Y. (2001). Oxidation of zinc-binding cysteine residues in transcription factor proteins. Antioxidants & Redox Signaling *3*, 549–564.

Xie, H., Hou, S., Jiang, J., Sekutowicz, M., Kelly, J., and Bacskai, B.J. (2013). Rapid cell death is preceded by amyloid plaque-mediated oxidative stress. Proc. Natl. Acad. Sci. U.S.A. *110*, 7904–7909.

Yanik, M.F., Cinar, H., Cinar, H.N., Chisholm, A.D., Jin, Y., and Ben-Yakar, A. (2004). Neurosurgery: functional regeneration after laser axotomy. Nature *432*, 822.

Youle, R.J., and Narendra, D.P. (2011). Mechanisms of mitophagy. Nat Rev Mol Cell Biol *12*, 9–14.

Zariwala, H.A., Borghuis, B.G., Hoogland, T.M., Madisen, L., Tian, L., De Zeeuw, C.I., Zeng, H., Looger, L.L., Svoboda, K., and Chen, T.W. (2012). A cre-dependent GCaMP3 reporter mouse for neuronal imaging in vivo. Journal of Neuroscience *32*, 3131–3141.

Zhang, C.-Y., Parton, L.E., Ye, C.P., Krauss, S., Shen, R., Lin, C.-T., Porco, J.A., Jr., and Lowell, B.B. (2006). Genipin inhibits UCP2-mediated proton leak and acutely reverses obesity- and high glucose-induced β cell dysfunction in isolated pancreatic islets. Cell Metabolism *3*, 417–427.

Zhang, F., Aravanis, A.M., Adamantidis, A., de Lecea, L., and Deisseroth, K. (2007). Circuit-breakers: optical technologies for probing neural signals and systems. Nat Rev Neurosci *8*, 577–581.

Zhang, Y., Xu, Z., Wang, H., Dong, Y., Shi, H.N., Culley, D.J., Crosby, G., Marcantonio, E.R., Tanzi, R.E., and Xie, Z. (2012). Anesthetics isoflurane and desflurane differently affect mitochondrial function, learning, and memory. Ann Neurol. *71*, 687–698.

Zhao, Y., Araki, S., Wu, J., Teramoto, T., Chang, Y.F., Nakano, M., Abdelfattah, A.S., Fujiwara, M., Ishihara, T., Nagai, T., et al. (2011). An expanded palette of genetically encoded Ca2+ indicators. Science *333*, 1888–1891.

Zhou, R., Yazdi, A.S., Menu, P., and Tschopp, J. (2010). A role for mitochondria in NLRP3 inflammasome activation. Nature *469*, 221–225.

Zorov, D.B., Filburn, C.R., Klotz, L.O., Zweier, J.L., and Sollott, S.J. (2000). Reactive oxygen species (ROS)-induced ROS release: a new phenomenon accompanying induction of the mitochondrial permeability transition in cardiac myocytes. J. Exp. Med. *192*, 1001–1014.